Etienne Rochat



Band 389

# High power optical fiber amplifiers for coherent inter-satellite communication

UFO Atelier für Gestaltung & Verlag

Université de Neuchâtel

Institut de Microtechnique

# High power optical fiber amplifiers for coherent inter-satellite communication

**Thèse**

Présentée à la faculté des sciences
pour obtenir le grade de docteur ès sciences
par

**Etienne Rochat**

Neuchâtel, février 2000.

**UFO Dissertation Band 389**

Die Deutsche Bibliothek – CIP-Einheitsaufnahme

Ein Titelsatz für diese Publikation ist bei Der Deutschen Bibliothek erhältlich.

Dissertation der Universität Neuchâtel
Datum der mündlichen Prüfung: 25. Januar 2000
Referenten: Prof. Dr. R. Dändliker
Prof. Dr. H.-P. Herzig
Dr. R. H. Czichy
Prof. Dr. W. Lüthy

UFO Atelier für Gestaltung & Verlag GbR
Allensbach
Internet http://www.ufo-verlag.de
Maus Druck & Medien GmbH, Konstanz
Erste Auflage 2000

ISBN 3-930803-89-5

# IMPRIMATUR POUR LA THÈSE

**High power optical fiber amplifiers for coherent inter-satellite communication**

de M. Etienne Rochat

---

UNIVERSITÉ DE NEUCHÂTEL

FACULTÉ DES SCIENCES

La Faculté des sciences de l'Université de Neuchâtel sur le rapport des membres du jury,

MM. R. Dändliker (directeur de thèse), H.P. Herzig, R.H. Czichy (Eggersriet) et W. Lüthy (Berne)

autorise l'impression de la présente thèse.

Neuchâtel, le 29 février 2000

Le doyen:

J.-P. Derendinger

A Christine et Rafaël

# Abstract

THE trend in communication systems goes to fast and global networks providing ubiquitous coverage. Therefore, it has been proposed to build satellite communication systems with free space inter-satellite coherent optical cross-connections. Fiber amplifiers are one possible solution to fulfill the power requirements for the optical inter-satellite link.

In this dissertation, we report on the design and the measurement of a high power double-clad doped fiber amplifier for coherent satellite communication systems. The amplifier delivers up to 1.3 W cw at 1.06 μm with about 10 mW input from a single frequency Nd:YAG master oscillator. The polarization state at the amplifier output is stable with an extinction ratio higher than 100:1. To boost the power of the fiber optical amplifier, the combination with a crystal amplifier has also been investigated.

Phase noise in optical amplifiers is a crucial issue in coherent optical communication systems. Since the first measurements published in 1990, it has been assumed that phase noise introduces spectral broadening of the amplified signal. However, there is a controversy in literature, because the theoretical model proposed in the original paper seems not to be correct and also because more recent measurements did not confirm these early results. Therefore, we decided to perform a series of experiments to clarify the situation. After careful investigation, we propose a different model, where the phase noise is introduced as an additive noise rather than a multiplicative noise. This description is in good agreement with the experimental results; no spectral broadening is expected.

Finally, as an attempt towards an integrated emitter for coherent space communication, we designed and investigated an all-fiber master oscillator power amplifier. It consists of a distributed feedback fiber laser, a piece of fiber coated with a piezoelectric layer as phase modulator, and the double-clad fiber amplifier described above.

# Table of Contents

# 1 Introduction

THE story of modern fiber optics communication started about 30 years ago with the demonstration of low loss single-mode fibers. The fibers were first optimized for a wavelength of 1.3 μm, corresponding to the second telecommunication window, because of the absence of chromatic dispersion. In long distance applications however, these systems were limited by the bandwidth of the electronic repeaters.

The first demonstration of an erbium doped fiber amplifier was published in 1986 by a group of the University of Southampton, UK. This was a kind of revolution in the field. Fiber amplifiers can replace electronic repeaters with a much larger bandwidth, they have high gain, are polarization insensitive and operate at a wavelength of 1.5 μm for which the telecommunication fibers exhibit the lowest losses. It ensued a lot of optimizations, leading to almost perfect fiber amplifiers for the large telecommunication market. The technology is now so reliable that the most recent undersea cables use only optical amplifiers.

During these last years, the demand for efficient transmission systems has continuously increased. The trend goes now to fast and global communication networks providing ubiquitous coverage. It is not possible anymore to respond to this request for mobility using the terrestrial networks. The cost for fiber installation is high and can only be accepted to connect highly populated areas. As a result, it was proposed to build satellite communication systems, using optical free space cross-connection to provide a sufficiently high bandwidth. Every point on earth can now be linked to everywhere else!

In the context of free space optical communication, it was demonstrated that coherent communication is the best solution to reduce terminal weight and size, and thus, to save costs. To achieve data rate in the Gbit/s range with optical coherent communication, one needs stable single-frequency single-polarization sources, operating at frequencies sufficiently stable to be locked to one another. Due to the long

distances between the satellites, high optical power is required. The combination of high power single-frequency lasers and fast phase or frequency modulation leads to heavy systems. Splitting the function of modulation and amplification, as demonstrated in RF technology, is a much better solution. It results in a small master oscillator followed by a modulator and a high power optical amplifier. This concept results in the so-called MOPA structure.

Currently, there is a strong interest for coherent free space communication systems, as some commercial satellite networks are being launched (e.g. Teledesic, Astrolink). The European Space Agency (ESA) proposed a project called SROIL (Short Range Intersatellite Links) for the development of a terminal for demonstration purpose. This project was managed by Contraves Space in Zurich and the Institute of Microtechnology at the University of Neuchâtel was entrusted with a study about high power fiber amplifiers. This work on high power amplifiers was also closely coordinated with the Swiss Priority Program Optics II (SPPO II). This gave the opportunity to investigate in more details some specific aspects of optical amplification in doped fibers.

This dissertation is placed in this particular context and the SROIL project became the skeleton of this work.

In chapter 2, the basic principles of optical amplification in doped fibers are presented. An expression is derived for the case of double-clad doped fibers, a special structure used in high power devices. Then, some specific properties of neodymium doped fibers are reviewed.

In chapter 3, we discuss the basic properties of coherent communication. The advantages of coherent detection are highlighted. The goals of the SROIL project are enumerated and the solution proposed by Contraves is also described.

In chapter 4, we present our most important results, namely the gain and output power of the fiber amplifiers as well as the study of its polarization properties. The power conversion efficiency is investigated. Some general considerations on front and side pumping of optical double-clad amplifiers and the effects of pump linewidth and pump wavelength are reviewed. A concept for power scaling of optical amplifiers is also presented, based on the combination of fiber and crystal amplifiers. Power scaling opens the way towards a few tens of Watts, as may be required in further applications.

Chapter 5 is the most fundamental part of this dissertation. First, we analyze the effect of an optical amplifier on the coherent detection, in term of signal-to-noise ratio.

Then, the spectral noise is measured and found to be negligible in the high saturated regime, in which we are working. Finally, phase noise is carefully investigated.

The problem of phase noise was first addressed in 1991, based on experimental results. However, there is a controversy in literature; the theoretical model proposed in the first publication seems to be incorrect. Furthermore, some of the original results were not reproducible. Therefore, we compared the different theoretical models with our experimental results. Then, to overcome the discrepancy between theoretical prediction and measurements, we proposed a new model in which the effect of phase noise is described as an additive process rather than a multiplicative one. Finally, we demonstrated that this description is in good agreement with the experimental data.

All-fiber master oscillator fiber amplifiers (MOPA) are reviewed in chapter 6. Initially, single-frequency fiber lasers are investigated, in order to replace bulky crystal solutions. Then, an all-fiber phase modulator is tested. Finally, a single-frequency fiber laser, a phase modulator and a power amplifier are combined to build an all-fiber MOPA structure, in collaboration with our partners of the SPPO II.

Most of this work has been published as regular papers or at conferences. Several new papers on the effect of phase noise in fiber amplifiers and on all-fiber MOPA are in preparation. The published papers are listed below:

- E. Rochat *et al.*: "Excited-state absorption and gain measurement at 1.3 μm in $Nd^{3+}$ doped silica fibers with different codopants: effect of ceasium on ESA cross-section," *J. Ligthwave Technol.*, vol. 15, pp 1573-1577, 1997.
- U. Roth, T. Graf, E. Rochat, K. Haroud, J. E. Balmer, and H. P. Weber: "Saturation, Gain, and Noise Properties of a Multipass Diode-Laser-Pumped Nd:YAG CW Amplifier," *J. Quantum Electron.*, vol. 34, pp. 1987-1991, 1998.
- Y.-A. Peter, H.-P. Herzig, E. Rochat, R. Dändliker, C. Marxer, N. F.de Rooij: "Pulsed fiber laser using micro-electro-mechanical mirrors," *Opt. Engineering*, vol. 38, pp. 636–640, 1999.
- E. Rochat *et al.*: "High-gain solid-state and fiber amplifier-chain for high-power coherent communication,"*Photon. Technol. Lett.*, vol. 11, pp. 1120-1122, 1999.
- E. Rochat *et al.*: "High power $Nd^{3+}$-doped fiber amplifier for coherent intersatellite links," *J. Quantum Electron.*, vol. 35, pp. 1419-1423, 1999.
- K. Haroud, E. Rochat, R. Dändliker, "A Broad-Band Superfluorescent Fiber Laser Using Single-Mode Doped Silica Fiber Combinations," *J. of Quantum Electron.*, vol. 36, pp. 151-154, 2000.

# 2 Rare-earth doped fibers

RARE earth doped fibers are key components in today communication systems. In order to design well adapted devices, it is important to understand the equations governing the emission and absorption process as well as the physical parameters describing the dopant. The methods commonly used for the measurement of these parameters are reported in detail in many textbooks [1], [2], [3]; they will not be further described in this dissertation.

There is a large choice of rare-earth dopants, depending on the desired application. In section 1.1, we describe the energy diagram and the transitions of neodymium, ytterbium and erbium doped fibers, the most widely used systems.

A model based on the rate equations in 4-level systems, such as neodymium, is developed in section 1.1. Simplifications for strongly pumped systems are introduced and compared later with the experimental results.

Some transitions suffer from excited state absorption (ESA), which reduces the gain at specific wavelengths, preventing laser oscillation or, in the worst case, amplification. In section 1.1, we report on measurements of the ESA cross-section around 1.3 μm in $Nd^{3+}$-doped fibers. It is shown that the magnitude of the ESA cross-section depends strongly on the co-dopant used to build the fiber core. These results have been published by the author as a regular paper in the J. of Ligthwave Technology [4].

# 2.1 Transitions in rare-earth doped fibers

It is beyond the scope of this dissertation to report all transitions used in rare-earth doped fiber amplifiers. We limited ourselves to the cases of neodymium ($Nd^{3+}$), ytterbium ($Yb^{3+}$) and erbium ($Er^{3+}$), which we have been using or considered in our experiments, and which are typical examples of 4, 2 and 3-level systems, respectively. The information given in this paragraph can be found in most text books on fiber amplifiers, for instance [1] and [3].

## 2.1.1 Neodymium doped fibers

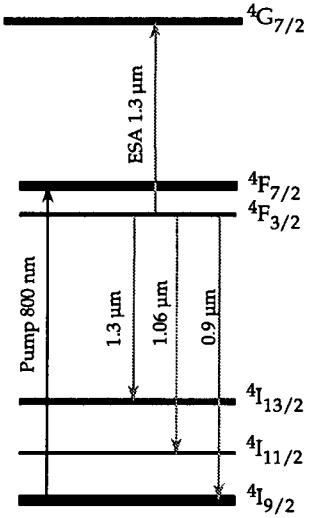


*Fig. 2.1: Energy level of Neodymium doped silica fibers.*

$Nd^{3+}$ ions have three main laser transitions, around 1.3 µm, 1.06 µm and 0.93 µm (Fig. 2.1). The usual pump wavelength is 800 nm, though pumping at 900 nm is also possible. The 1.3 µm transition suffers from excited state absorption (ESA), as described in § 1.1, reducing considerably the gain in the second telecommunication window.

The 1.06 µm transition is of strong interest for single-frequency lasers (using Nd:YAG crystals for example) and frequency up-conversion towards green and blue wavelengths. Moreover, it is a very efficient transition, not suffering from reabsorption, thus being rather insensitive to the fiber length. $Nd^{3+}$ is now being replaced in some applications by $Yb^{3+}$ , which has a larger tunability and a higher efficiency

*Physical parameters*

The fluorescent lifetime of the $^4F_{3/2}$ level in $Nd^{3+}$ doped silica fibers is typically 470 µs, but decreases to 200 µs for high dopant concentration (§ 4.1). The emission cross-section for the 1.06 µm transition is roughly $10^{-24}$ $m^2$, but varies with dopant concentration and co-dopants used within the core (§ 1.1).

### 2.1.2 Ytterbium doped fibers

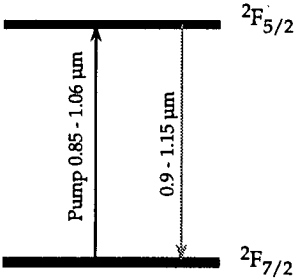


*Fig. 2.2: Energy level of Ytterbium doped silica fibers.*

$Yb^{3+}$ ions in silica have just one broadband laser transition, between 0.97 and 1.2 µm, pumped continuously between 850 and 1064 nm [5] (Fig. 2.2). The absorption peak is at 975 nm. In the short wavelength region, $Yb^{3+}$ has a unique 2-level structure. In the long wavelength region, the transition is rather similar to the 3-level system of $Er^{3+}$.

$Yb^{3+}$ doped fibers are very efficient sources. Due to the simple 2-level system, they do not suffer from excited state absorption.

The emission wavelength can be more or less selected by a careful choice of the pump wavelength. $Yb^{3+}$ doped fibers are now being used at 1020 nm for pumping praseodymium doped fluoride fiber amplifiers (amplification in the 1.3 µm region) and at 1140 nm for pumping thulium doped fibers (upconversion, to get blue light emission). At 1064 nm, they may replace bulky Nd:YAG laser, for instance in coherent communication (§ 6.1.3).

Apart from being used as emitters, $Yb^{3+}$ ions are often combined with $Er^{3+}$, as sensitizers [6]. The $Yb^{3+}$ ions absorb the pump power and, due to cross relaxation between adjacent ions of $Er^{3+}$ and $Yb^{3+}$, the energy is transferred to the $Er^{3+}$ ions. This process allows to have strong absorption of the pump, without signal absorption due to the $Er^{3+}$ concentration, which helps to design short cavity fiber lasers.

*Physical parameters*

The fluorescent lifetime of the $^2F_{7/2}$ level in $Yb^{3+}$ doped silica fibers is typically 840 µs and the peak emission cross-section is $2.5 \times 10^{-24}$ $m^2$, as reported in [5].

### 2.1.3 Erbium doped fibers

$Er^{3+}$ doped silica fibers are the most widely used devices, because they have a transition in the third telecommunication window, around 1.5 µm (Fig. 2.3). They can be pumped either at 800 nm, 980 nm or 1480 nm. The 980 nm pump band is the most advantageous choice. It produces the highest output power and gain with the lowest noise figure. Pumping at 1480 nm is not as good as at 980 nm, but is very useful for remote sensing, where the pump light must propagate within long fibers without loss (see [2], ch.7 for a discussion of the different pump bands).

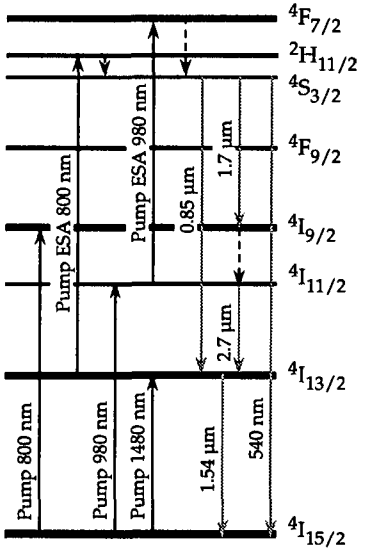


*Fig. 2.3: Energy level of Erbium doped silica fibers.*

The 800 nm pump band suffers from ESA, but it is used for upconversion, producing green emission about 540 nm. Combined with the red emission of praseodymium or samarium doped fibers and with the blue emission of praseodymium or thulium doped fibers, it just opens the way to large-scale projection systems. The same pumping mechanism is also used to obtain laser emission at 850 nm and a cascade of transitions at 1.7 µm and 2.7 µm for medical applications [7].

Erbium doped fiber amplifiers are thus key elements in long range optical transmission systems. They are still under study, in order to broaden the bandwidth, to flatten the gain and to increase the power. As much as 100 channels can be simultaneously amplified, resulting in terabits transmission lines. Output power around tens of watts have also be obtained.

*Physical parameters (1.5 µm)*

The fluorescent lifetime of the $^4F_{13/2}$ level in $Er^{3+}$ doped fibers is typically 10 ms and the peak emission cross-section is $0.5 - 0.8 \times 10^{-24}$ m$^2$.

## 2.2 Theoretical modeling of doped fibers

Many theoretical models are available. They are based on the rate equations and differ mainly by the assumptions and approximations made.

A model based on the mode overlap between pump, signal and dopant distribution has been proposed by Digonet *et al.* [8] and was later extended especially for superfluorescent fiber laser (SFL) [9]. It is assumed that the transition has a single emission linewidth following a Lorentzian lineshape. This is not compatible with the simulation of complex emission spectra. Therefore, at high power, the results became inaccurate.

Assuming a given shape of the dopant concentration in the core, it is possible to find an analytical solution for the rate equations [10]. We also tried this method, but again, in the case of high power amplifiers, the results were not in good agreement with experimental data.

Going back to basics, and modifying the approach described by Desurvire for 3-level systems in [1], we developed a general model taking into account spectral properties of the dopant as well as saturation of the gain and overlap between pump and signal modes. The model assumes homogeneous broadening of the gain medium.

Meanwhile, a commercial software became available for the simulation of erbium doped fiber amplifiers and lasers [11], following the model described in [1]. It is expected, that a version including neodymium and ytterbium doped fibers will be available soon.

### 2.2.1 Rate equations in 4-level systems

The bases of all theoretical models are the rate equations. According to the energy diagram of Fig. 2.4, we define: $R_{14}$ and $R_{41}$, the stimulated absorption and emission rates for the pump transition; $W_{23}$ and $W_{32}$, the stimulated absorption and emission rates for the signal transition; $A_{32}$, $A_{32}^{nr}$, $A_{43}^{nr}$ and $A_{21}^{nr}$, the radiative and nonradiative spontaneous emission rates, respectively.

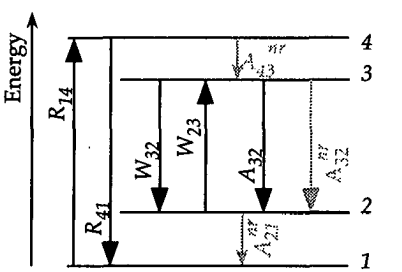


*Fig. 2.4: Energy diagram and definition of the parameters involved in the description of 4-level laser system.*

The stimulated absorption and emission rates are related to the photon densities through [12]

$$R_{14} = \eta_p \frac{c}{n}\sigma_p = \frac{I_p}{h\nu_p}\sigma_p \tag{2.1}$$

$$W_{32} = \eta_s \frac{c}{n}\sigma_s = \frac{I_s}{h\nu_s}\sigma_s, \tag{2.2}$$

where $\eta_{s,p}$ are the photon densities at signal and pump wavelength, respectively, $c$ is the speed of light in vacuum, $n$ is the index of refraction and $\sigma_{s,p}$ are the transition cross-sections at signal and pump wavelength, respectively.
The spontaneous emission rate $A_{32}$ is related to $\tau_{32}$, the lifetime of the upper level of the laser transition, by

$$A_{32} = \frac{1}{\tau_{32}}. \tag{2.3}$$

The population densities of the four levels are $N_1$, $N_2$, $N_3$ and $N_4$. Using these definitions, we get the rate equations:

$$\frac{dN_1}{dt} = R_{41}N_4 + A_{21}^{nr}N_2 - R_{14}N_1 \tag{2.4}$$

$$\frac{dN_2}{dt} = W_{32}N_3 + A_{32}N_3 + A_{32}^{nr}N_3 - W_{23}N_2 - A_{21}^{nr}N_2 \tag{2.5}$$

$$\frac{dN_3}{dt} = W_{23}N_2 - A_{32}N_3 - A_{32}^{nr}N_3 - W_{32}N_3 + A_{43}^{nr}N_4 \tag{2.6}$$

$$\frac{dN_4}{dt} = R_{14}N_1 - R_{41}N_4 - A_{43}^{nr}N_4. \tag{2.7}$$

Assuming that transitions from level 4 to 3 and from level 2 to 1 are predominantly nonradiative, radiative transitions from these levels can be neglected ($R_{41}N_4 = 0$, $W_{23}N_2 = 0$).

The nonradiative transition between level 3 and 2, namely $A_{32}^{nr}N_3$ is neglected in a first approach. In this case, $\tau_{32}$ can be replaced by $\tau_{fluo}$, the fluorescent lifetime of the transition. When necessary, the nonradiative contribution will be reintroduced through the branching ratio (see § 2.3.1). In addition, it is assumed that the nonradiative transitions from level 4 to 3 and from level 2 to 1 are much faster than any other transition. Therefore, the population densities $N_4$ and $N_2$ are negligibly small with respect to $N_3$ and $N_1$, so that

$$N_1 + N_3 = \rho, \tag{2.8}$$

where $\rho$ is the total dopant population density.

Using Eq. (2.8) and solving Eqs. (2.4) - (2.7) for $N_3$ at steady state ($dN_i/dt = 0$) finally leads to

$$N_3 = \rho \frac{R_{14}\tau_{fluo}}{1 + \tau_{fluo}(R_{14} + W_{32})}. \tag{2.9}$$

It is then straightforward to find for the population density in level 1

$$N_1 = \rho \frac{1 + W_{32}\tau_{fluo}}{1 + \tau_{fluo}(R_{14} + W_{32})}. \tag{2.10}$$

*Transition cross-section*

The local absorption, emission and pumping rates are also related to the signal and pump intensities $I_s(z)$ and $I_p(z)$, respectively. Using the emission cross-section $\sigma_s$ at signal wavelength $\lambda_s$ and the absorption cross-section $\sigma_p$ at pump wavelength $\lambda_p$, the differential intensity changes over a slice of thickness $dz$ of the gain medium are given by [13]

$$\frac{dI_s}{dz} = \sigma_s N_3(z) I_s(z) \tag{2.11}$$

$$\frac{dI_p}{dz} = -\sigma_p N_1(z) I_p(z). \tag{2.12}$$

*Saturation*

The lifetime of the upper level of the laser transition plays a key role in the understanding of saturation mechanism. Equation (2.9) can be written in the generic form [12] [13] [14]

$$N_3 = \frac{N_0}{1 + \tau_{sat} W_{32}}, \tag{2.13}$$

where

$$N_0 = \rho \frac{\tau_{fluo} R_{14}}{1 + \tau_{fluo} R_{14}} \tag{2.14}$$

is the steady-state population difference and

$$\tau_{sat} = \frac{\tau_{fluo}}{1 + \tau_{fluo} R_{14}} \tag{2.15}$$

is the saturation time constant. Following Eq. (2.2), $W_{32}$ is a function of the signal intensity $I_s$. Therefore, the population density $N_3$ will depend on the signal intensity, and we get finally

$$N_3 = \frac{N_0}{1 + \tau_{sat}\sigma_s \dfrac{I_s}{h\nu_s}}, \tag{2.16}$$

where $h\nu_s/\sigma_s\tau_{sat}$ is known as the saturation intensity $I_{sat}$.

Though very useful, the saturation time constant $\tau_{sat}$ cannot be measured. The only physical parameter to which we have access is the fluorescent lifetime $\tau_{fluo}$. Thus, it is more convenient to define saturation intensities for pump and signal with respect to $\tau_{fluo}$ as

$$I_s^{sat} = \frac{h\nu_s}{\sigma_s \tau_{fluo}}, \quad I_p^{sat} = \frac{h\nu_p}{\sigma_p \tau_{fluo}}. \tag{2.17}$$

*Mode envelope*

The intensity does not only depend on the position z along the fiber, but, through the guiding properties, also on the position $(r, \theta)$ in the cross-section of the fiber. According to [1], we define a normalized mode envelope $\bar{\psi}_{s,p}(r,\theta)$, with $(r, \theta)$ representing the cylindrical transverse coordinates, so that

$$\bar{\psi}_{s,p}(r,\theta) = \frac{\psi_{s,p}(r,\theta)}{\int_S \psi_{s,p}(r,\theta)\ r dr d\theta}, \tag{2.18}$$

where $\psi_{s,p}(r, \theta)$ is the intensity profile of the mode.
The indices s and $p$ stand for the signal and the pump, respectively, and $S$ is the fiber cross-section. The intensity is then given by

$$I_{s,p}(r,\theta) = P_{s,p}\bar{\psi}_{s,p}(r,\theta), \tag{2.19}$$

where $P_{s,p}$ is the total power guided by the respective modes.
For weakly guiding step-index fibers, the modes are well described by the *LP* mode solutions [15]. In the case of single mode fibers, the intensity profile is described by

$$\psi_{s,p} = \begin{cases} J_0^2\left(U_{s,p} \cdot \frac{r}{a}\right) & \text{for } r \le a \\ \frac{J_0^2(U_{s,p})}{K_0^2(W_{s,p})} K_0^2\left(W_{s,p} \cdot \frac{r}{a}\right) & \text{for } r > a\ , \end{cases} \tag{2.20}$$

where $J_0$ and $K_0$ are the zero order Bessel functions, $a$ is the core radius, $U_{s,p}$, $V_{s,p}$ and $W_{s,p}$ are the normalized frequency and eigenvalue parameters (see [16] and [17] for definition and calculation of these terms).

It is useful to define a mode power radius [1] so that

$$\omega_{s,p} = \left[\frac{1}{\pi}\int_S \psi_{s,p}(r,\theta) r\ dr\ d\theta\right]^{1/2}. \tag{2.21}$$

Combining Eqs. (2.18) and (2.21), the mode envelope becomes

$$\psi_{s,p}(r) = \pi\omega^2\bar{\psi}_{s,p}(r), \tag{2.22}$$

from which we find the mode power radius

$$\omega_s = a\frac{V_s K_1(W_s)}{U_s K_0(W_s)} J_0(U_s). \tag{2.23}$$

*Evolution of pump and signal power along the fiber*

The evolution of the signal power $P_s(z)$ along the z axis of a single mode fiber is obtained by substitution of Eq. (2.19) into Eq. (2.11). After combination with Eq. (2.22) and integration over $\theta$ ($LP_{01}$ mode), one gets

$$\frac{dP_s}{dz} = \frac{2\sigma_s P_s}{\omega_s^2}\int N_3(r,z)\psi_s(r,z)\ r dr. \tag{2.24}$$

The spontaneous emission is introduced as a noise photon of power $P_0 = h\nu\delta\nu$ into the bandwidth $\delta\nu$. The power differential gain of the signal is finally given by

$$\frac{dP_s}{dz} = \frac{2\sigma_s(P_s + 2P_0)}{\omega_s^2}\int N_3(r,z)\psi_s(r,z)\ rdr, \tag{2.25}$$

where we take into account the two orthogonal polarization modes for the spontaneous emission. In a similar way, we get for the evolution of the pump power $P_p(z)$ along the z axis in the $LP_{01}$ mode

$$\frac{dP_p}{dz} = -\frac{2\sigma_p P_p}{\omega_p^2}\int N_1(r,z)\psi_p(r,z)\ rdr. \tag{2.26}$$

It is important to note, that we assumed a pump beam propagating in the same direction as the signal, which is known as forward pumping. For backward pumping, the sign in Eq. (2.26) will change.

A more restrictive assumption is that all ions at any point $(r, \theta, z)$ in the fiber core have the same transition cross-section. This is equivalent to assume homogenous broadening, which is not correct for glass hosts, such as in doped silica fibers. A derivation of the more general case is given in [1], but it is beyond the scope of this dissertation.

*Emission and pumping rate*

Substituting Eqs. (2.19) and (2.22) into Eq. (2.2) gives for the stimulated emission rate

$$W_{32}(r,z) = \frac{\sigma_s}{h\nu_s\pi\omega_s^2}P_s(z)\psi_s(r). \tag{2.27}$$

In a similar way, the pumping rate is given by

$$R_{14}(r,z) = \frac{\sigma_p}{h\nu_p\pi\omega_p^2}P_p(z)\psi_p(r). \tag{2.28}$$

Multiplying Eqs. (2.27) and (2.28) by the lifetime $\tau_{fluo}$, together with Eq. (2.17), allows us to introduce the saturation power $P_s^{sat}$ and $P_p^{sat}$

$$P_s^{sat} = I_s^{sat}\pi\omega_s^2;\ P_p^{sat} = I_p^{sat}\pi\omega_p^2 \tag{2.29}$$

at signal and pump wavelength, respectively, so that the emission and absorption rates are written as

$$W_{32}(r,z)\tau = \frac{P_s(z)}{P_s^{sat}}\psi_s(r) \tag{2.30}$$

$$R_{14}(r,z)\tau = \frac{P_p(z)}{P_p^{sat}}\psi_p(r). \tag{2.31}$$

We also normalize the signal and pump power to their respective saturation power, namely

$$s(z) = \frac{P_s(z)}{P_s^{sat}}, p_0 = \frac{P_0}{P_s^{sat}},\ p(z) = \frac{P_p(z)}{P_p^{sat}}. \tag{2.32}$$

Substituting Eqs. (2.30) and (2.31) in (2.9) and (2.10), one gets for the population density of level 3

$$N_3(r) = \rho \frac{p(z)\psi_p(r)}{1 + \left(p(z)\psi_p(r) + s(z)\psi_s(r)\right)} \tag{2.33}$$

and for the population density of the ground state

$$N_1(r) = \rho \frac{1 + s(z)\psi_s(r)}{1 + \left(p(z)\psi_p(r) + s(z)\psi_s(r)\right)}. \tag{2.34}$$

To take into account the distribution of the dopant concentration $\rho$ across the fiber core, we define a dopant profile $\rho(r)$ and the maximum concentration $\rho_0$. After substitution of Eqs. (2.33) and (2.34) into (2.25) and (2.26), using (2.32), we find for the differential change of the signal power and the pump power in the fiber amplifier

$$\frac{ds}{dz} = 2\rho_0 \frac{\sigma_s}{\omega_s^2}(s + 2p_0)p(z)\int \frac{\rho(r)}{\rho_0}\psi_s \cdot \frac{\psi_p(r)}{1 + p(z)\psi_p(r) + s(z)\psi_s(r)}\, rdr \tag{2.35}$$

$$\frac{dp}{dz} = -2\rho_0 \frac{\sigma_p}{\omega_p^2} p(z)\int \frac{\rho(r)}{\rho_0}\psi_p \cdot \frac{1 + s(z)\psi_s(r)}{1 + p(z)\psi_p(r) + s(z)\psi_s(r)}\, rdr. \tag{2.36}$$

This set of equations is numerically integrated in both directions, over the entire spectrum. This leads to rather cumbersome computing, but it is the only possibility to take into account the saturation of the gain and the spectral properties of the transition. Some simplification can be made for the dopant distribution $\rho(r)$ and the mode envelope $\psi(r)$. They are described in [1].

*Double-clad doped fibers*

When working with large size multimode pump laser diodes, the pump beam cannot be launched into the single-mode core. Thus, double-clad doped fibers must be used. In double-clad doped fibers, the single-mode doped core is surrounded by a large multimode core, which guides the pump light. The pump power is progressively absorbed by the core (see § 4.1 for a complete description of double-clad doped fiber amplifiers).

The pump distribution is not anymore a $LP_{01}$ mode. However, Eqs. (2.18) and (2.19) still apply so that

$$I_p(r,\theta) = P_p \frac{\psi_p(r,\theta)}{\int_S \psi_p(r,\theta)\, rdrd\theta}, \tag{2.37}$$

where $\psi_p$ is now the intensity profile of the multimode pump beam. In a first approximation, we can consider that this profile is constant ($\psi_p = 1$) over the double-clad cross-section. Thus, Eq. (2.37) reduces to

$$I_p(r,\theta) = \frac{P_p}{\pi r_{clad}^2} \qquad for\ r < r_{clad}, \tag{2.38}$$

where $r_{clad}$ is the radius of the multimode core. This assumption is however not strictly true, as demonstrated experimentally by Bedö *et al.* [18] through the measurement of the absorption coefficient. The intensity profile is more complicated. However, for the following, we will use Eq. (2.38) for the intensity distribution. Substituting Eqs. (2.1), (2.2), (2.9) and (2.10) into Eqs. (2.11) and (2.12), using Eq. (2.38), we get the differential intensity change for signal and pump, respectively

$$\frac{dI_s}{dz} = \rho_0\sigma_s(I_s + 2I_0)\frac{I_p(z)}{I_p^{sat}}\int\frac{\rho(r)}{\rho_0}\cdot\frac{\psi_s(r)}{1+\frac{I_p(z)}{I_p^{sat}}+\frac{I_s(z)}{I_s^{sat}}\psi_s(r)}\,rdr \tag{2.39}$$

$$\frac{dI_p}{dz} = -\rho_0\sigma_p I_p(z)\int\frac{\rho(r)}{\rho_0}\cdot\frac{1+\frac{I_s(z)}{I_s^{sat}}\psi_s(r)}{1+\frac{I_p(z)}{I_p^{sat}}+\frac{I_s(z)}{I_s^{sat}}\psi_s(r)}\,rdr. \tag{2.40}$$

As a consequence of the large multimode core for the pump beam, the pump intensity $I_p = P_p/\pi r_{clad}^2$ is relatively small, even for high pump power. Thus, we can assume that, for pump power below 10 W, the pump intensity $I_p$ is smaller than the pump saturation intensity $I_p^{sat}$. In this case, Eqs. (2.39) and (2.40) reduces to

$$\frac{dI_s}{dz} = \rho_0\sigma_s(I_s + 2I_0)\frac{I_p(z)}{I_p^{sat}}\int\frac{\rho(r)}{\rho_0}\cdot\frac{\psi_s(r)}{1+\frac{I_s(z)}{I_s^{sat}}\psi_s(r)}\,rdr \tag{2.41}$$

$$\frac{dI_p}{dz} = -\rho_0\sigma_p I_p(z)\int\frac{\rho(r)}{\rho_0}\,rdr, \tag{2.42}$$

and we get, after substitutions,

$$\frac{dI_s}{dz} = -\frac{dI_p}{dz}(I_s + 2I_0)\frac{\sigma_s\tau}{h\nu_p}\frac{\int\rho(r)\cdot\frac{\psi_s(r)}{1+\frac{I_s(z)}{I_s^{sat}}\psi_s(r)}\,rdr}{\int\rho(r)\,rdr}. \tag{2.43}$$

Moreover, the signal intensity can be higher than the signal saturation intensity so that Eq. (2.43) further simplify to

$$\frac{dI_s}{dz} = -\frac{\nu_s}{\nu_p}\frac{(I_s + 2I_0)}{I_s(z)}\frac{dI_p(z)}{dz} \cong -\frac{\nu_s}{\nu_p}\frac{dI_p(z)}{dz}. \tag{2.44}$$

This is the case of a fully saturated amplifier for which every pump photon is converted into one signal photon.

### 2.2.2 Strongly pumped amplifiers

Hardy and Oron [19] proposed an analytical solution for strongly pumped double-clad fiber amplifiers. In a first step, they assumed that either the pump or the signal, or both, are large compared to the amplified spontaneous emission (ASE). Then, they used their model to take into account ASE and Rayleigh backscattering [20]. Oron kindly proposed to make some calculations for me and then even gave me the code of this program for further studies.

For information, we reproduce the equations of [19] in the case of backward pumped amplifiers (signal and pump are travelling in opposite direction). The signal and the pump along the z axis are given by

$$P_s^-(z) \cong P_s^-(L)\exp\left[R(L-z)/(1+q)\right]\,\hat{\phi}(L-z) \tag{2.45}$$

$$P_p(z) \cong P_p(0)\left[P_s^-(0)/P_s^-(z)\right]^q \exp\left(-Rz\right), \tag{2.46}$$

with the following definitions

$$\left[\hat{\phi}(L-z)\right]^{1+q} = \left|\frac{1-C_3/C_4}{1-(C_3/C_4)\left[\hat{\phi}(L-z)\right]^{1+q}}\right|^{\left(1+C_2C_4/C_3\right)} = \exp\left(\left[C_4(1+q)(L-z)\right]\right) \tag{2.47}$$

$$q = \frac{\Gamma_p\sigma_p}{\Gamma_s\sigma_e(\lambda_s)} \tag{2.48}$$

$$R = \Gamma_p\sigma_p N + \alpha(\lambda_p) - \alpha(\lambda_s)q \tag{2.49}$$

$$C_2 = \frac{\lambda_s\Gamma_s\sigma_e(\lambda_s)}{\lambda_p\Gamma_p\sigma_p}\cdot\frac{P_s^-(L)}{P_p(L)} \tag{2.50}$$

$$C_3 = \left[\alpha(\lambda_s) + R/(1+q)\right]\cdot C_2 \tag{2.51}$$

$$C_4 = \Gamma_s\sigma_e(\lambda_s)N - R/(1+q) - \alpha(\lambda_s), \tag{2.52}$$

where the power filling factor for the pump $\Gamma_p \cong A_{core}/A_{cladding}$ is the ratio of the area of the core and the area of the cladding (including the core), in the case of double-clad fiber, and the power filling factor for the signal $\Gamma_s \leq 1$. A typical value for $\Gamma_s$ is 0.75 [19]. The model is then extended to take into account the ASE in channel of bandwidth $\Delta\lambda$ [20]. A comparison between experimental results and this model are presented in § 4.4.4.

## 2.3 Comparison of ESA cross-section at 1.3 μm for different $Nd^{3+}$-doped fibers

At the early days of fiber amplifiers, gain was not possible around 1.3 μm. Neodymium doped silica fibers, which seemed to be good candidates, have problems with excited state absorption (ESA) around this wavelength and with the competing laser transition at 1.06 μm. For this reason, most of the installed optical amplifiers have been designed for 1.5 μm, in the third telecommunication window, instead of the second telecommunication window at 1.3 μm.

Since then, some solutions based on other host materials have been proposed, like $Pr^{3+}$ZBLAN (fluoride based glass) fibers or GaLaS glasses [21] [22] [23]. However, it is interesting to better understand the ESA mechanisms for the 1.3 μm transition in $Nd^{3+}$ doped silica fibers.

It is known that $Al_2O_3$ doping of silica shifts the position of the 1.06 μm transition in $Nd^{3+}$ fibers and reduces the excited state absorption [24]. Is this sufficient to allow gain at 1.3 μm? Is it possible to introduce other material in the core to increase this effect? For this reason, we have comparatively investigated the ESA spectra for $Nd^{3+}$-silica fibers co-doped with Ge, Al or Cs.

### 2.3.1 Principle

Assuming that both pump and signal power are much smaller than their respective saturation power (the so called small signal gain approximation), it is possible to rewrite Eqs. (2.35) and (2.36) in the form

$$\frac{ds}{dz} = 2\rho_o \frac{\sigma_s}{\omega_s^2}(p_s + 2p_o)p(z)\int \frac{\rho(r)}{\rho_o}\psi_s\psi_p(r)\ rdr \tag{2.53}$$

$$\frac{dp}{dz} = -2\rho_0 \frac{\sigma_p}{\omega_p^2}p(z)\int \frac{\rho(r)}{\rho_0}\psi_p\ rdr. \tag{2.54}$$

Substituting Eq. (2.54) and the definition of Eq. (2.32) into (2.53), we find

$$\frac{dP_s}{dz} = -\frac{\sigma_s\tau}{h\nu_p\pi\omega_s^2}(P_s + 2P_0)\frac{\pi\omega_p^2\int\frac{\rho(r)}{\rho_0}\psi_s\psi_p(r)\ rdr}{\pi\omega_p^2\int\frac{\rho(r)}{\rho_0}\psi_p\ rdr}\frac{dP_p(z)}{dz}. \tag{2.55}$$

Using the definitions in [25], this last equation can be written in the form

$$\frac{dP_s}{dz} = \frac{\sigma_{eff}\tau}{h\nu_p}\frac{1}{A_f}(P_s + P_0)\frac{F}{\eta_p}\frac{dP_{abs}}{dz}, \tag{2.56}$$

where $\sigma_{eff}$ , the effective transition cross-section, has been introduced to take into account the ESA, $F$ is the overlap integral between signal and pump mode, $\eta_p$ is the fraction of pump power within the fiber core, $A_f$ is the area of the signal mode (related to the core size) and $dP_{abs}/dz = -dP_p/dz$ is the absorbed pump power per unit length. Integrating Eq. (2.56) over the fiber length leads to

$$\ln\left(\frac{P_{s(z=l)}}{P_{s(z=0)}+P_0}\right) = \frac{\sigma_{eff}\cdot\tau}{h\nu_p}\frac{F}{\eta_p}\frac{1}{A_f}\cdot P_{abs}, \tag{2.57}$$

where $P_{abs}$ is the total absorbed pump power and the left hand term is the small signal gain, which can be measured, and is usually given in dB. After taking the logarithm, Eq. (2.57) becomes

$$\sigma_{eff} = \frac{1}{10\log e}\frac{h\nu_p}{\tau}\frac{\eta_p}{F}\frac{A_f}{P_{abs}}\cdot G_{[dB]} = C_0\cdot G_{[dB]}, \tag{2.58}$$

where $G_{[dB]}$ is the small signal gain in dB.

For a transition suffering from ESA (Fig. 2.1), the effective transition cross-section $\sigma_{eff}$ is the difference between the stimulated emission cross-section $\sigma$ and the ESA cross-section $\sigma_{ESA}$ [26]

$$\sigma_{eff} = \sigma - \sigma_{ESA}. \tag{2.59}$$

At a wavelength where no ESA transition occurs (i.e. $\sigma_{ESA} = 0$, for instance at 1.06 μm), the effective transition cross-section is directly given by the stimulated emission cross-section, namely $\sigma_{eff} = \sigma$, which is consistent with the previous notation. It is then possible to define the constant $C_0$ in Eq. (2.58) simply through

$$C_0 = \frac{\sigma}{G_{[dB]}}. \tag{2.60}$$

In a first approximation, the stimulated emission cross-section can be evaluated using the Fuchtbauer-Ladenburg equation [27], [28] [1]

$$\sigma_{peak} = \frac{\lambda_{max}^4}{8\pi n^2 \tau \Delta\lambda_{eff}}, \tag{2.61}$$

where $\lambda_{max}$ is the fluorescence peak wavelength, $c$ is the speed of light in vacuum, $n$ is the index of refraction and $\Delta\lambda_{eff}$ is the effective linewidth of the transition. The effective linewidth is calculated from the fluorescence spectrum. The complicated lineshape of the transition is replaced by a rectangular shape of height $\sigma_{peak}$ and the same area as the one under the fluorescence spectrum. The spontaneous radiative emission lifetime is related to the measured fluorescence lifetime through [1], [28]

---

[1] A discussion of the validity of the Fuchtbauer-Ladenburg equation is given in [1]. The values for the emission cross-section are in general overestimated with this method.

$$\tau_{spont}^{rad} = \frac{\tau_{fluo}}{\beta}, \tag{2.62}$$

where $\beta$ are the branching ratios between radiative and nonradiative transitions (see Fig. 2.4). Values for $\beta$ are given in [29].

If we assume that the spontaneous and stimulated emission spectra both have the same lineshape, it is possible to extract the spectrum of the stimulated emission cross-section $\sigma_{stim}(\lambda)$ by normalizing each transition of the fluorescence spectrum to the $\sigma_{peak}$ given by the Fuchtbauer-Ladenburg equation. Following Eq. (2.59), the ESA cross-section spectrum is then obtained by calculating the difference between the spectra of the stimulated emission cross-section and the effective cross-section of the transition.

### 2.3.2 Experimental results

We measured some $Nd^{3+}$ -silica fibers containing different co-dopants in the core. Three of them were manufactured by the Swiss Center for Electronics and Microtechnology (CSEM), the other one by York Technology Ltd. Their characteristics are given in Table 2-1. The concentration of $Nd^{3+}$ is obtained from comparison of their absorption coefficient with reference samples, as described in [30] and [31].

| | CSEM 060592 | CSEM 210192B | CSEM 160491B | York ND95020E |
|---|---|---|---|---|
| **Co-dopant** | Cs | Cs | Al | Ge |
| **Attenuation at 800 nm [dB/m]** | 42 | 20 | 470 | 13 |
| **Concentration in $Nd^{3+}$ [ppm]** | 955 | 455 | 10700 | 295 |

*Table 2-1: Concentration of Nd and co-dopant.*

The measurement of the fluorescence lifetime was performed using either the conventional impulse response technique or the frequency transfer function method [32]. The results are listed in Table 2-2. We see that cesium increases the lifetime of the $^4F_{3/2}$ level, which is the common upper level for all three transitions at 0.9 µm, 1.06 µm and 1.3 µm (see Fig. 2.1). This increase of the lifetime was confirmed by measurements made at the CSEM.

| | 060592 | 210192B | 160491 | ND95020E |
|---|---|---|---|---|
| **Lifetime [µs]** | 507 | 512 | 336 | 472 |

*Table 2-2: Measured fluorescent lifetime for the different fibers.*

The fluorescence spectrum was obtained by axial detection at the end of the doped fiber (Fig. 2.5). By carefully adjusting the pump power, one can be sure that the spontaneous emission is greater than the stimulated emission. This is true if the

fluorescence power is less than 30 μW, a typical value for our $Nd^{3+}$ doped fibers [32]. The fiber lengths for this measurement were around 1 m, except for the highly doped fiber, which was only 0.1 m long only. We found the expected 20 nm red shift of the 1.06μm transition for Ge co-dopant [33]. We also measured a 30 nm blue shift of the 930 nm transition for Cs co-dopant, similar to the one described in [33] for Al.

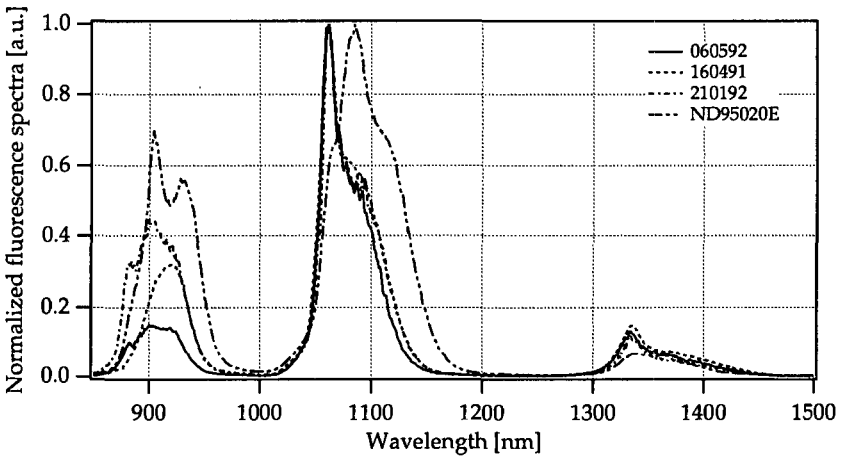


*Fig. 2.5: Fluorescence spectra for the different fibers. (Spectra not corrected for the spectral response of the detector).*

The stimulated emission cross-section spectra are then calculated, using Eq. (2.61). They are shown in Fig. 2.6. It can be seen that the Ge co-doped fiber (ND95020E) is less efficient. The cross-section around 900 nm is almost equal to the cross-section around 1.06 μm, in agreement with the gain measurement (see Fig. 2.8).

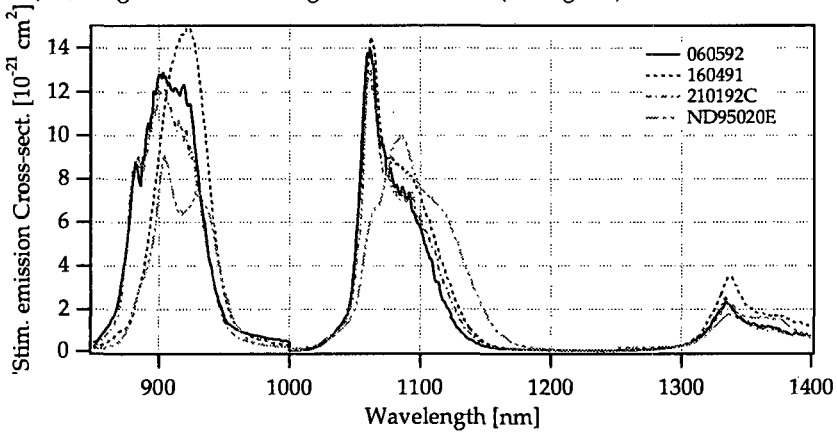


*Fig. 2.6: Stimulated emission cross-sections for $Nd^{3+}$ doped fibers.*

Spectral gain measurements were performed using a semi-conductor laser diode pump (810 nm), co-propagating with the signal from a white light halogen source, as shown in Fig. 2.7. Lock-in detection was used through a Jobin-Yvon HR250 spectrometer, with additional filters to block any residual pump light. With this configuration, the amplified spontaneous emission is filtered.

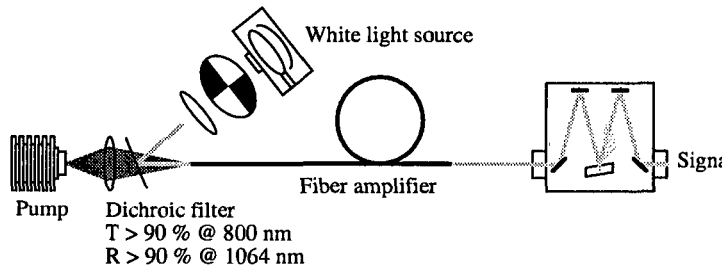


*Fig. 2.7: Set-up for the measurement of the small signal gain in doped fibers.*

The signal power is sufficiently small to neglect gain saturation. The measured gain spectra between 850 nm and 1400 nm in Fig. 2.8 show clearly the three transitions (0.92 µm, 1.06 µm, 1.34 µm) and the excited state absorption (1.31 µm). Only the 060592 Cs co-doped fiber shows measurable gain near 1.3 µm. The gain at 1.35 µm is 0.032 dB per mW of absorbed pump power. However, the gain is also much higher at 1.06 µm than for other fibers, because of the longer fluorescence lifetime, so that most of the emission will take place at this wavelength.

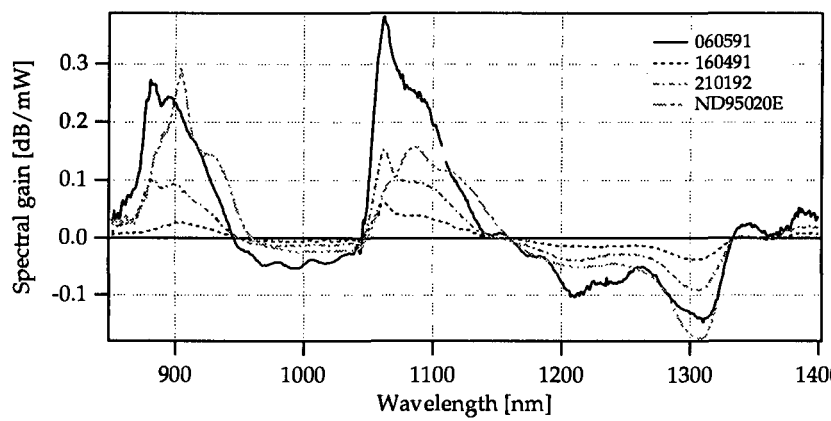


*Fig. 2.8: Spectral gain versus absorbed pump power for Nd3+ doped fibers.*

Following Eq. (2.60), the effective transition cross-section is obtained by multiplication of the gain spectra with the constant $C_0$. Fig. 2.9 shows the resulting ESA

cross-section around 1.3 μm for the four fibers. These results show that the maximum value of the ESA cross-section can be reduced by co-dopants [24], particularly with cesium (Cs). This is the reason for the observed gain at 1.35 μm. However, it is not possible to increase the total gain at 1.3 μm by launching higher pump power into the fiber, because of the competing 1.06 μm laser transition.

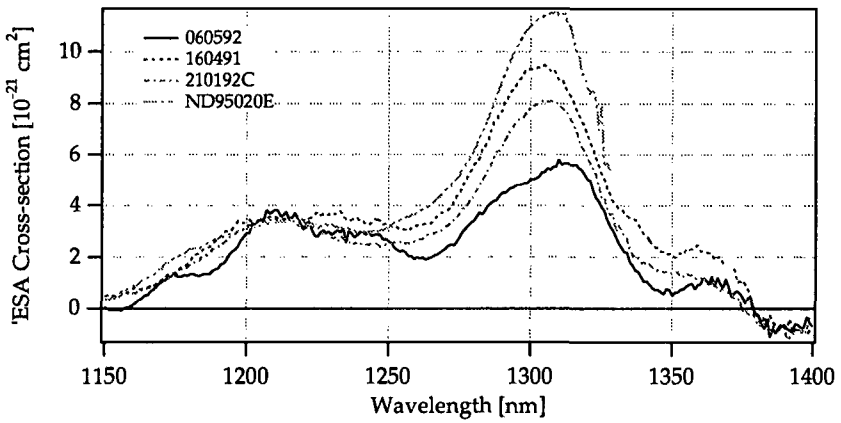


*Fig. 2.9: Comparison of ESA cross-section around 1.3 μm for $Nd^{3+}$ doped fibers.*

It is evident from these results, that $Nd^{3+}$ -silica based fibers are not suitable for amplification at 1.3 μm, even when using Cs co-doping. In fact, the peak of the ESA does not shift according to the co-dopant, as we expected at the beginning of these measurements. The gain is always saturated by the 1.06 μm transition, which shares the same upper level and has a much larger stimulated emission cross-section. To overcome this limitation, we proposed to place a ring of $Yb^{3+}$ around the $Nd^{3+}$ -doped core, to produce distributed losses at 1.06 μm. In such a configuration, the laser effect should not build up and more ions should be available for the gain at 1.3 μm. A fiber has been drawn by the CSEM. We measured its fluorescence spectrum (Fig. 2.10) and found a strong dependence with the fiber length, consistent with distributed loss at 1.06 μm. However, almost no fluorescence was seen at 1.3, and no measurable gain was found at 1.34 μm.

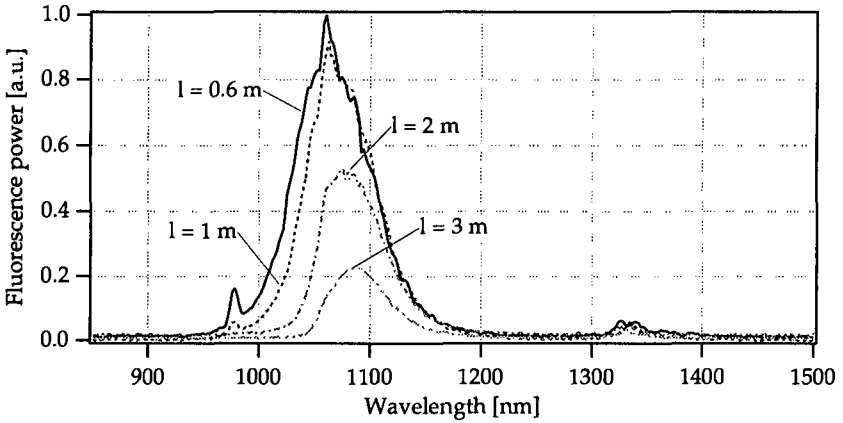


*Fig. 2.10: Fluorescence spectra of fiber 030795. Containing a ring of $Yb^{3+}$ to generate distributed loss at 1.06 μm.*

In fact, the Cs did not play its role, so that the expected gain around 1.3 μm did not show up. The fluorescence of the $Nd^{3+}$ ions was absorbed by $Yb^{3+}$, so that no stimulated emission did build up at 1.06 μm. However, the fluorescence of the $Yb^{3+}$ ions was partially guided, which explains the observed shift of the fluorescence towards longer wavelengths (Fig. 2.10). Since the results were not encouraging, no further investigations were undertaken with this type of fibers.

# 3 The concept of coherent space communication systems

DURING these last years, there has been such an increasing request for mobile communication that new global approaches had to be studied. Satellite networks appeared to be a good solution. Iridium, a system owned by Motorola, is the first of these global satellite communication networks. Working since October 1998, it consists of 66 satellites in low earth orbit (LEO). The communication between the different satellites is based on radio frequencies. Thus, the system has been mainly designed for voice transmission. Celestri, by Motorola, with 63 LEO and 9 geostationnary earth orbit (GEO) satellites and Teledesic with 288 satellites [34] have been designed for higher data rate. Celestri relies on optical transmission between satellites to insure its large data rate. Recently, Celestri and Teledesic have been joined into one common project.

Optical communication has many advantages over RF transmission systems in space, mainly in terms of flexibility, power consumption, weight and costs. However, the first investigations on optical intersatellite links were based on direct detection of the laser beam and were still bulky and heavy. Thus, it became rapidly evident that optical coherent communication was the only way to achieve the requirements of space communication [35] [36], as it is only limited by quantum noise. Moreover, it is less sensitive to background illumination than direct optical detection and allows closer channel spacing. For this reason, and within the context of global communication networks, the European Space Agency (ESA) proposed a project called SROIL (Short-Range Optical Intersatellite Link) to demonstrate, over short distance, the feasibility of optical data transmission between satellites. The contract for the development of this system was awarded to Contraves Space in Zurich. IMT Neuchâtel was a subcontractor in charge of the fiber amplifier development.

Section 3.1 summarizes the basic theory of coherent optical communication while section 3.2 describes the SROIL project.

## 3.1 Summarized theory of coherent communication

Coherent optical communication has mainly two advantages over direct detection scheme [37]. First, higher sensitivity is achieved because the power of the local oscillator can be set arbitrarily high so that the detection is limited by the quantum noise of the received light. Quantum noise is much lower than the multiplication noise in avalanche photodiode or the thermal noise of the load resistance, which dominate in direct detection. It can be shown that direct detection requires hundreds of photons per bit, which is above the quantum limit of 10 photons per bit normally attained with coherent systems, assuming a bit error rate of $10^{-9}$ (see § 3.1.3 for a definition of the BER). The fact that terrestrial networks operate usually with direct detection schemes results from the possibility to implement optical amplifiers in the fiber lines at certain intervals. However, in space where weight and high reliability over long lifetime in orbit are the most important criteria, coherent detection seems still to be the best solution.

The second advantage is the increased selectivity of the receiver. It allows better packing of the channels in the frequency domain, an important aspect for high data rate transmission. Furthermore, the sensitivity to high intensity broadband sources like the sun, the planets or certain stars is largely reduced. It becomes even possible to communicate with the sun in the receiver field of view, when a coherent tracking sensor is used. Moreover, constant envelope modulation schemes, like frequency shift keying (FSK) or phase shift keying (PSK), reduce transient phenomena.

Using the semiclassical description of noise and following the treatment of [1] (mainly ch. 3), [37] and [38], we will analyze the general case of heterodyne coherent detection and its sensitivity to noise. The contribution of the optical amplifier to both phase and amplitude noise will be reviewed in chapter 5.

### 3.1.1 Heterodyne coherent detection

In heterodyne systems, the receiver combines the signal beam with a reference beam coming from the local oscillator, as shown in Fig. 3.1.

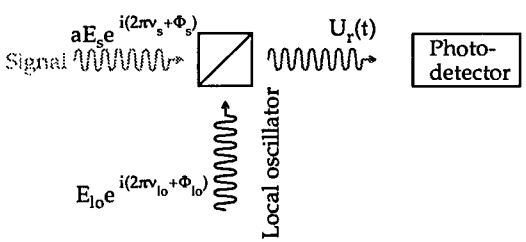


*Fig. 3.1: Principle of heterodyne detection.*

The frequency of the local oscillator and the emitter must be locked, using an optical phase locked loop. We will see later (§ 3.2) the conditions required for such systems.

The electrical signal on the photodiode is given by

$$P_{ph} = E_s^2 + E_{lo}^2 + 2E_sE_{lo}\cdot\cos(2\pi\Delta\nu t + \Delta\phi) = P_s + P_{lo} + 2\sqrt{P_sP_{lo}}\cdot\cos(2\pi\Delta\nu t + \Delta\phi), \tag{3.1}$$

where $P_{ph}$ is the optical power on the photodiode, $P_s = E_s^2$ and $P_{lo} = E_{lo}^2$ are the power of the incoming signal and the local oscillator, respectively, $\Delta\nu$ is the frequency difference between the two beams and $\Delta\phi$ is the phase difference.

### 3.1.2 Signal-to-noise ratio

The mean number of photons arriving on the detector during the integration time $\tau$ is

$$\bar{n}_p = \frac{P_{opt}\tau}{h\nu}, \tag{3.2}$$

where $h$ is the Plank constant and $\nu$ is the frequency of the light. The integration time is related to the electrical bandwidth through

$$B_e = \frac{1}{2\tau}. \tag{3.3}$$

Reference [12] (Appendix A) describes in more detail the different definitions for the electrical bandwidth. The mean number of electrons created in the photodiode is

$$\bar{n}_e = \eta\bar{n}_p + \bar{n}_d, \tag{3.4}$$

where $\eta$ is the efficiency of the photon-electron conversion and $\bar{n}_d$ is the number of electrons generated in darkness (which produce the dark current of the photodetector).

The current is simply the product of the number of electrons by the charge of the electron divided by the integration time. Thus, using Eqs. (3.2) and (3.4) we get

$$\bar{i}_e = \frac{e}{\tau}\left(\eta\frac{P_{opt}\tau}{h\nu} + \bar{n}_d\right) = \frac{e\eta}{h\nu}P_{opt} + \bar{i}_d, \tag{3.5}$$

where $e$ is the charge of the electron, $\bar{i}_d$ is the dark current and $P_{opt} = P_s + P_{lo}$ is the mean power on the photodiode according to Eq. (3.1). The term $e\eta/h\nu$ is referred to as the spectral sensitivity $S$ of the photodiode. The optical power can be set to a level such that the first term of Eq. (3.5) is predominant, so that the dark current can be neglected.

The statistics of the number of detected photons follows a Poisson distribution. The fluctuation (variance) of the current is directly related to the fluctuation $< \Delta n_e^2 >$ of the number of detected photons, which is equal to the mean value $\bar{n}_e$ for the Poisson distribution. Thus, the corresponding noise becomes

$$< \Delta i_{sn}^2 > = < \Delta n_e^2 > \frac{e^2}{\tau^2} = 2eB_e\bar{i}_e = 2eB_e\eta\left(\frac{(P_s + P_{lo})e}{h\nu}\right). \tag{3.6}$$

This contribution to the noise is referred to as shot noise.

The electronics used with the photodetector is responsible for thermal noise or electrical noise, sometimes called Johnson noise. This source of noise is related to the capacitance of the photodiode and the temperature. The equivalent current noise is [38]

$$< \Delta i_{tn}^2 >= \frac{2kTC}{\tau^2} \cong \frac{4kTB_e}{R}, \tag{3.7}$$

where $k$ is the Boltzman constant, $T$ is the temperature, $C$ is the capacitance and $B_e = 1/2\tau \cong 1/2RC$.

The signal-to-noise ratio is defined as

$$SNR = \frac{< i_s^2 >}{< \Delta i_{noise}^2 >} = \frac{< i_s^2 >}{< \Delta i_{sn}^2 > + < \Delta i_{tn}^2 >}, \tag{3.8}$$

where $i_s$ is the photodetector current, corresponding to the information.

The relevant information in coherent optical communication is the beat signal

$$P_{sig} = 2\sqrt{P_s P_{lo}} \cdot \cos(2\pi\Delta\nu t + \Delta\phi) \tag{3.9}$$

in the optical power $P_{ph}$ on the photodetector (Eq. (3.1)). The corresponding power of the electrical signal is given by the averaged value of the square of the photodetector current

$$\begin{aligned} < i_s^2 > &=< 4P_s P_{lo} \cdot \cos^2(2\pi\Delta\nu t + \Delta\phi) > \left(\frac{e\eta}{h\nu}\right)^2 \\ &= 2 \cdot \left(\frac{e\eta}{h\nu}\right)^2 \cdot P_s P_{lo} \ . \end{aligned} \tag{3.10}$$

Combining Eqs. (3.6), (3.7), (3.8) and (3.10) we get for the signal-to-noise ratio

$$SNR = \frac{2P_s P_{lo}}{\frac{2B_e h\nu}{\eta}(P_{s+} P_{lo}) + \frac{4kTB_e}{R}\left(\frac{h\nu}{e\eta}\right)^2}. \tag{3.11}$$

When the power of the local oscillator is set sufficiently high ($P_{lo} >> P_{s\cdot}$), the second term in the denominator (electronic noise) can be neglected and the SNR reduces to

$$SNR = \frac{\eta P_s}{B_e h\nu}. \tag{3.12}$$

Therefore, for a coherent system, the detection is limited by the shot noise of the optical power $P_s$ of the incoming signal only!

### 3.1.3 Bit error rate

In communication, the ultimate parameter is the number of photons to be detected to achieve a given bit error probability (BER). The required BER for space telecommunication systems is usually $\leq 10^{-9}$. For shot noise limited detection and in the case of amplitude modulation, it is straightforward to find the probability for an error, i.e. to detect zero photon for an average number of $\bar{n}$ photons, from the Poisson distribution of the signal, namely

$$p(n=0) = e^{-\eta\bar{n}}. \tag{3.13}$$

In the ideal case $\eta = 1$, we get for $p(n{=}0) = 10^{-9}$ a minimum number of photons $\bar{n} \approx 21$, assuming no coding.

Coherent optical communication is the only solution to reach this fundamental limit. The mean number of photons required for the communication depends on the detection scheme and on the coding of the information, as summarized in Table 3-1 for the case of phase, amplitude and frequency shift keying, PSK, ASK and FSK, respectively [37], [39].

| | PSK | ASK | FSK |
|---|---|---|---|
| Homodyne | 9 | 18 | 36 |
| Synchronous heterodyne | 18 | 36 | 36 |

*Table 3-1: Minimum number of photons/bit for different coherent optical communications systems, assuming $\eta = 1$, a BER of $10^{-9}$ and without coding.*

It is even possible to reduce the number of photons to 5, when the powers of the local oscillator and of the signal are equal in Eq. (3.11); it is the so-called "super quantum limit". Such high sensitivity detection can also be performed using a special synchronization technique, as reported in [40]. This detection scheme is the basis of the SROIL (Short Range Optical Inter-satellite Link) transmission system.

A discussion of BER for coherent and incoherent transmission systems is reported in [36], showing clearly the important difference between these systems, as can be seen in Fig. 3.2.

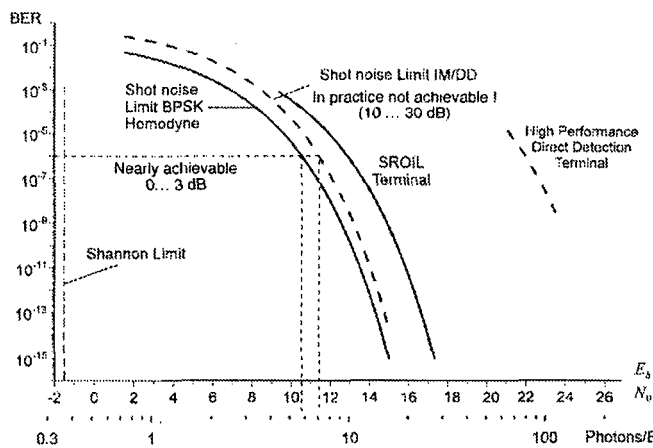


*Fig. 3.2: Theoretical sensitivity limits of coherent and incoherent communication systems, compared with the practically achievable performance (after [36]).*

## 3.2 Coherent optical communication in space: SROIL

There have been already several attempts to build optical intersatellite links. The European Space Agency (ESA) proposed many programs [35] [36], starting with homodyne systems based upon $CO_2$ lasers, later upon Nd:YAG oscillator and then with SILEX (Semi-Conductor Inter Satellite Links Experimental [41]). SILEX «has been dimensioned using the limited laser diode power available at the end of the 1980's, namely 60 mW average power at 830 nm [35].» The result was a 25 cm aperture telescope, a mass of 157 kg and an electrical power consumption of 150 W, providing a data rate of about 150 Mbit/s for inter-orbit links (LEO-GEO). Thus, SILEX was hardly an attractive alternative to a RF terminal.

In order to demonstrate the miniaturization potential for optical terminal when using advanced technologies, the ESA has started a new project named SROIL (Short-Range Optical Intersatellite Links). One of the early results of the development work performed in the frame of this project was to confirm that coherent detection schemes offer the highest miniaturization possibility for high data rate (over 500 Mbit/s) free space communication, and also the best growth potential towards even higher data rates [36].

### 3.2.1 The goals of SROIL

The SROIL project has been proposed for the following missions [35]

- cross-links between low-Earth-orbiting satellites in global satellite networks such as Iridium or Teledesic
- cross-links between co-located telecommunication satellites in geostationary orbit (high data rate)
- cross-links between widely spaced geostationary satellites (medium data rate)

A demonstration unit, including optics, electronics and all other relevant parts had to be build in order to demonstrate the feasibility of the system.

According to the mission scenario described in [42], the system has been designed for links in the range of 1200 km to 4000 km, using a Binary Phase Shift Keying (BPSK) homodyne system for a data rate of about 1.5 Gbps and a Bit Error Rate (BER) of $10^{-9}$. The mass of the terminal head is below 10 kg and its electrical power consumption is lower than 40 W. The telescope has a diameter of only 3.5 cm.

### 3.2.2 Proposed solution

To achieve coherent detection, the frequencies of the local and the master oscillators must be locked. This is only possible for lasers with good spectral quality. At the beginning of the project, there was no such laser available in the 1.55 µm telecommunication window but only at 1.3 and 1.06 µm (Table 3-2). Amplifiers compatible with space applications are not yet available at 1.3 µm, so that the system was finally based on a commercially available diode pumped single-frequency Nd:YAG lasers at 1.06 µm. Single-frequency fiber lasers were not taken into account at that time because there was no commercial solution available. More recently, Ionas A/S (Denmark) started to sell very good distributed feedback fiber lasers, which may be used for this application (see § 6.1.3).

| Wavelength [µm] | Narrow linewidth laser | Amplifier |
|---|---|---|
| 0.8 | Not available | Semi-conductor |
| 1.064 | High power Nd:YAG | Fiber ($Nd^{3+}$, $Yb^{3+}$)<br>solid state ($Nd^{3+}$, $Yb^{3+}$),<br>semi-conductor |
| 1.33 | Low power Nd:YAG | Non-linear effects, ZBLAN fiber |
| 1.55 | Not available | Fiber ($Er^{3+}$), semi-conductor |

*Table 3-2: Review of the elements required to build a coherent communication system, as available at the beginning of the project.*

The optical power required for the SROIL terminal is in the range of 1 W. Nd:YAG lasers with such power are available. However, they must be combined with phase modulators and optical isolators, which are, for this power level, rather bulky and heavy. The modulator would also operate close to its damage limit. This is not compatible with the idea to keep the communication system at low weight and high reliability. Moreover, power scaling of single-frequency lasers seems difficult. For theses reasons, we have chosen a Master Oscillator Power Amplifier (MOPA) structure (Fig. 3.3), using a low power single-frequency Nd:YAG laser with output power around 100 mW, a modulator and then a high power optical amplifier to achieve the required output power.

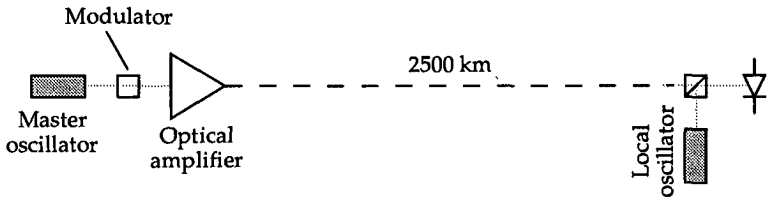


*Fig. 3.3: Concept of coherent communication system using Master Oscillator Power Amplifier.*

In our experiment, the Master Oscillator is a single-frequency Nd:YAG laser from Ligthwave Electronics. It has a linewidth < 5 kHz over 5 ms and an output power of 100 mW. Taking into account the insertion loss in the isolator, the coupling loss to the fiber and the losses in the modulator, we assume that 10 mW are available at the fiber amplifier input. Thus, a gain of at least 20 dB is necessary to obtain the required output power of 1 W. The Power Amplifier is based on double-clad doped fibers pumped by laser diode arrays [43] [44] [45].

IMT has been chosen by Contraves Space as subcontractor to build a fiber amplifier at 1.06 μm for this specific application. This project was the motivation for our work on high-power fiber amplifier systems. It served also as a basis for collaboration with the University of Bern and for the publications made within the context of this dissertation.

# 4 Power fiber amplifier

THE only way to reach high power in doped fibers is. to use a double-clad structure. Such fiber amplifiers are very efficient, because they can be pumped with high power laser diodes. Due to the large outer core area, the system is not very sensitive to pump misalignment, which is of great advantage for space applications. However, a large outer core will reduce the absorption of the pump power, resulting in an increase of the required amplifier length. The gain in the high pump and high signal regime is not sensitive to the fiber geometry, but rather to the dopant concentration. Therefore, a careful adjustment of dopant concentration and outer core diameter is important in order to fulfill the requirements.

To get maximum coherent detection signals, the polarization of the signal and of the local oscillator must be the same. Thus, it is necessary to control the polarization at the output of the amplifier.

In order to increase the output power of single-frequency sources, we combined a fiber amplifier and a crystal amplifier in a dual-stage configuration. This opens the way towards extremely high output power, though loosing the guiding properties of the fiber system.

This chapter presents the results of investigations on $Nd^{3+}$ -doped fiber amplifiers with different dopant concentrations. Section 4.1 describes the concept of double-clad doped fibers and gives the parameters of the fibers we studied. Section 4.2 is an overview of the different pumping conditions. Sections 4.3 and 4.4 report the most interesting results we obtained in terms of polarization stability and output power. The study of the dual stage amplifier, developed in collaboration with the University of Bern, is described in section 4.5.

The results presented in this chapter have been published by the author as regular paper in the J. of Quantum electron. [46] and in. Photonics Technology Letters [47].

## 4.1 Description of the fiber amplifier

Efficient coupling of pump light into single-mode core is difficult for powerful multi-mode laser diodes with large junctions (typically a few 100 of μm); passive beam shaping cannot convert the multi-mode emission into the single-mode accepted by the fiber amplifier core.

In double-clad doped fibers however [43] [44] [45], the single mode core is surrounded by a large multi-mode area into which the pump power can be launched without problem, as shown in Fig. 4.1. Pump light is then progressively absorbed by the doped core, opening the way to high signal output power. Guiding in the outer-clad is obtained by the use of a coating that has an index of refraction lower than silica glass. The simplest geometry is, of course, a centered core in a circular multi-mode guide. Such fibers are commercially available; they have been used for all our investigation. The effect of other designs are reported in [48] and a multicore geometry is proposed in [49].

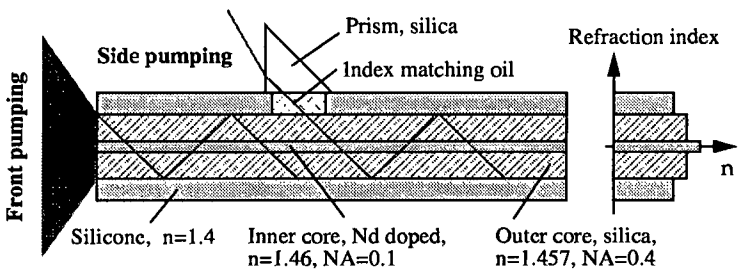


*Fig. 4.1: Front and side pumping of double-clad doped fiber. The coating has an index of refraction lower than the cladding. Therefore, the cladding is a multi-mode core around the single-mode centered core.*

The double-clad technique increases the absorption length [18] so that either high dopant concentration or long fibers are required to absorb efficiently the pump. In long fibers, the absorption at the signal wavelength will reduce the efficiency of the amplifier, since the gain must first compensate for the propagation losses. Long fibers are also more sensitive to cosmic radiation. Radiation increases the absorption in fibers and the induced losses are proportional to the fiber length. On the other hand, propagation losses depend mainly on the fabrication process and cosmic radiation induced losses do not seem to be influenced by the dopant concentration [50] [51] [52]. For these reasons, we have chosen to increase the dopant concentration to keep the fiber short.

The pump power can be launched directly from the front end of the fiber, or from the side, using different techniques [53] [54] [55]. We tried front and side pumping, always in single-pass configuration. A double-pass system would not give more output power for a completely saturated device and the amplifier would be more likely to oscillate.

Pump absorption in double-clad fiber strongly depends on the shape of the fiber coil. For fibers coiled on a cylinder, the absorption increases for decreasing radius of the coil. However, this may not be sufficient to get complete absorption of the pump power. For this reason, Zellmer *et al.* [48] proposed to coil the fiber in a kidney shape. We used this approach in most of our experiments.

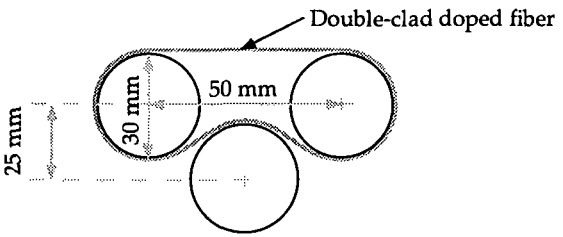


*Fig. 4.2: Typical kidney shape used within this dissertation to coil the double-clad doped fiber.*

Table 4-1 gives the parameters of the fibers we used. The first one was made by the CSEM (Centre Suisse d'Electronique et de Microtechnique, Neuchâtel Switzerland), the others by the IPHT (Institut für Physikalische Hochtechnologie, Jena, Germany). All these fibers were manufactured in silica glass; they have a single-mode core centered in a circular multi-mode core. Their concentrations are deduced from the absorption at the pump wavelength, using calibrated samples of doped fibers [30] [31].

| | CSEM 100192B [53] | IPHT 45 SK 3 | IPHT 152 SK 4 |
|---|---|---|---|
| $\varnothing_{core}$ [µm] | 7 | 4 | 3.4 |
| $NA_{core}$ | 0.1 | 0.19 | 0.22 |
| $\varnothing_{cladding}$ [µm] | 160 | 200 | 180 |
| $NA_{cladding}$ | 0.4 | 0.4 | 0.4 |
| Signal loss (1060 nm) [dB/m] | 1.2 | 0.58 | 0.66 |
| Pump attenuation (800 nm) [dB/m] | 440 | 750 | 1200 |
| $Nd^{3+}$ [weight] | 1 % | 1.7 % | 2.7 % |
| Lifetime [ms] | 330 | 270 | 230 |

*Table 4-1: Parameters of the double-clad doped fibers. Concentration are computed using [31].*

Some fibers were specially drawn for us by the team of Dr. Tosin (IAP, Berne). Unfortunately, they did not reach the required dopant concentration or had excessive loss at the signal wavelength. For this reason, they are not considered in this work.

The amplifier is working in counter-propagation, which is the best solution to maximize the output power [56]. Thus, our amplifier is similar to most of the systems going towards higher output power [57]. There is however a degradation of the noise figure (see § .5.1 for a definition of noise figure) for counter-propagating amplifiers, but this is not critical for phase modulated signal as in the case of coherent communication systems.

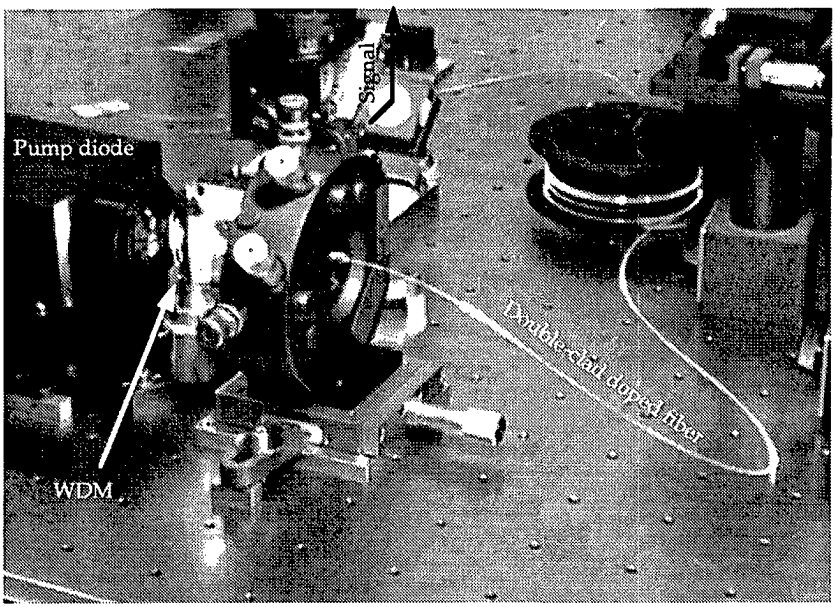


*Fig. 4.3: IR view of a double-clad fiber amplifier pumped by the Fisba laser diodes module.*

# 4.2 Pumping of double-clad doped fibers

## 4.2.1 Front pumping

Front pumping is the most direct method to launch pump power into double-clad doped fibers. It is suitable for fiber lasers, because only one end of the fiber is used as output. Thus, the other end is free for pumping. In amplifiers, however, the problem is a bit more difficult. Both sides of the fiber are required to couple the signal in and out. Thus, one end must be shared between pump and signal beam, requiring WDM (wavelength division multiplexing) technique (see Fig. 4.13 and § 4.4.).

## 4.2.2 Side pumping

In some early experiments, based on the CSEM 100192B fiber (see Table 2-1 and Table 4-1 for a description of this fiber), we investigated side pumping through a prism, as described in [53]. Side pumping is a very attractive scheme, because it allows to maintain both ends of the fiber free, which makes signal coupling easier. In addition, repetitive pumping is possible, and thus higher pump power is available. With a Ti:sapphire laser as pump source we obtained a coupling efficiency of the pump power into the 160 µm multi-mode core of nearly 60 %. We tried then to launch pump power from a high power laser diode module (Fisba Optik: NA = 0.56, spot size = 186 µm x 332 µm, P = 23 W cw at 805 nm). With this module, we were not able to reach sufficient coupling efficiency. The method is too sensitive to beam quality.

## 4.2.3 Effect of the coil shape on the output power

We investigated the effect of the coil shape on the output power, according to [48]. Using a 25 m long 45 SK3 fiber, we measured the output power in the signal direction for different coil shape, when the amplifier is working as a superfluorescent fiber laser (SFL). This gives a good estimation of the possibilities of the amplifier. As expected, we observed a strong variation of the output power, as summarized in Table 4-2.

| Coil shape | Fluorescence output power [mW] |
|---|---|
| 25 m coiled on ø 150 mm | 200 |
| 5 m coiled on ø 90 mm, remaining part coiled on ø 150 mm | 420 |
| 5 m in kidney shape, remaining part coiled on ø 150 mm | 600 |
| 10 m in kidney shape, remaining part coiled on ø 150 mm | 860 |
| 12 m in kidney shape, remaining part coiled on ø 150 mm | 900 |

*Table 4-2: Effect of the coil shape on the fluorescence output power.*

Using the last configuration described in Table 4-2, we obtained 1.3 W in the amplified signal, as will be shown later in this chapter.

### 4.2.4 Effect of the pump linewidth

The transition used to pump $Nd^{3+}$ doped fibers is large. However, changes in the center wavelength or in the linewidth may affect the pumping efficiency. We investigated theoretically, using a simple model, the effect of the pump linewidth and the pump center wavelength on the absorption by the doped fiber.

The absorption and emission linewidth are assumed to be of Loretzian shape ([12] p. 444). Thus, the absorption coefficient $\alpha(\lambda)$ of the fiber and the emission power spectrum of the pump laser diode are given by their full width at half maximum (FWHM) and their magnitude. One can find the amount of absorbed pump power simply by integrating the pump power spectrum $P_{diode}(\lambda)$ over the absorption range as

$$P_{abs} = \int_{\lambda_{min}}^{\lambda_{max}} \eta_c P_{diode}(\lambda) \cdot \left[1 - e^{-\alpha(\lambda) \cdot l_{fibre}}\right] \tag{4.1}$$

where $\lambda_{min}$ and $\lambda_{max}$ are the limiting wavelengths of the pump transition and $\eta_c$ is the pump coupling coefficient into the double-clad fiber.
This equation has been solved numerically for the 100192B fiber (Table 4-1) using the following parameters:

- peak absorption wavelength $\lambda_{peak}$ = 802 nm
- absorption width FWHM $\Delta\lambda$ = 28 nm
- peak absorption coefficient $\alpha_{max}$ = 440 dB/m
- pump power $P_{diode}$ = 1 W
- core diameter: 7 μm
- cladding diameter: 160 μm

For simplicity, $\eta_c$ was set to 1 and the absorption coefficient was simply reduced by the ratio of the area of the core and the clad (see § 2.2.1, Eq. (2.38) for a justification of this assumption). We computed the absorbed pump power when the center wavelength was moving around the absorption peak (Fig. 4.4). The effect of the spectral width of the diode was also investigated (Fig. 4.5).

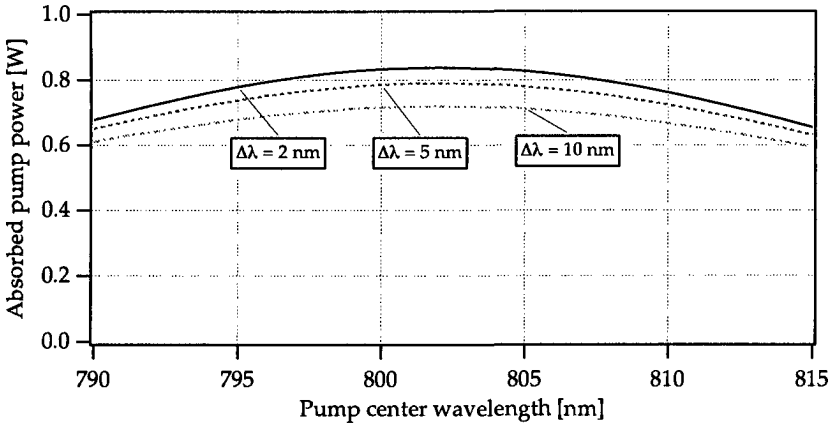


*Fig. 4.4: Absorbed pump power vs. shift of the center wavelength ($P_{diode}$ = 1 W, 10 m long fiber)*

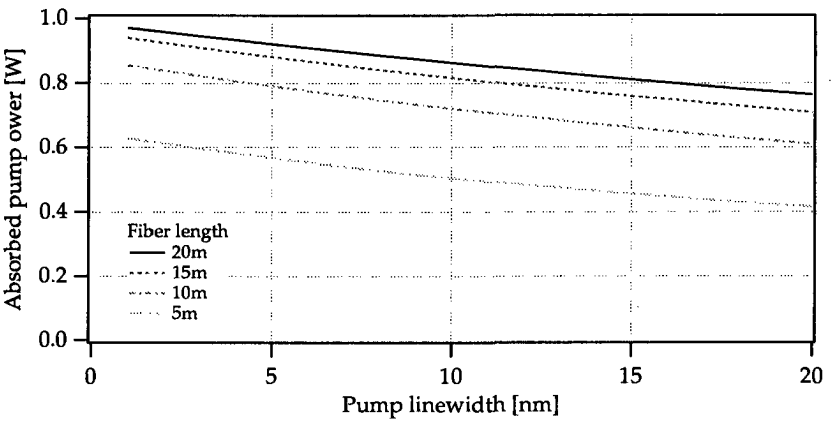


*Fig. 4.5: Reduction of the absorbed pump power due to the increase of the pump linewidth. The pump center wavelength is 802 nm.*

This approach is unfortunately too simple. The absorption of the dopant is not strictly a Loretzian and its magnitude is difficult to measure without specific techniques [16]. The reduction of the absorption coefficient is also not exactly proportional to the ratio of the area of the core and the clad [18]. Therefore, these curves give only the tendency of the variation but not their exact magnitude. However, we see that the variations are slow, so that the quality of the pump is not so critical.

# 4.3 Polarization properties

## 4.3.1 Measurement of the polarization state

The polarization of the signal at the amplifier output was measured using a polarimeter based on the division of wavefront, as described by Ulrich in [58] and Azzam in [59] (Fig. 4.6). The system cannot separate left and right hand polarization states but is sufficient to get the variations of the polarization states around a given position.

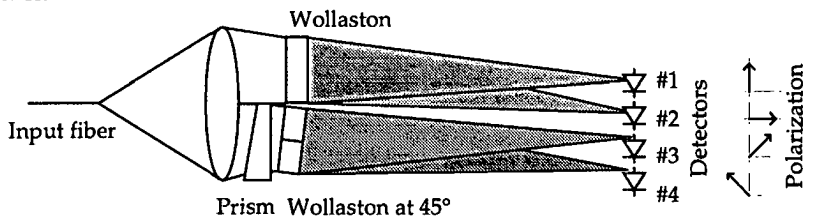


*Fig. 4.6: Four detector polarimeter.*

The intensities $I_1$, $I_2$, $I_3$ and $I_4$ on the detectors are the projections of an elliptical polarization state on four axes (90°, 0°, 45° and -45°), as shown in Fig. 4.7.

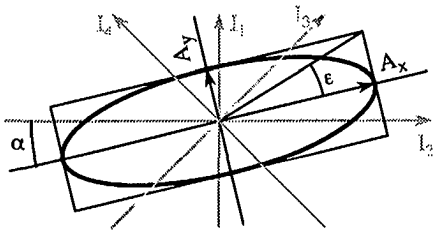


*Fig. 4.7: Elliptical polarization state with orientation α and ellipticity tan(ε).*

The Stokes parameters are defined through the intensities on the 4 detectors by [58]

$$S_0 = I_1 + I_2 + I_3 + I_4 \tag{4.2}$$

$$\frac{S_1}{S_0} = \frac{(I_1 - I_2)}{(I_1 + I_2)} \tag{4.3}$$

$$\frac{S_2}{S_0} = \frac{(I_3 - I_4)}{(I_3 + I_4)} \tag{4.4}$$

$$\left(\frac{S_3}{S_0}\right)^2 = 1 - \left(\frac{S_1}{S_0}\right)^2 - \left(\frac{S2}{S_0}\right)^2. \tag{4.5}$$

It follows that

$$\alpha = \frac{1}{2}\left[\arctan\left(\frac{S_2}{S_1}\right)\right] \tag{4.6}$$

$$\sin 2\varepsilon = \left[1 - \left(\frac{S_1}{S_0}\right)^2 - \left(\frac{S_2}{S_0}\right)^2\right]^{1/2}. \tag{4.7}$$

From the definition of the ellipticity, we can define the extinction ratio as

$$\frac{I_{max}}{I_{min}} = \left[\frac{1}{\tan\varepsilon}\right]^{1/2}, \tag{4.8}$$

where $I_{max}$ and $I_{min}$ are the intensities of the major and minor axis of the polarization state, respectively.

The maximum acquisition rate of the system was 6 kHz. This frequency is low compared with the modulation of the communication signal, but is sufficient to get information on thermal and mechanical perturbations of the amplifier.

### 4.3.2 Stability of the polarization

Perturbations along the fiber can couple light between different polarization modes. Such perturbations are due to variations in the geometry, the composition or the strain in the fibers. They originate in the preform, during the drawing process or, simply, by bends and twists of the fiber. Since the perturbations along the fiber are not known *a priori*, the polarization state at the fiber output cannot be calculated directly. In this case, a random distribution of the perturbations along the fiber is assumed usually [60]. Double-clad doped fibers suffer from this randomly distributed intrinsic birefringence. Thus, a polarization controller is required to obtain a linear polarization state at the output of the fiber amplifier. A Polarite™ all-fiber Babinet-Soleil compensator, manufactured by General Photonics Co., was inserted in the amplifier to achieve the desired polarization state. The stability of the polarization was then measured according to the method described above.

We measured the extinction ratio at the output of an 8 m long passive amplifier (unpumped) coiled on a 10 cm diameter aluminum cylinder (fiber CSEM 100192B). In this case, $I_{max}$ and $I_{min}$ were simply measured behind a Glan-Thompson polarizer. We found that the orientation of the polarization was stable within ± 0.5 ° over a period of 8 minutes while the extinction ratio $I_{max}/I_{min}$ of the maximum and the minimum intensities was 125:1 over the same period. The thermal expansion of the aluminum cylinder can change the birefringence in the fiber amplifier, and thus the polarization state at output. In order to investigate this effect, we increased the temperature of the cylinder from 20 to 40 °C. The orientation of the polarization did not change more than 3 ° while the extinction ratio decreased almost to 1 (a circular polarization) as shown in

Fig. 4.8. However, it was possible to get the original polarization state simply by adjusting the polarization controller (point *A* in Fig. 4.8).

After a complete temperature cycle without correction of the polarization controller, the polarization state was slightly lower than the original value (point *B* in Fig. 4.8) but can be corrected.

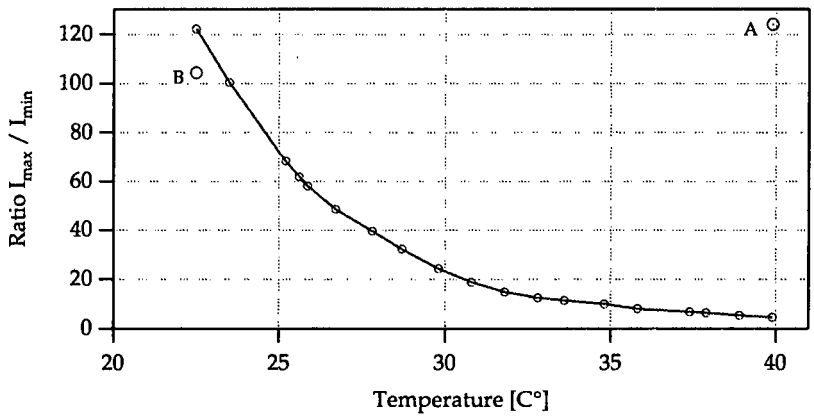


*Fig. 4.8: Variation of the polarization as a function of the temperature of the aluminum cylinder.*

This experiment demonstrates that the thermal stability of the fiber is a critical point for a coherent communication system. The temperature of the amplifier and the mechanical stability must be carefully controlled in order to maintain the polarization properties.

Then, we measured the polarization stability of a 12 m long amplifier coiled in a kidney shape (fiber IPHT 152 SK 4). The polarization state at the output of the passive (un-pumped) amplifier fiber is stable and the extinction ratio is always higher than 200:1 (Fig. 4.9 and Fig. 4.10).

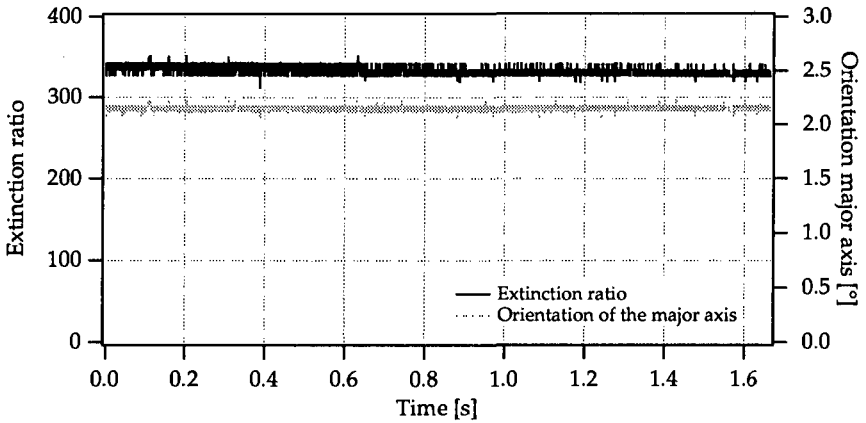


*Fig. 4.9: Stability over 1.6 s of the polarization state at the passive amplifier fiber output (fiber 152 SK4, 12 m long amplifier, coiled on kidney shape). The noise corresponds to a variation of 1 least significant bit of the analog-digital converter in the acquisition system. The sampling rate is 6 kHz.*

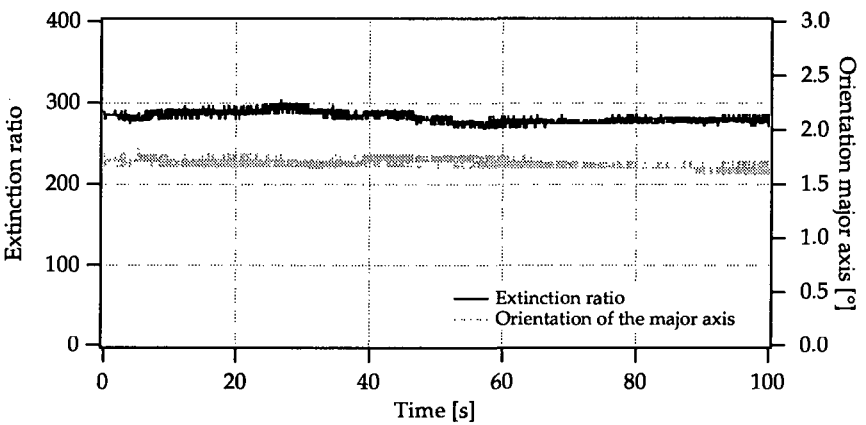


*Fig. 4.10: Stability over 1.5 min of the polarization state at the passive amplifier fiber output (see Fig. 4.9 for explanation on noise). The sampling rate is 100 Hz.*

With the amplifier active (pumped), the system becomes more sensitive to mechanical vibrations and to thermal fluctuations (Fig. 4.11). However, the extinction ratio is again well above 200:1. The variations of the polarization are slow (seconds) and can be corrected easily using a feed back loop.

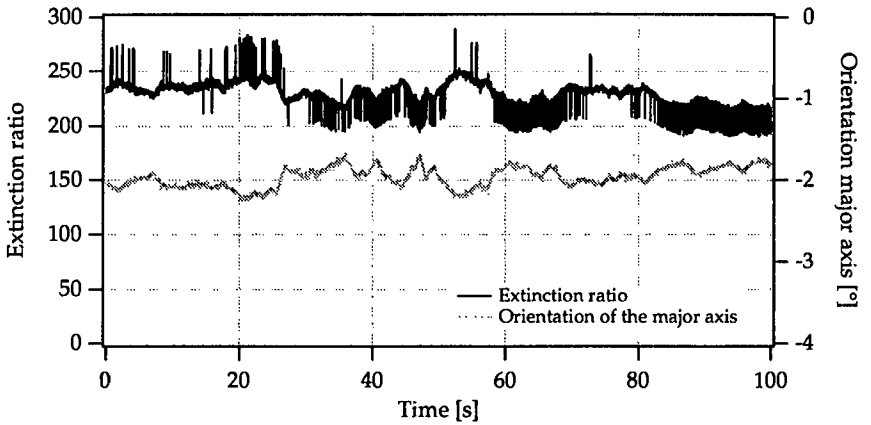


*Fig. 4.11: Stability over 1.5 min. of the polarization state at the active amplifier fiber output. The noise corresponds to a variation of 1 least significant bit of the analog-digital converter in the acquisition system. The sampling rate is 100 Hz.*

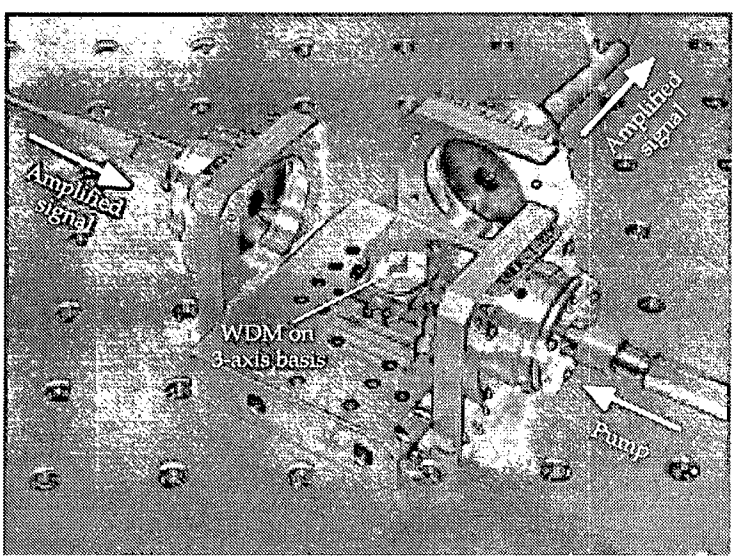


*Fig. 4.12: Detail of coupling system using Optics for Research (OFR) devices, for the realization of a miniaturized version of the fiber amplifier.*

# 4.4 Gain, Output power and power conversion efficiency

## 4.4.1 Methods for the measurement of the gain and the output power

In high power amplifiers, the amplified spontaneous emission (ASE) can be very important compared to the small input signal. Thus, synchronous detection is required. However, modulation of the input signal is not sufficient because, in the saturated gain regime, power is transferred from the ASE to the amplified signal. Therefore the ASE background is modulated in opposition to the signal and the lock-in amplifier sees only the difference between the amplified signal and the ASE level. Therefore, spectral filtering is needed to measure the gain accurately.

We used three methods to measure the gain: a narrow band-pass filter, a spectrometer and a heterodyne detection system. Filtering of the amplified spontaneous emission is achieved by all three methods.

A band-pass filter (1064 nm, FWHM = 3 nm) can be used. However, care must be taken when working with small signals which do not saturate completely the amplifier, because the ASE contribution in the filter bandwidth may be too high. Before using this method, we investigated carefully the ASE spectra under different working conditions.

A spectrometer is a better solution, because the bandwidth and the central wavelength of the filter can be set precisely to match the signal (Fig. 4.13). Moreover, the spectrometer can be used to analyze the ASE spectrum, as long as the system is stable during the acquisition time

Heterodyne detection is a powerful tool for gain measurement (Fig. 4.13). It is very sensitive and gives information on the gain and the phase noise of the amplifier (cf. § 5.3). The amplified signal interferes with the reference, producing the useful electrical beat signal. The ASE remains as a DC component in the electrical spectrum and thus, is filtered by the spectrum analyzer.

Both ends of the fiber amplifier are cleaved at an angle of 12° to prevent self-oscillation. The optical isolator (40 dB) is used to protect the Nd:YAG laser from amplifier noise. Two acousto-optic modulators, driven at 40 and 40.05 MHz, respectively, are used for the heterodyne detection. Pump and signal beam are separated with a dichroic filter. In this configuration, the signal is propagating in the opposite direction with respect to the pump beam and more output power is available [56]. The amplifier was pumped with a high power laser diode array from Fisba Optik. It delivers up to 23 W at 800 nm in a 332 x 186 $\mu m^2$ spot size.

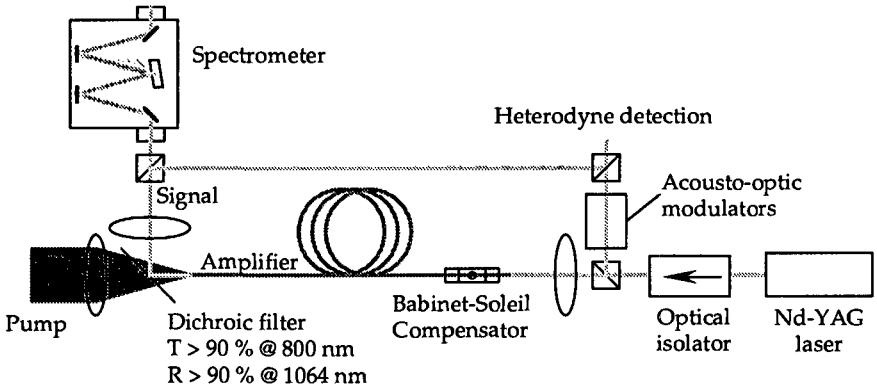


*Fig. 4.13: Set-up for the measurement of the gain, using either spectrometer or heterodyne detection.*

### 4.4.2 Gain and output power

Gain and output power for the 3 different fibers are shown in Fig. 4.14 and Fig. 4.15. As expected, the output power versus input power is almost flat (saturated) for short fiber amplifier lengths. In such a design, the system becomes insensitive to the power of the input signal. This allows more flexibility for the specified power of the master oscillator. Keeping the fiber short is also better in view of radiation hardness. For two samples of different lengths, radiation will induce larger distributed losses in the longer fiber.

The gain and the output power are now described with more details for each fiber.

*Fiber CSEM 100192 B*

Except for some early experiments (cf. § 4.2.2), the amplifier was backward pumped (with respect to the signal propagation) through the output end of the fiber (Fig. 4.13) with the Fisba source. Pump power coupling efficiency into the multi-mode core was measured to be around 23%, thus launching 5 W of the 23 W laser diode module. Assuming that the propagation losses for the pump beam in the multi-mode core are negligible [61] [45], measuring the remaining pump power at the other end of the amplifier gives a good estimation of the absorbed pump power. The gain and the output power were measured for a 8 m long amplifier coiled on 10 cm diameter aluminum cylinder. We achieved an output power of about 630 mW for 3.9 W absorbed pump power (Fig. 4.15). For an input signal of 35 mW, this gives a power conversion

efficiency (PCE, cf. § 4.4.3) of 15 % (Fig. 4.16). However, expressed as a fraction of the launched pump power, the efficiency is only 13 %.

*Fiber IPHT 45 SK 3*

The dopant concentration and the multi-mode core size are larger than for the CSEM fiber, so that higher output power was achieved. In a first configuration, we used a 24 m long amplifier, of which the first 12 m were coiled in a kidney shape (3 cylinders with a diameter of 30 mm, Fig. 4.2). In the second configuration, the last 12 m were removed. As much as 6.6 W of pump power was launched into the 200 µm multi-mode core and the absorbed pump power was 4.3 W and 3.8 W, respectively. This demonstrates clearly the importance of the coil shape; only 500 mW were absorbed in the last portion of the fiber, while the rest was absorbed in the first 12 m. In this configuration, we obtained 1.35 W and 1.2 W output power, respectively.

The properties of the two amplifiers are rather different; this is obvious when looking at the output power versus input power (Fig. 4.15). The 12 m long amplifier is completely saturated (constant output power) for signals above 6 mW. This means that the system is limited by the pump-photon to signal-photon conversion. But, due to the shorter absorption length, the output power is lower than for the longer amplifier. The 24 m long amplifier is more powerful, but we did not reach fully saturated output power. For small signals, a large ASE builds up in the first part of the amplifier and saturates the gain. This is obvious from the measured total output power of the amplifier, which remains constant. In our application, it is assumed that 10 mW are available at input of the amplifier, thus, only the short version is capable to give more than 1 W output power. For signal input power of 55 mW, the power conversion efficiency, referring to the absorbed pump power, is close to 30 % in both configurations (Fig. 4.16).

*Fiber IPHT 152 SK 4*

This fiber has the highest dopant concentration. The losses at signal wavelength are similar to the IPHT 45 SK 3 fiber. The cladding diameter is 180 µm and therefore only 5.6 W pump power could be launched. The absorbed pump power was measured to be 4 W. The output power was slightly below 800 mW (Fig. 4.15) and the PCE is around 20 %, referring to the absorbed pump power (Fig. 4.16) for a signal of 60 mW.

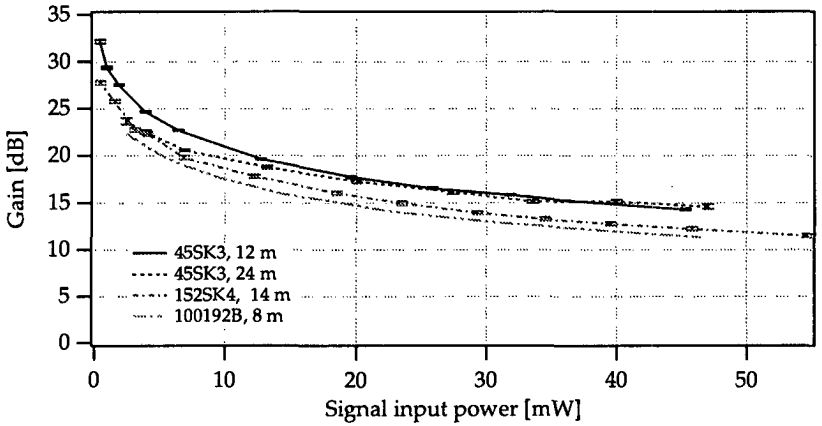


*Fig. 4.14: Gain for different fibers. For the 24 m long 45 SK 3 fiber amplifier, 12 m were coiled in kidney shape. The 12 m long 45 SK 3 fiber amplifier was completely coiled in kidney shape. The 152 SK 4 fiber was also coiled in kidney shape. The 100192 B was coiled on a cylinder.*

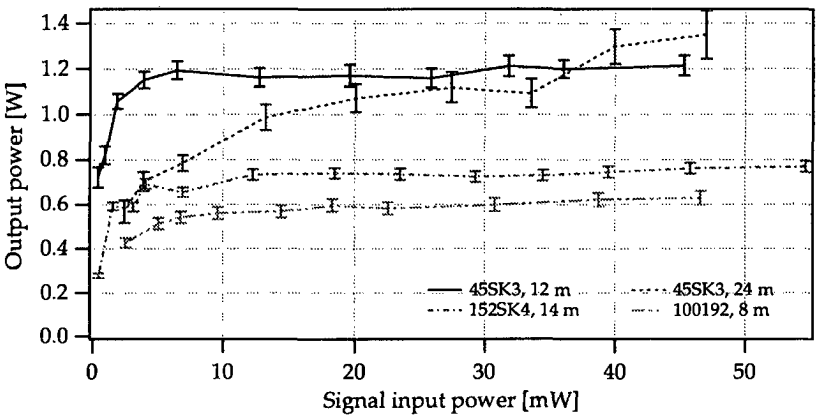


*Fig. 4.15: Output power for different fibers (for fiber lengths and coil shapes, see the caption of Fig. 4.14).*

### 4.4.3 Power conversion efficiency

The power conversion efficiency (PCE) of the amplifier is defined as

$$PCE = \frac{P_{s-out} - P_{s-in}}{P_{abs}}, \tag{4.9}$$

where $P_{s-in}$ is the power of the signal at amplifier input, $P_{s-out}$ is the amplified signal and $P_{abs}$ it the absorbed pump power. For a given absorbed pump power, and when the amplifier is in saturation, the PCE is constant with respect to the input signal. Sometimes, the power conversion efficiency is defined with respect to the launched pump power or even the total available pump power.

According to the ratio of the pump wavelength (800 nm) and the signal wavelength (1064 nm), the theoretical PCE is 75% (one pump photon per signal photon). The absorbed pump power was calculated subtracting the residual pump power at the amplifier output from the launched pump power, according to the assumption made at the beginning of the previous section.

In order to keep the amplifier as short as possible, though with a good efficiency, one could think that the highest dopant concentration is the best. This is obviously not the case when looking at the different PCE (Fig. 4.16). In fact, we reached an upper limit for the concentration, probably due to the fact that concentration quenching becomes a problem. Thus, 2 % of neodymium within the core is believed to be an optimum dopant concentration for such fiber amplifiers.

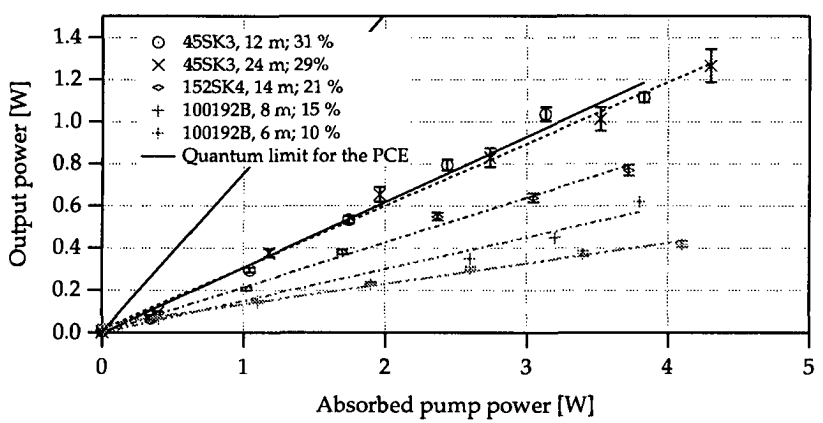


*Fig. 4.16: Power conversion efficiency (PCE) measured for different amplifiers (for fiber lengths and coil shapes, see the caption of Fig. 4.14)*

Losses at the signal wavelength do not depend on the dopant concentration (in 4 level systems, there is no re-absorption) but rather on the fabrication process. For a given process, a short fiber will have less distributed losses and will be more efficient. It is, however, not clear from the experimental results whether a low concentration for a given length would be more efficient than a high concentration or not. The fiber 100192 has much higher losses at 1.06 μm than the other one, so that direct comparison does not make sense. Nevertheless, there is probably a tradeoff between high concentration, which reduces the fluorescence lifetime (and thus the gain), and low concentration, which reduces the absorption. A much larger number of samples and extensive simulations are required to give a better answer.

### 4.4.4 Comparison with theoretical model

Using the model developed by Hardy and Oron [19] [20], we performed some calculation for the IPHT 45 SK3 double-clad doped fibers. The parameters are summarized in Table 4-3.

| Parameters for simulation | | |
|---|---|---|
| $P_s$ (input signal) | 10 | [mW] |
| $P_p$ | 6.6 | [W] |
| $\sigma_s$ | $2.5 \cdot 10^{-24}$ | [m²] |
| $\sigma_p$ | $2 \cdot 10^{-24}$ | [m²] |
| $\lambda_s$ | $1064 \cdot 10^{-9}$ | [nm] |
| $\lambda_p$ | $806 \cdot 10^{-9}$ | [nm] |
| $\alpha(\lambda_s)$ | -0.55 | [dB/m] |
| N (# of channel) | 15 | |
| $\Gamma_s$ | 0.75 | |
| $\Gamma_p$ | 0.15 | |

*Table 4-3: Parameters of fiber IPHT 45SK3 for numerical simulation.*

The computed output power and the measured values are reported in Fig. 4.17.

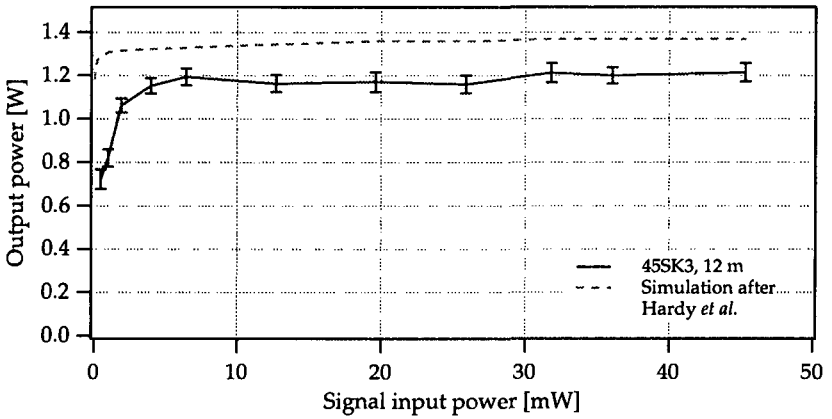


*Fig. 4.17: Comparison of experimental data with the simulation using the model of Hardy et al. [20]*

A few conclusions are obvious from these simulations.

The predicted output power is slightly higher than measured. This is probably due to an underestimation of signal loss or to some fluctuations of the dopant concentration. It has been shown that the dopant distribution can significantly vary over short fiber length [62], thus modifying the gain properties of the fibers. Verifications of these parameters require destructive methods; for this reason, they have not been carried out.

The output power for weak signals is much lower in the experiment than in the simulations. There is no obvious explanation for this discrepancy, though one may think that the assumption on concentration quenching is not fulfilled (see the reduction of fluorescent lifetime, Table 4-1).

Further simulations demonstrated that longer fibers (up to 20 m as in first experiment) would produce only slightly increased output power. Estimations of the absorbed pump power were also in good agreement with the simulations. As expected, the loss at signal wavelength is the key issue to increase the output power and the power conversion efficiency of the double-clad fiber amplifiers.

## 4.5 Dual-stage amplifiers

Double-clad doped fiber amplifiers pumped by laser diode arrays are capable of delivering up to 5 W [63] [64]. They show high gain and reasonable output power, as well as low spectral and phase noise. Although fiber lasers with up to 110 W cw have been demonstrated so far [65], they are limited in the output power due to nonlinear effects and damage threshold [66]. On the other hand, diode pumped solid-state amplifiers have high output power, but their gain is small in the Watt range compared to fiber amplifiers, requiring more powerful master oscillators. Such powerful oscillators are unfortunately not compatible with the power that phase modulators can handle. Thus, it seems evident to study the combination of both types of optical amplifiers in a two-stage device to obtain both high gain and high output power. The fiber amplifier (first stage) provides large gain and delivers an output power compatible with the input required for the solid-state amplifier. This second stage acts as a booster.

We combined a $Nd^{3+}$ -doped double-clad fiber and a Nd:YAG crystal amplifier and we obtained a single-mode, single-frequency output power of 3.5 W for a total gain of 28 dB.

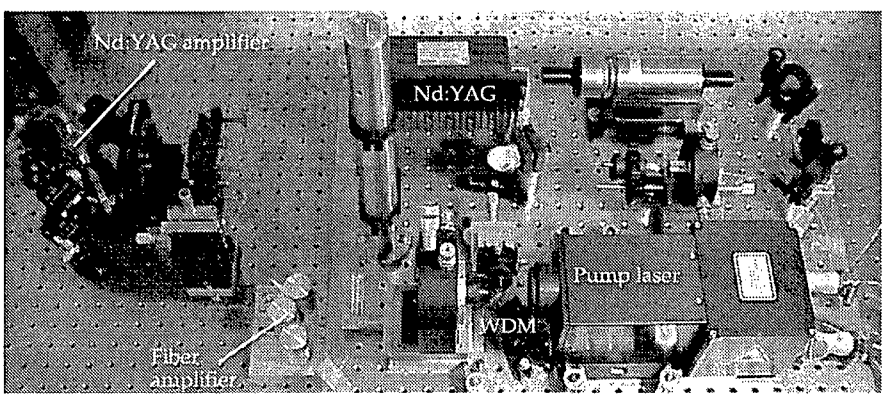


*Fig. 4.18: Dual-stage amplifier. The pump delivery system of the crystal amplifier has been removed for this picture.*

### 4.5.1 Design of the amplifier

*Fiber amplifier*

We used the 45 SK 3 $Nd^{3+}$ -doped fiber in the 8-m long configuration as first stage amplifier. Thus, we obtained 1 W saturated output power as already described in § 4.4.2 (cf. Fig. 4.15 for the output power of the first stage). This device is suitable for pre-amplification.

*Solid state Nd:YAG amplifier*

The second stage of the amplifier is based on two identical 1% doped Nd:YAG crystals (Fig. 4.19, top). It has been constructed and studied by U. Roth at IAP, University of Bern. A detailed description of the design and the results he got are given in [68]. The following description is a summary of this reference.

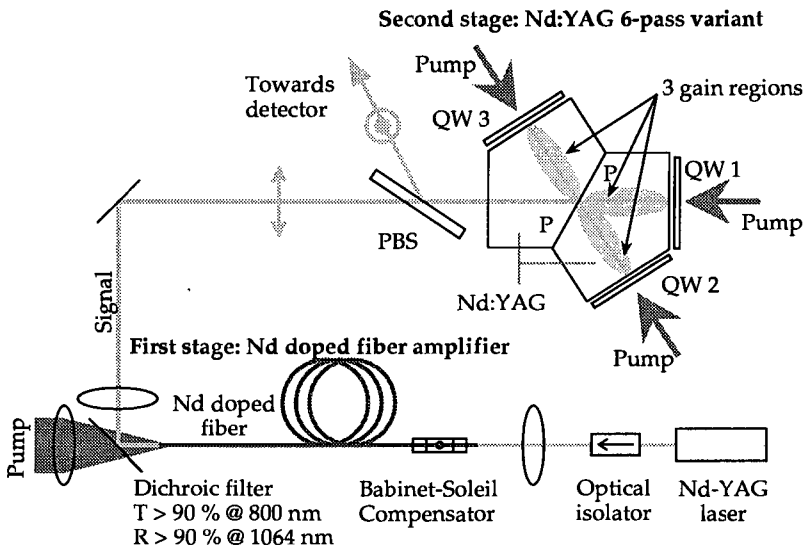


*Fig. 4.19: Dual-stage amplifier combining a fiber amplifier as first stage and a solid state amplifier as booster.*

The face marked P is coated as a dielectric polarizer; the other faces are anti-reflection (AR) coated for both 809 and 1064 nm. The quarter-wave plates have an AR coating for both 809 and 1064 nm on the side next to the crystal and on the other side they are coated as mirrors for 1064 nm and AR coated for 809 nm. The crystal length from the polarizer face P to the pump faces is 11 mm.

The horizontally polarized signal beam (corresponding to the drawing plane) passes the polarizer face marked P at Brewster's angle, then passes the quarter-wave plate QW1 and is reflected at its backside. Due to the double-pass through the quarter-wave plate, the polarization is rotated by 90°. Now the beam is reflected at the polarizer P and travels towards QW2. There, the polarization is rotated again and passes through the polarizer P towards QW3. Another double-pass through a quarter-wave plate rotates the polarization again; the beam (vertical polarization) is finally reflected at the polarizer P, exits the crystal in direction of the incoming beam and is separated by the polarizing beam-splitter (PBS). Altogether, the signal passes 2 times in each of the 3 gain regions.

The pump power is delivered by three fiber-coupled diode laser modules (Jenoptik AG, Jena, Germany). The fibers have a core diameter of 600 µm and a NA of 0.22. The spectrum of the pump radiation is centered at 809 nm and has a width of 2 nm (FWHM). Each fiber delivers up to 10 W of pump radiation that are focused onto the crystal by a micro-objective. The transmittance of the focusing optics and the quarter-wave plates was measured to be 87 %. Thus, there was an incident power on the crystal of 3 x 8.7 W. The crystal itself was mounted on a fully adjustable holder with a copper heatsink on its upper and lower face to remove the generated heat. In this configuration, we obtained an output power up to 7 W (Fig. 4.20, bottom curve) with a gain of 4.7 dB. The input beam was from a 2.7 W Nd:YAG $TEM_{00}$ mode laser. As the gain is small, this amplifier will be used best as a booster.

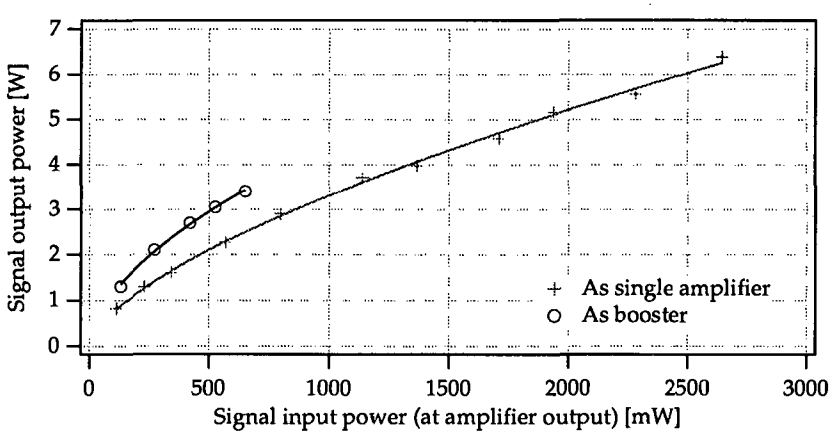


*Fig. 4.20: Output power of the solid state amplifier working as booster (upper curve) and as single amplifier (lower curve).*

*Dual-stage system*

The output beam from the fiber amplifier is launched into the crystal, forming a two-stage configuration (Fig. 4.19). The coupling efficiency between the two amplifiers (the ratio of the crystal output without pump and the fiber amplifier output) is 60 %, including the transmission losses through the coupling optics, the crystal, the polarizers and the quarter-wave plates.

We know from the study of the fiber amplifier that there is no amplified spontaneous emission (ASE) for input signals larger than 5 mW. The second stage will act as a booster for the signal, without introducing further ASE. The first stage is working in saturation; the output power is not sensitive to the signal input power. This is not the case for the booster so that it is not possible to extract the complete available power.

In a first experiment, the combination of the two amplifiers produces a total output power of 2.8 W for a gain of 27.5 dB at the beginning of the saturation (Fig. 4.21), a result that cannot be reached in one stage. The first stage delivers 1.1 W with a gain of 23.4 dB. The launched pump power is 6.6 W and the PCE referring to the launched pump power is 17 % (cf. chapter 4). The second stage gives 2.8 W with a gain of 4.1 dB. With the 26 W of pump power launched into the crystal, we obtain a PCE of 9 %.

After optimization of the system alignment, the total output power was increased up to 3.5 W. The output versus input power of the second stage in this optimized case is shown in Fig. 4.20 (upper curve). The values are slightly higher compared with the measurement as single stage. This is probably due to the better mode quality of the beam.

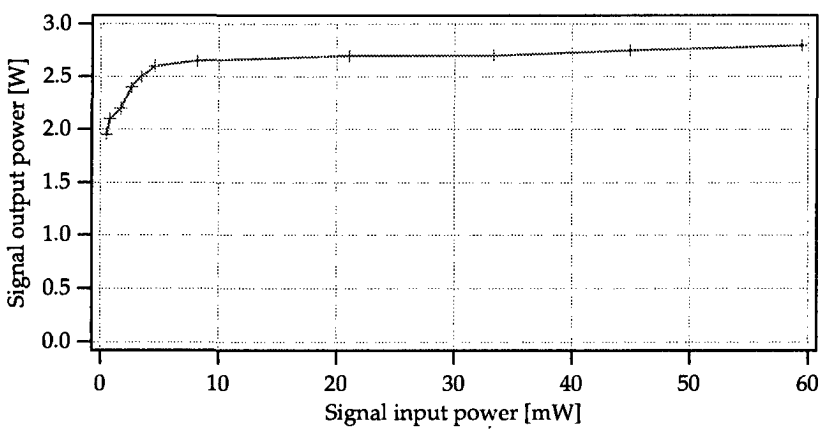


*Fig. 4.21: Total output power of the dual-stage amplifier.*

### 4.5.2 Performance of the combined amplifier

Due to the fact that the fiber amplifier is operating in saturation, the output power is no longer sensitive to intensity variations of the input signal and the amplification increases monotonically with the pump power. The total output power may be easily scaled to a few tens of watts, according to power levels currently available in solid-state lasers. Thus, it seems evident that two-stage amplifiers are a viable solution to achieve both high gain and high output power with single-frequency emission, as required for coherent communication. However, for space applications, it is necessary to shield the fiber amplifier carefully against ionizing radiation, or, in case of longtime missions, to use radiation hardened fiber types.

The output power in our experiment was limited by the crystal amplifier, which cannot be driven into saturation. Thus, it was not possible to extract all the available power. However, fiber amplifiers with more than 5 W have already been demonstrated ([63], [64]) so that, using these as first stages, we can expect at least 10 W out of the booster crystal (Fig. 4.20). Moreover, Nd:YAG lasers of a few tens of Watts are already available, showing that this second stage may be scaled to even higher power.

To the best of our knowledge, this is the first demonstration of two-stage amplifiers combining the advantages of fiber and crystal amplifiers. It opens new possibilities in the field of high performance coherent space communications.

# 5 Noise in fiber amplifiers

OPTICAL amplifiers, as all active devices, add some noise to the amplified signal. A better understanding of the different noise contributions is necessary to asses the influence on a coherent communication system.

Coherent communication systems are normally based on binary phase or frequency modulation rather than on amplitude modulation. Thus, amplitude noise, mainly related to pump stability, is not a critical point. Amplified spontaneous emission may be more annoying because it reduces the efficiency of the amplifier and can saturate the detector in a bandwidth close to the signal. Phase noise, the most critical contribution, depends mainly on the spectral width of the amplified signal. For narrow linewidth signals, it is negligible, allowing coherent detection with large modulation bandwidth.

In section 5.1 we briefly define the noise figure and, in section 5.2, we present some experimental investigations on amplified spontaneous emission (ASE). Phase noise is discussed in detail in section 5.3. First, the theoretical models are developed. Then, the experimental results are presented and analyzed.

## 5.1 Effect of an optical amplifier on the signal-to-noise ratio, noise figure

When an optical amplifier is present in the transmission chain, some noise is added by amplified spontaneous emission (ASE) (Fig. 5.1).

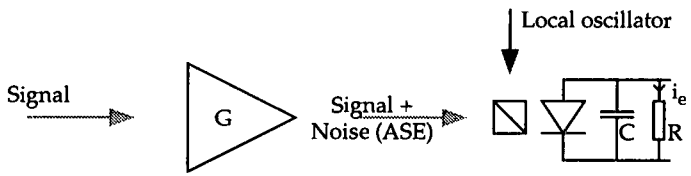


*Fig. 5.1: Effect of the amplifier in the transmission chain.*

For coherent detection, the total noise power within the detector bandwidth is found to be ([1] Eq. 3.100)

$$< \Delta i^2_{noise} >= \sigma_d^2 = \sigma_{sn}^2 + \sigma_{lo-ASE}^2 + \sigma_{s-ASE}^2 + \sigma_{ASE-ASE}^2 + \sigma_{th}^2, \tag{5.1}$$

where $\sigma_{sn}$ is the shot noise, $\sigma_{lo\text{-}ASE}$, $\sigma_{s\text{-}ASE}$ and $\sigma_{ASE\text{-}ASE}$ are the local oscillator-ASE, signal-ASE and ASE-ASE beat noise, respectively, and $\sigma_{th}$ is the thermal noise (as defined in Eq. (3.7)).

From Eq. (3.6), including gain $G$ on the signal and the contribution of ASE, we derive the shot noise contribution

$$\sigma_{sn}^2 = 2eB_e\eta\left(\frac{P_{lo}e}{h\nu} + \frac{GP_s e}{h\nu} + 2\frac{P_{ASE}e}{h\nu}\right), \tag{5.2}$$

where $2P_{ASE}$ is the mean ASE power within the optical bandwidth $B_o$ of the amplifier, referred to as the equivalent input noise of the amplifier and given by [1] (section 5.7)

$$P_{ASE} = n_{sp}h\nu B_o(G-1). \tag{5.3}$$

The term $n_{sp}$ in Eq. (5.3) is the spontaneous emission factor (defined in [1] chapter 2). In the particular case of 4-level systems, $n_{sp}$ equals unity. Note also that the ASE power is considered in two polarization modes, as it is usually the case for fiber amplifiers. The other contributions to the noise are given as ([1] Eq. 3.101-3.104)[2]

$$\sigma_{lo-ASE}^2 = 4\eta^2 P_{ASE}\cdot P_{lo}\cdot\left(\frac{e}{h\nu}\right)^2\frac{B_e}{B_o} \tag{5.4}$$

---

[2] A complete derivation of these noise components is given in the book of Desurvire [1] and is beyond the scope of this text. We only intend to show the effect of amplifier noise and the influence on a coherent communication system.

$$\sigma^2_{ASE-ASE} = 4\eta^2 G P_s \cdot P_{ASE} \cdot \left(\frac{e}{h\nu}\right)^2 \frac{B_e}{B_o} \tag{5.5}$$

$$\sigma^2_{s-ASE} = 2\eta^2 P^2_{ASE} \cdot \left(\frac{e}{h\nu}\right)^2 \frac{2B_e}{B_o}. \tag{5.6}$$

Substituting Eqs. (5.2) to (5.6) into (3.8) and after some simplifications, we get for the electrical signal-to-noise ratio (SNR)

$$SNR = \frac{\frac{\eta P_s}{B_e h\nu}}{\eta\left(1+\frac{GP_s}{P_{lo}}\right)\left(\frac{2n_{sp}(G-1)}{G}+\frac{1}{\eta G}\right)+\frac{2P_{ASE}}{GP_{lo}}\left(1+\eta n_{sp}(G-1)\right)+\frac{\sigma_{th} h\nu}{2GB_e P_{lo}\eta e^2}}. \tag{5.7}$$

We can distinguish three different cases for the SNR, according to the power level of the local oscillator and the gain of the amplifier.

*Amplifier off, G=1*

When the amplifier is turned off, the gain $G = 1$ and $P_{ASE} = 0$ according to Eq. (5.3). Thus, the SNR becomes

$$SNR = \frac{\frac{\eta P_s}{B_e h\nu}}{\left(1+\frac{P_s}{P_{lo}}\right)+\frac{\sigma_{th} h\nu}{2B_e P_{lo}\eta e^2}}. \tag{5.8}$$

Moreover, if the power of the local oscillator is sufficiently high, Eq. (5.8) further reduces to

$$SNR = \frac{\eta P_s}{B_e h\nu}, \tag{5.9}$$

as expected by a shot noise limited communication without amplification (see Eq. (3.12)).

*High power local oscillator*

For G>1 and when the power of the local oscillator is high, the SNR at the amplifier output is given by

$$SNR = \frac{\frac{P_s}{B_e h\nu}}{\frac{2n_{sp}(G-1)}{G}+\frac{1}{\eta G}}. \tag{5.10}$$

The numerator in Eq. (5.10) corresponds to the optical shot noise limit, thus, to the SNR(0) at the amplifier input. Therefore, we can write Eq. (5.10) as

$$F_0 = \frac{SNR(0)}{SNR(z)} \text{ with } F_0 = \frac{2n_{sp}(G-1)}{G}+\frac{1}{\eta G}, \tag{5.11}$$

where the noise figure $F_0$ is a measurement of the degradation of the optical signal-to-noise ratio for a signal passing through the optical amplifier.

*High gain optical amplifier and high power local oscillator*

When both the power of the local oscillator and the gain are large, the SNR is dominated by the LO-ASE beat noise and (5.7) reduces to

$$SNR = \frac{P_s}{2n_{sp}B_e h\nu}, \tag{5.12}$$

which is independent of the photodetector quantum efficiency. When compared with an ideal direct detection, assuming $\eta = 1$ in Eq. (3.12), optical amplifiers introduce an excess noise of 3 dB in the SNR. However, in the case of real photodetectors, for which $\eta < 1$, the optical amplification can enhance the electrical SNR (see for instance a discussion in [1] section 3.3). Note that, in this case, the noise figure $F_0 = 2$.

## 5.2 Amplified spontaneous emission

Amplified spontaneous emission (ASE) is filtered by the heterodyne (coherent) detection so that no additional band-pass filter is required for the detection. However, large ASE is not desirable in optical amplifiers, because it reduces the signal-to-noise ratio and the power available in the amplified signal.

We measured ASE spectra for different configurations, using a spectrometer as for the measurement of the gain (Fig. 4.13). Turning the signal on resulted always in a transfer of the ASE into the amplified mode (Fig. 5.2). The ASE power represents less than 10 % of the output power for both the IPHT 45 SK 3 and 152 SK 4 fibers in the saturated regime, i.e. for signals above 10 mW.

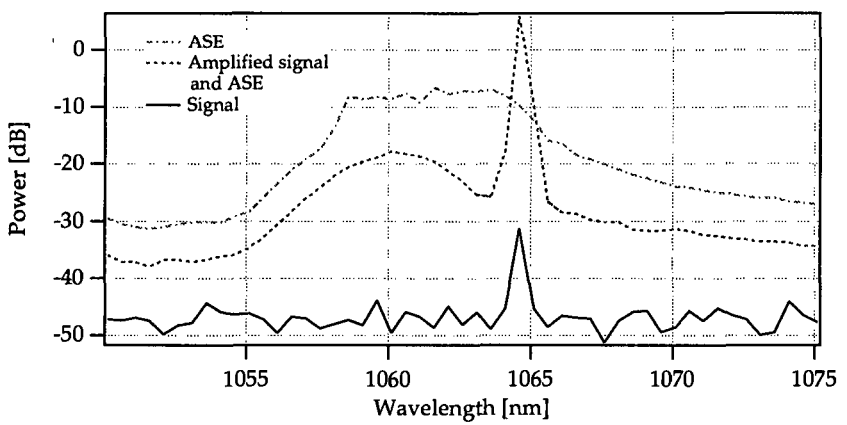


*Fig. 5.2: Signal spectrum, ASE spectrum and amplified signal spectrum of fiber IPHT 152 SK 4. Amplifier 14 m long, coiled in kidney shape. Signal power 0.13 mW; output power 695 mW; gain of 37.5 dB. Spectra measured with a Jobin-Yvon HR 460 monochromator (resolution 0.5 nm).*

The output spectrum for the 152 SK 4 fiber with the amplifier working in saturation is shown in Fig. 5.3. We can clearly see the reduction of the ASE.

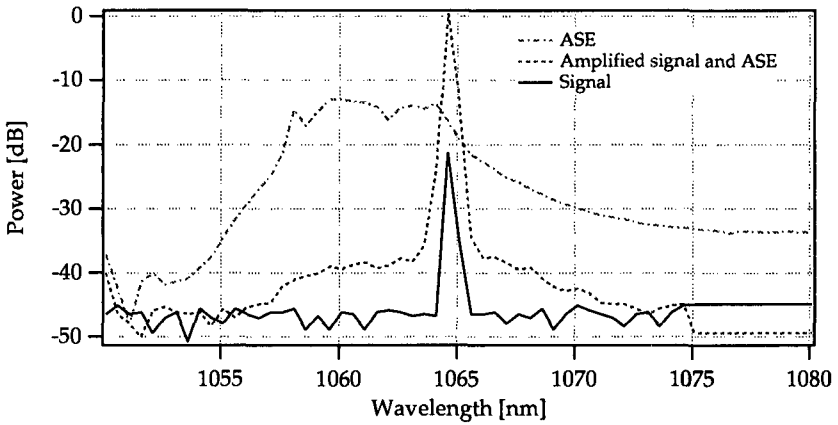


*Fig. 5.3: Same as Fig. 5.2, but with signal power 5 mW, total output power 730 mW and gain of 21.6 dB.*

## 5.3 Phase noise

A semiclassical model for the fundamental noise limit of linear amplifiers has been developed by Heffner in 1962 [69]. This model predicts a phase noise which depends on the optical linewidth of the input signal. In 1990, experimental results were published by Cowle [70], which showed a spectral broadening of the signal linewidth due to the phase noise added by an optical fiber amplifier. The spectral broadening was explained by the so called "modified semiclassical model" [71], following the general treatment of line broadening due to phase noise in lasers (see for instance [14]). Following the same approach, Desurvire [1] derived the semiclassical model, which predicts spectral broadening much smaller than those measured in [70]. Recently, measurements published by Möller [72] indicated that spectral broadening due to fiber amplifier was not as large as predicted in [71]. In order to clarify these findings, we decided to measure the noise introduced by our high power fiber amplifiers for different linewidths of the input signal.

Following the treatment of Heffner, we will first find the lower limit of the phase noise given by the uncertainty principle of Heisenberg. Then, following the treatment of Desurvire, we will establish the semiclassical model, which describes the spectral broadening due to phase noise. We will then compare these results to the model developed by Cowle. Finally, we will propose a different model where the phase noise is introduced as an additive noise rather than a multiplicative noise. The experimental results will finally reveal the appropriate model.

### 5.3.1 Uncertainty principle

Heffner [69] based his investigation of phase noise on the uncertainty principle of Heisenberg. In the following, we summarize this approach.

The uncertainty principle can be applied to the measurement of phase and photon number through

$$\Delta n \Delta \phi \geq \frac{1}{2}, \tag{5.13}$$

where $\Delta n$ and $\Delta \phi$ are the uncertainty of the number of detected photons and of the measured phase, respectively. In the case of an ideal linear amplifier, given a number of input photons $n_1 \pm \Delta n_1$, the output power will be $Gn_1 \pm G\Delta n_1$. Let us assume now that the amplifier is followed by an ideal detector, sensitive to both phase and amplitude and with quantum efficiency equal to 1. The detector will measure the signal with the uncertainty $\Delta n \Delta \phi = 1/2$ which corresponds to an uncertainty of $\Delta n \Delta \phi = 1/2G$ at amplifier input. This clearly is not possible. Thus, the amplifier must add some noise!

We assume now a noisy amplifier followed by an ideal detector measuring both photon number and phase with a unity quantum efficiency, as shown in Fig. 5.4.

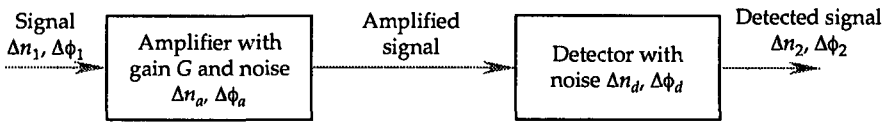


*Fig. 5.4: Noise for detection with an optical amplifier.*

In the following equations, the indices $a$ and $d$ are for the amplifier and the detector, respectively. Indices 1 and 2 refer to the input and the output signal, respectively. The variance of the phase and of the mean number of photons at the output of the system is given by

$$\begin{aligned} \Delta n_2^2 &= \Delta n_a^2 + \Delta n_d^2 \\ \Delta\phi_2^2 &= \Delta\phi_a^2 + \Delta\phi_d^2 \ . \end{aligned} \tag{5.14}$$

Multiplication of the terms in (5.14), assuming that $\Delta n_d \Delta\phi_d = 1/2$, leads to

$$\Delta n_2^2 \Delta\phi_2^2 = \Delta n_a^2 \Delta\phi_a^2 + \frac{1}{4} + \frac{\Delta\phi_a^2 \Delta\phi_d}{2\Delta n_d}\left(\frac{\Delta n_a^2}{\Delta\phi_a^2} + \frac{\Delta n_d^2}{\Delta\phi_d^2}\right). \tag{5.15}$$

The ratio $\Delta n_d/\Delta\phi_d$ is still open. The best detection is achieved when $\Delta n_2 \Delta\phi_2$ is minimized with respect to $\Delta n_d/\Delta\phi_d$, which leads to

$$\frac{\Delta n_a}{\Delta\phi_a} = \frac{\Delta n_d}{\Delta\phi_d}. \tag{5.16}$$

If we look at the input of the system, Eq. (5.14) can be written in the form

$$\begin{aligned} \Delta n_1^2 &= \frac{1}{G^2}\left(\Delta n_a^2 + \Delta n_d^2\right) \\ \Delta\phi_1^2 &= \Delta\phi_a^2 + \Delta\phi_d^2 \end{aligned} \tag{5.17}$$

and Eq. (5.15) becomes

$$\Delta n_1^2 \Delta\phi_1^2 = \frac{1}{G^2}\left[\Delta n_a^2 \Delta\phi_a^2 + \frac{1}{4} + \frac{\Delta\phi_a^2 \Delta\phi_d}{2\Delta n_d}\left(\frac{\Delta n_a^2}{\Delta\phi_a^2} + \frac{\Delta n_d^2}{\Delta\phi_d^2}\right)\right]. \tag{5.18}$$

After substitution of (5.16) in (5.18) and with $\Delta n_1 \Delta\phi_1 = 1/2$, we find that

$$\Delta n_a \Delta\phi_a = \frac{G-1}{2}. \tag{5.19}$$

For a signal with white Gaussian noise, which is the case for amplified spontaneous emission, the phase error is given by [69]

$$\Delta\phi_a^2 = \frac{P_N}{2P_S}, \tag{5.20}$$

where $P_S$ is the power of the signal and $P_N$ is the power of the noise.

*Noise power* $P_N$

We assume that the amplifier generates an ASE field $E_N(t)\cdot e^{i\phi t}$ where $E_N(t)$ and $\phi(t)$ are random time-varying amplitude and phase terms. Noise results then from the superposition of the amplified signal and the ASE field. It is obvious from Fig. 5.5, that the in-phase component of the ASE ($E_1$) is responsible for amplitude noise, while the quadrature component ($E_2$) is responsible for phase noise.

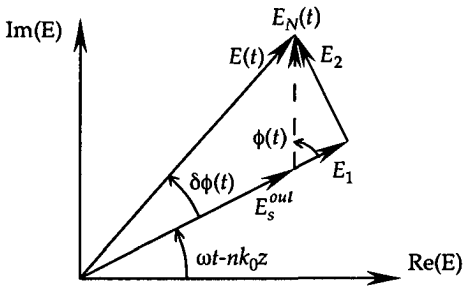


*Fig. 5.5: Semiclassical phasor model for the ASE-induced phase noise. $E_s$ is the amplified signal, $E_N$ is the ASE contribution and E is the resulting signal (after [1]).*

The variance of the power at the output of the optical amplifier is related to the photon number variance through

$$\Delta P^2 = (h\nu/T)^2 \Delta n_a^2, \tag{5.21}$$

where $T$ is the integration time. The mean value $<P>$ is given by

$$\langle P\rangle = \left\langle |E_S + E_N|^2 \right\rangle = \left\langle |E_S|^2 + |E_N|^2 + E_S E_N^* + E_S^* E_N \right\rangle, \tag{5.22}$$

where we have used Fig. 5.5 for the definition of $P$. Then,

$$\begin{aligned}\left\langle P^2 \right\rangle = \; & \left\langle |E_S|^4 + |E_N|^4 + E_S^2 E_N^{*2} + E_S^{*2} E_N^2 + 2|E_S|^2|E_N|^2 + 2|E_S|^2 E_S E_N^* + 2|E_S|^2 E_S^* E_N \right. \\ & \left. +2|E_N|^2 E_S E_N^* + 2|E_N|^2 E_S^* E_N + 2E_S E_S^* E_N E_N^* \right\rangle\end{aligned} \tag{5.23}$$

Using the definition of the variance $<\Delta P^2> = <(P-<P>)^2> = <P^2>-<P>^2$, and after simplification of Eq. (5.23), we get for the variance of the power

$$\left\langle \Delta P^2 \right\rangle = 2P_S P_N. \tag{5.24}$$

Combining Eqs. (5.24) and (5.21) into (5.19), using Eq. (5.20) gives the noise power

$$P_N = h\nu B(G-1), \tag{5.25}$$

where $B \approx 1/2T$ is the optical bandwidth of the amplifier.

Substituting (5.25) into (5.20) and replacing the signal power $P_S$ at the amplifier output by the signal input power $P_s^{in}$ multiplied by the gain ($P_S = GP_s^{in}$) finally gives

$$\Delta\phi_a^2 = \frac{h\nu B(G-1)}{2GP_s^{in}}. \tag{5.26}$$

This is the smallest phase fluctuation added by the amplifier and compatible with the uncertainty principle.

### 5.3.2 Semiclassical description of phase noise: a phasor model

The spectral broadening of laser oscillator linewidth due to the phase noise introduced by the spontaneous emission is often described through a phasor model ([1] section 5.7, [14] section 10.7). Since the phenomena are apparently the same in the case of optical amplifiers, namely spontaneous emission, the same derivation is used.

The mean ASE power in the bandwidth $B_o$ is given by (5.3).

$$P_{ASE} = n_{sp} h\nu B_o (G-1), \tag{5.27}$$

where $n_{sp}$ is the spontaneous emission factor (defined in [1] chapter 2), an equivalent input noise describing the nature of the optical amplifier. The mean arrival time $t_{ASE}$ between ASE photons is the reciprocal of the photon flux, so that

$$t_{ASE} = \frac{1}{n_{sp} B_o (G-1)}. \tag{5.28}$$

If we assume a single spontaneous emission event (one ASE photon) and a number of signal photons which is much larger than 1, the effect of this ASE photon on the phase is found to be (Fig. 5.6)

$$\tan(\delta\phi_1) \approx \delta\phi_1 = \frac{1}{\sqrt{< n_s >}} \sin(\phi). \tag{5.29}$$

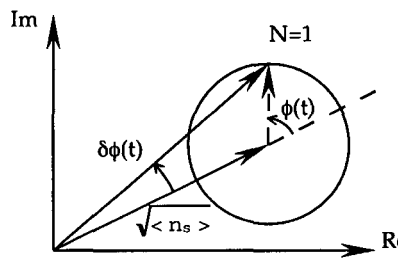


*Fig. 5.6: Phase deviation associated with one single spontaneous photon (N=1) with random phase; the mean signal photon number is $<n_s>$ and the corresponding mean signal field is $\sqrt{< n_s >}$ (after [1]).*

Averaging over a large number of events, the standard deviation of the phase is

$$\Delta\phi = \sqrt{< \delta\phi_1^2 >} = \frac{1}{\sqrt{2 < n_s >}}. \tag{5.30}$$

Assuming that the amplified signal power is given by $GP_s^{in}$, the number of photons detected during the time $t_{ASE}$ is given by

$$\langle n_s \rangle = \frac{GP_s^{in}}{h\nu} \frac{1}{n_{sp} B_o (G-1)}. \tag{5.31}$$

Combining (5.30) and (5.31), we obtain for the standard deviation of the phase, induced by spontaneous emission during $t_{ASE}$,

$$\Delta\phi = \sqrt{\frac{n_{sp}h\nu B_0(G-1)}{2GP_s^{in}}}. \tag{5.32}$$

Eqs. (5.32) and (5.26) differ only by the definition of $B_0$ ($B_0 = 2B$) and by the $n_{sp}$ term. It is not clear in Desurvire's book where the factor 2 comes from, but it is probably to take into account the 2 polarizations of the ASE noise (see § 5.1 and the comment on Eq. (5.3)). At high pump power, $n_{sp}$ is essentially unity so that both approaches lead finally to the same result.

Following the derivation of the spectral broadening of laser linewidth ([1] section 5.7), Desurvire proposed to relate the variance of the phase due to ASE to the linewidth of the amplified signal. Assuming that the spectrum of the signal is a Lorentzian defined by its full width at half maximum (FWHM) $\delta\nu$, and that the emission of spontaneous photons follows a Gaussian law, than the variance of the phase is related to the linewidth of signal by [14]

$$\Delta\phi^2 = \frac{2\pi\delta\nu}{B_0}. \tag{5.33}$$

From Eqs. (5.32) and (5.33), we find the equivalent linewidth broadening ([1], Eq. 5.77)

$$\delta\nu_{Desurvire} = \frac{n_{sp}h\nu B_0(G-1)}{4\pi GP_s^{in}}B_0. \tag{5.34}$$

We see from Eq. (5.34) that the phase deviation is small for large input power. This is also obvious when looking at Fig. 5.6. Moreover, the spectral broadening is independent of the gain when the gain is sufficiently high ($G > 20$ dB), which is the case in our amplifiers.

### 5.3.3 The "Cowle" model

Cowle developed his model before the publication of the book of Desurvire. The arguments presented by Cowle in his Ph.D. thesis are not very clear, but are reproduced here as faithfully as possible.

Cowle [70] measured line broadening due to amplifier noise and found values much larger than those predicted by the semiclassical theory. Using the same arguments as for Eq. (5.33), he got a relation for the variance $\Delta\theta$ of the phase in the amplified signal of linewidth $\Delta\nu_s$ for an observation time equal to the mean photon arrival time $t_{ASE}$, as defined in Eq. (5.28). The results is ([71] chapter 6)

$$\Delta\theta^2(t_{ASE}) = 2\pi\Delta\nu_s t_{ASE} = \frac{2\pi\Delta\nu_s}{n_{sp}B_0(G-1)}. \tag{5.35}$$

The average number of the signal noise photons in the output signal during the time for the detection of one ASE photon is given by the phase deviation of the laser signal during $t_{ASE}$ (Eq. (5.35)) divided by the phase deviation induced by one ASE photon (Eq. (5.30))

$$n_{spont} = \frac{\Delta\theta(t_{ASE})}{\Delta\phi}. \tag{5.36}$$

Using Eqs. (5.32) and (5.35) in (5.36), one gets for the average number of photon noise

$$n_{spont} = \sqrt{\frac{4\pi\Delta\nu_s G P_s^{in}}{n_{sp}^2 h\nu B_0^2 (G-1)^2}}. \tag{5.37}$$

Cowle assumed in his Ph.D. dissertation ([71] chapter 6) that «the amount of spectral broadening measured by the detector can be approximated in proportion of the signal spectral width as:

$$\delta\nu_{Cowle} \approx \frac{1}{n_{spont}} \Delta\nu_s, \tag{5.38}$$

([71] p 176)» so that, combining Eqs. (5.37) and (5.38) one finally gets

$$\delta\nu_{Cowle} \approx \sqrt{\frac{m^2 n_{sp}^2 h\nu B_0^3 (G-1)^2}{4\pi G P_s^{in}}}, \tag{5.39}$$

where $m = B_0/\Delta\nu_s$.

### 5.3.4 Comparison

Eqs. (5.32) and (5.39) are related through

$$\delta\nu_{Cowle} \approx \sqrt{n_{sp} B_0 (G-1) \cdot \delta\nu_{Desurvire}}, \tag{5.40}$$

where we have assumed that $m = 1$ in Eq. (5.39).

The spectral broadening predicted by Cowle is much larger because of the factor $n_{sp}B_0(G-1)$ and the variation of the broadening with the signal input power is reduced compared with the semiclassical approach, because of the square root.

We computed the value of the spectral broadening according to Eqs. (5.32) and (5.39), for a gain of 20 dB, a wavelength of 1.06 μm and for different signal linewidth $\Delta\nu_s$, as a function of the input power. We see clearly the large difference between these two models (Fig. 5.7).

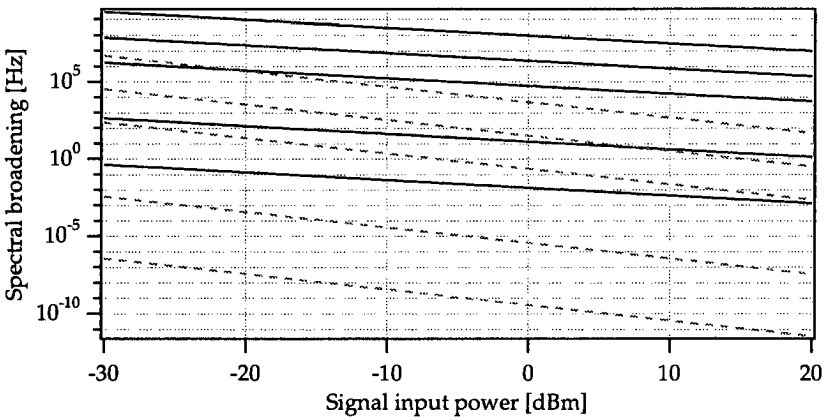


*Fig. 5.7: Spectral broadening according to Cowle (continuous lines) and Desurvire (dashed lines). From top to bottom: Δν = 18 GHz, 1.5 GHz, 125 MHz, 500 kHz, 5 kHz. The gain is 20 dB and the wavelength is 1.06 μm.*

### 5.3.5 Method for the measurement of phase noise

According to the approach described so far, the effect of the phase noise is assumed to broaden the linewidth of the signal. Thus, it is straightforward to use a Mach-Zehnder interferometer as the standard method for linewidth characterization. The amplifier is placed within one arm of the interferometer so that the spectral broadening induced by the ASE can be measured at the Mach-Zehnder output (Fig. 5.8).

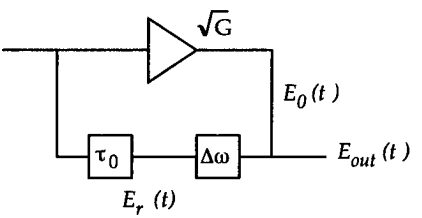


*Fig. 5.8: Mach-Zehnder interferometer for the measurement of phase noise.*

Due to the spontaneous nature of the ASE field considered in phase noise, it is possible to follow the same derivation as for laser linewidths (for example, see Yariv [14] § 10.7), namely to calculate the autocorrelation function at the output of the interferometer and to find the corresponding spectrum using Fourier transformation (Wiener–Kinchine relation).

Cowle assumed that the phase noise of the amplifier contributes to the system as a multiplicative noise [71], so that the signal at the output of the interferometer is given by

$$E_{out}(t) = \sqrt{G}E_0 \cdot e^{i\phi(t)} \cdot e^{iwt} \cdot e^{i\phi_a(t)} + E_r \cdot e^{i\phi(t+\tau_0)} \cdot e^{i(w+\Delta\omega)(t+\tau_0)}, \tag{5.41}$$

where $E_0$ and $E_r$ are the amplitude in the signal and reference arm respectively, $\tau_0$ is the delay of the interferometer, $\Delta\omega$ is the frequency shift introduced by the acousto-optic modulator, $G$ is the intensity gain of the amplifier, $\phi$ is the phase noise of the signal and $\phi_a$ is the phase noise due to the amplifier. In this approach, the noise is produced by the gain.

The autocorrelation function of the intensity at output of the interferometer is given by

$$\begin{aligned}\Gamma(\tau) = \; & G^2E_0^4 + 2GE_0^2E_r^2 + E_r^4 \\ & + GE_0^2E_r^2 \cdot \left\langle e^{i\left[\Delta\phi_{\tau_0}(t) - \Delta\phi_{\tau_0}(t+\tau)\right]} \right\rangle \cdot \left\langle e^{i\left[\phi_a(t) - \phi_a(t+\tau)\right]} \right\rangle \cdot e^{i\Delta\omega\tau} \\ & + GE_0^2E_r^2 \cdot \left\langle e^{-i\left[\Delta\phi_{\tau_0}(t) - \Delta\phi_{\tau_0}(t+\tau)\right]} \right\rangle \cdot \left\langle e^{-i\left[\phi_a(t) - \phi_a(t+\tau)\right]} \right\rangle \cdot e^{-i\Delta\omega\tau},\end{aligned} \tag{5.42}$$

where $\tau$ is the delay of the autocorrelation function and $\Delta\phi_{\tau_0}(t) = \phi(t) - \phi(t+\tau_0)$. In the particular case of a matched path interferometer, (5.42) reduces to

$$\begin{aligned}\Gamma(\tau) = \; & G^2E_0^4 + 2GE_0^2E_r^2 + E_r^4 \\ & + GE_0^2E_r^2 \cdot \left\langle e^{i\left[\phi_a(t) - \phi_a(t+\tau)\right]} \right\rangle \cdot e^{i\Delta\omega\tau} \\ & + GE_0^2E_r^2 \cdot \left\langle e^{-i\left[\phi_a(t) - \phi_a(t+\tau)\right]} \right\rangle \cdot e^{-i\Delta\omega\tau}.\end{aligned} \tag{5.43}$$

The autocorrelation does not depend anymore on the phase noise of the signal itself.

Taking the Fourier transform of (5.43) results in a Loretzian shape spectrum whose linewidth is the spectral broadening due to the amplifier phase noise [71]. In the absence of amplifier, the Fourier transform of (5.43) is a delta function of magnitude $GP_0P_r$, a result expected for a matched paths Mach-Zehnder interferometer (Fig. 5.9).

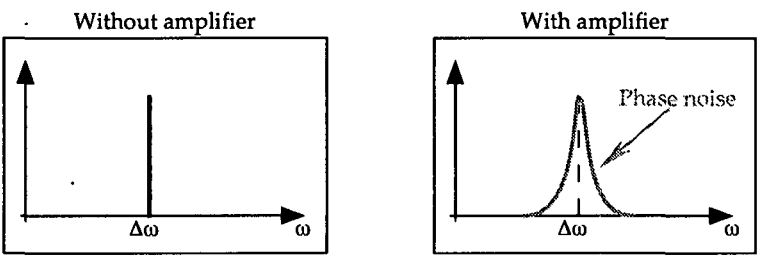


*Fig. 5.9: Autocorrelation spectra in the case of multiplicative phase noise.*

Möller [72], reproduced the experiments of [71]. In his set-up, the resolution of the linewidth measurement was 10 Hz, while the spectral broadening predicted by the modified semiclassical model (Cowle) was 1.3 kHz for a signal linewidth of 1.2 MHz. Even so, no broadening was measured. Unfortunately, the spectral broadening predicted by the semiclassical model was only 15 mHz in this case, thus below the resolution of the instrument, so that it was not possible to check the validity of this model. However, Möller suggested that the description of phase noise by Cowle may be not correct.

In order to clarify the validity of the two models, we started to investigate phase noise with different linewidth of the input signal. We used sources with increasing linewiths, so that the predicted spectral broadening in the case of the semiclassical model became larger than the resolution of our instrumentation.

### 5.3.6 Experimental set-up

We placed the high power fiber amplifier in the interferometer shown in Fig. 5.10. The FFT spectrum analyzer (SR 760) allows a resolution of 250 mHz, so that it should be possible to detect extremely small phase noise. In some cases, an optical filter, 3 nm wide and centered at 1064 nm, was placed in front of the detector to reduce the background of the broad ASE power.

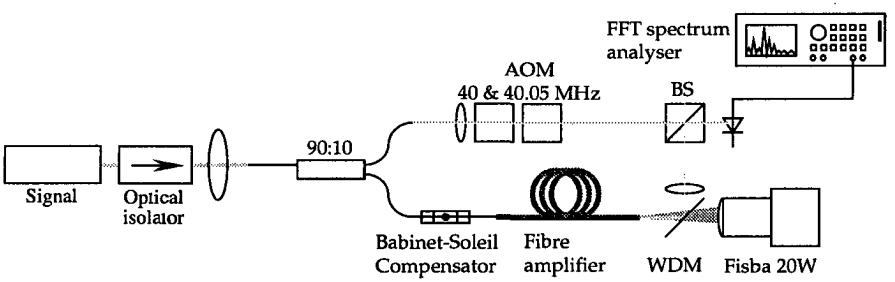


*Fig. 5.10: Set-up for the measurement of phase noise. The measured phase noise is due to the amplifier only.*

### 5.3.7 Effect of the source linewidth

As shown in Fig. 5.7, the theory predicts a phase noise which depends on the power and the linewidth of the input signal. Therefore, we tried to measure the phase noise for sources of different optical linewidths.

*Input signal with 5 kHz linewidth*

With the Nd:YAG single-frequency laser used so far, the predicted spectral broadening cannot be measured. However, the beat spectrum was used for comparison.

*Input signal with 500 kHz linewidth*

We used a DFB fiber laser, which has a linewidth of 500 kHz (a detailed description of this laser is given in § 6.1.). For such a laser, and assuming signals in the mW range, the broadening predicted by the modified model is within 10 Hz and can be detected with our set-up. However, the semiclassical model predicts a broadening in the μHz range, which is much smaller than the resolution of our experimental setup (Fig. 5.11).

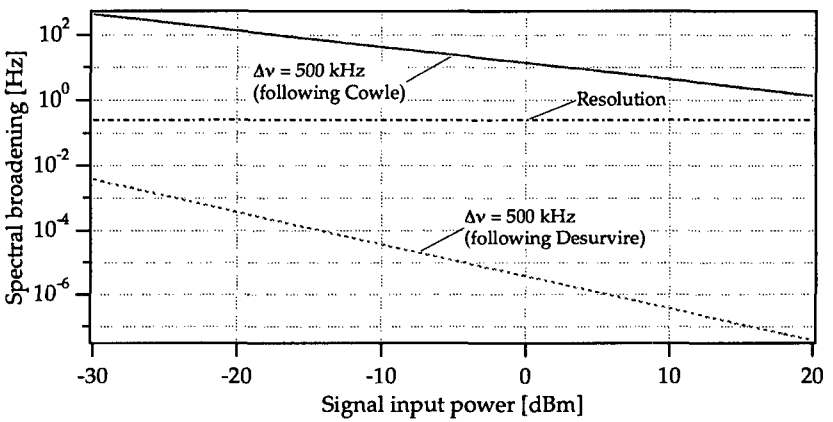


*Fig. 5.11: Expected spectral broadening due to phase noise for 500 kHz linewidth of the input signal, vs. power.*

The power of the laser was varied between 1.7 and 9 dBm. We did a Gaussian fit on the beat spectra measured by a FFT spectrum analyzer with and without amplification. The spectral broadening was calculated as the difference of the widths of the two Gaussian functions. Typical beat spectra are shown in Fig. 5.12 and the resulting values for the spectral broadening are given in Table 5-1.

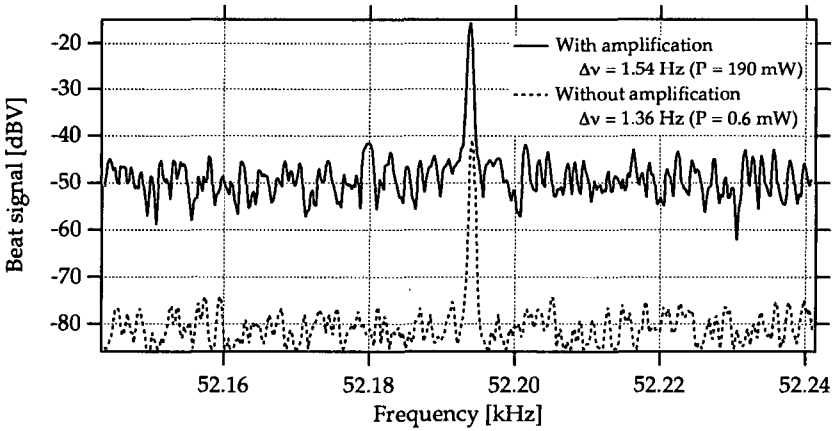


*Fig. 5.12: Comparison of measured beat spectra for a signal linewidth of 500 kHz.*

| Signal input power [dBm] | Resolution [Hz] | Measured spectral broadening [Hz] (Gaussian fit) | Theoretical broadening according to Cowle [Hz] |
|---|---|---|---|
| 1.7 | 0.25 | 0.09 | 11 |
| 2.4 | 0.25 | 0.16 | 10 |
| 5.7 | 0.25 | 0.18 | 7 |
| 9 | 0.5 | 0.14 | 4.8 |

*Table 5-1: Spectral broadening for 500 kHz input linewidth.*

It is obvious from Table 5-1 that the measured spectral broadening is always smaller than the resolution. Moreover, we do not see the spectral broadening predicted by the "Cowle" model, although it is much larger than the resolution of 0.55 Hz. This is the first evidence against the "Cowle" model.

*Input signal with 18 GHz linewidth*

We have built a specially designed double-pass superfluorescent fiber laser (SFL) with a Bragg grating on one side (Fig. 5.13). From the 0.1 nm bandwidth of the grating we expect an emission linewidth of about 25 GHz without any longitudinal modes, since there is no cavity. A booster amplifier allows to get the desired output power.

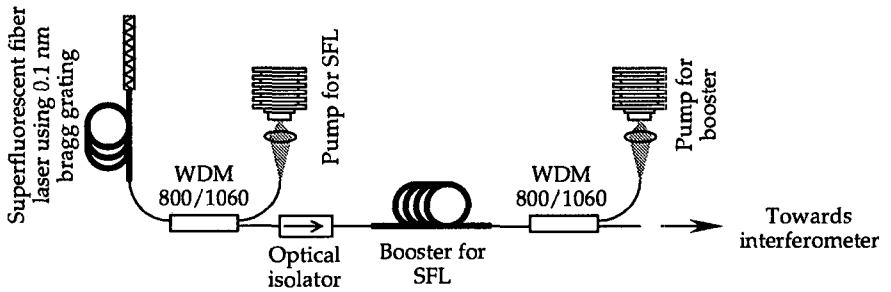


*Fig. 5.13: Double-pass superfluorescent fiber laser with booster.*

By a variation of the reference arm length in the Mach-Zehnder interferometer, one can measured the visibility of the fringe pattern. In the case of a Lorentzian line-shape, a decrease of the visibility by a factor $1/e$ corresponds to the coherence length of the source [73]. The coherence length $l_c$ and the spectral width $\Delta\nu$ of the source are related through

$$l_c = \frac{c}{\pi \ \Delta\upsilon}. \tag{5.44}$$

From the measured fringe visibility (Fig. 5.14), we get a coherence length $l_c = 5.3$ mm, which corresponds to a linewidth of 18 GHz.

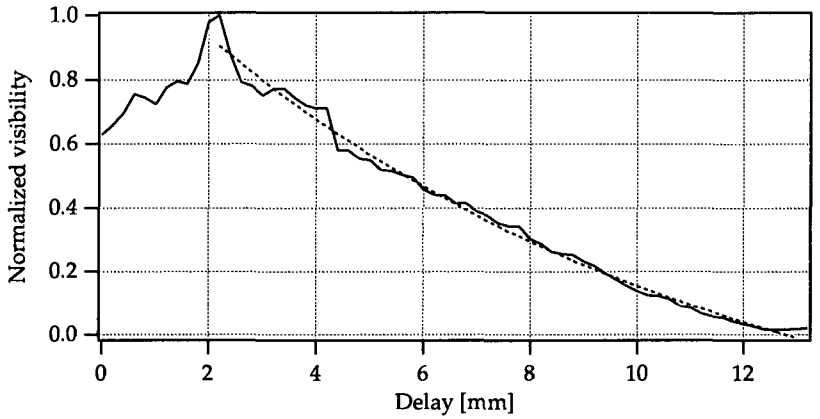


*Fig. 5.14: Measurement of the coherence length of a superfluorescent fiber laser with a 0.1 nm bandwidth Bragg grating. The coherence length is $l_c = 5.3$ mm (visibility = 1/e).*

The beat frequency spectra measured with the balanced Mach-Zehnder interferometer are shown in Fig. 5.15.

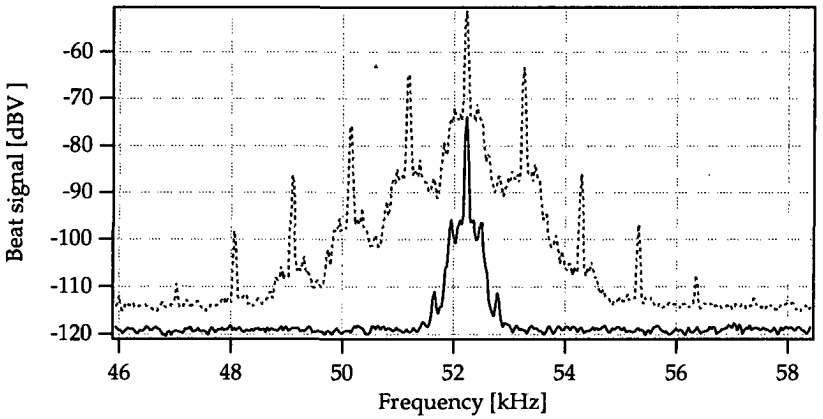


*Fig. 5.15: Phase noise measured for fiber 45SK3 (amplifier) and an 18 GHz linewidth superfluoresent fiber laser as signal. Lower curve: input signal, P = 53 μW; upper curve: amplified signal, P = 5.3 mW.*

In this particular configuration, the expected spectral broadening according to the modified semiclassical description is about 390 MHz. According to the semiclassisal model, the expected broadening is 95 kHz (Fig. 5.7). In fact, nothing is visible!

In another experiment, we simply used the booster as a large bandwidth source; the linewidth is about 2.6 THz (corresponding to a transition linewidth in the order of 10 nm). According to the semiclassical model, the expected spectral broadening in this case is about 2 GHz. The resulting beat spectra look like a copy of the previous measurement: no spectral broadening is observed. This demonstrates clearly that these fiber amplifiers do not introduce the spectral broadening predicted by the models reported in the literature.

### 5.3.8 Effect of the amplifier pump intensity noise

The beat spectra corresponding to signals with either 5 kHz or 18 GHz linewidth look more or less the same (Fig. 5.16).

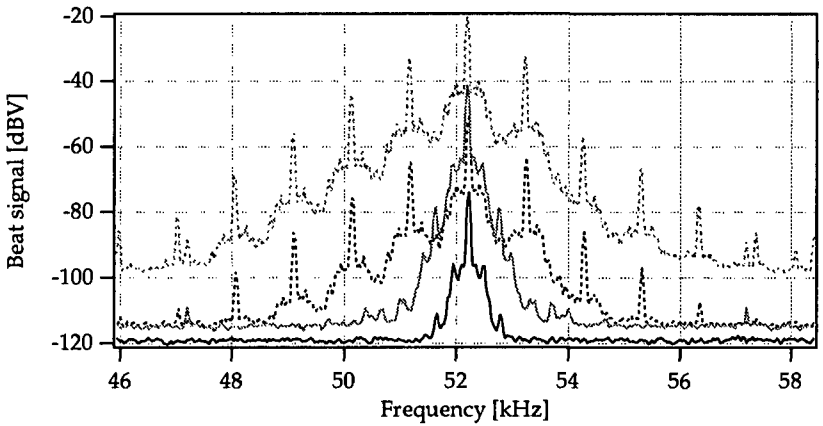


*Fig. 5.16: Comparison of beat spectra for SFL (black curves) and Nd:YAG (gray curves) as signal source. Continuous curves represent the beat spectra before amplification while dashed curves are the amplified beat spectra.*

The vertical shift is due to the different power of these sources. However, both have a noisy structure with peaks regularly spaced at about 1 kHz. This effect is caused by the intensity noise of the amplifier pump diode, shown in Fig. 5.17, which results in an intensity modulation of the amplified signal.

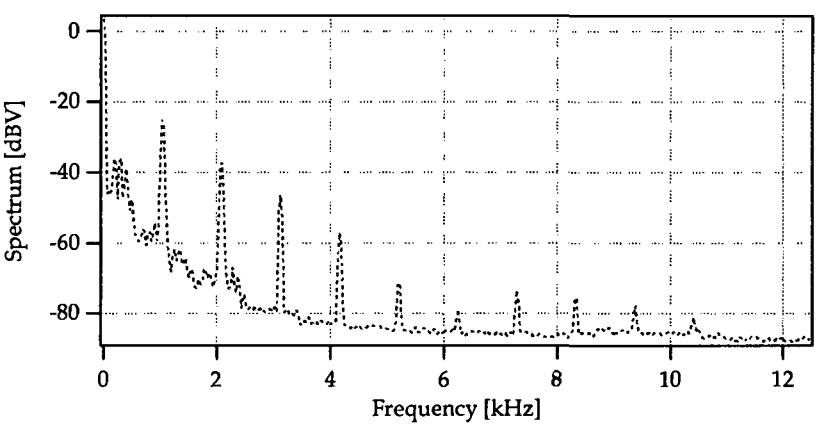


*Fig. 5.17: Intensity noise spectra of the amplifier pump diode.*

In order to eliminate this intensity noise, the double-clad power amplifier was replaced by a portion of single-mode single-clad doped fibers (CSEM 060592B, see description of this fiber in § 1.1) pumped by a 150 mW single-mode laser diode. For the investigations reported in § 5.3.9 and 5.3.10, this amplifier was used instead of the high power systems.

### 5.3.9 Effect of the detector bandwidth on the measured phase noise

The detector bandwidth may be a limiting factor. This can be justified as follows. In the case of a non-balanced interferometer, the expected beat spectrum is twice the width of the source [74]. A detector, whose bandwidth is too narrow, will clip part of the beat signal. The same argument is valid for the balanced interferometer. If the linewidth of the signal is smaller than the bandwidth of the detector, there is no limitation by the detection system. Thus, the bandwidth, which applies in Eqs. (5.34) or (5.39), is the smallest of either the source or the detector. In order to check the validity of this assumption, we replaced the 125 MHz bandwidth detector by a detector having a 1.5 GHz bandwidth.

The incident power on the detector was about 200 nW (taking into account the bandpass filter) and increased to 570 nW when the amplifier was turned on. The predicted broadening for 125 MHz bandwidth is 756 Hz and is 109 kHz in the case of a 1.5 GHz bandwith, as can be computed using Eq. (5.34). No difference was observed between these two measurements, as shown in Fig. 5.18 and Fig. 5.19, except a difference in the beat signal power due to the sensitivity of the detectors. This confirms that no spectral broadening occurs.

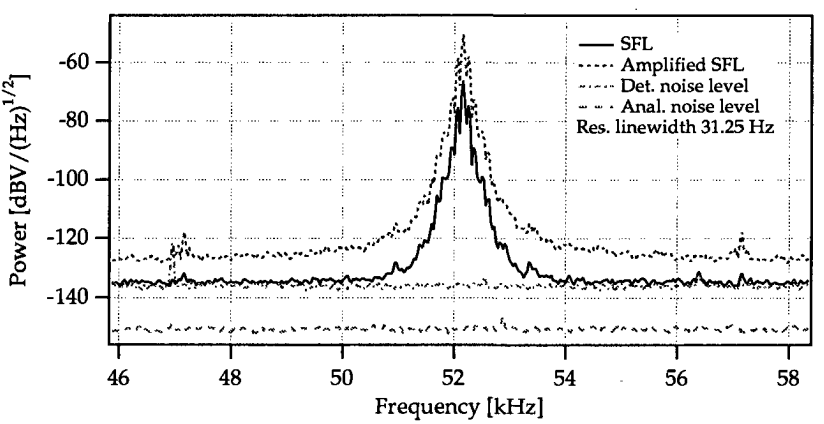


*Fig. 5.18: Measured phase noise for fiber amplifier 060592 and 18 GHz linewidth superfluoresent fiber laser as signal. The detector bandwith is 125 MHz.*

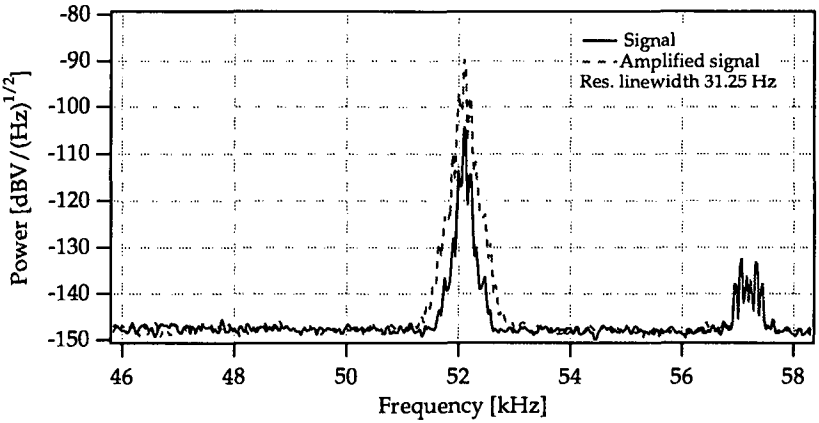


*Fig. 5.19: Measured phase noise for fiber amplifier 060592 and 18 GHz linewidth superfluoresent fiber laser as signal. The detector bandwith is 1.5 GHz.*

### 5.3.10 Phase noise as an additive process

In our experiments, we used broadband superfluorescent fiber lasers such that the spectral broadening predicted by the semiclassical model was larger than the experimental resolution (see § 5.3.7). But no spectral broadening was visible. We also checked the influence of the detector bandwidth (see § 5.3.9). Therefore, we conclude that the currently used descriptions of the introduction of phase noise by optical amplifiers need to be modified, in order to better reflect the reality.

In fact, according to [75], the phase noise is an additive noise rather than a multiplicative noise. Thus, the output of the Mach-Zehnder interferometer becomes

$$E_{out}(t) = \sqrt{G}E_0 \cdot e^{i\phi(t)} \cdot e^{iwt} + E_n \cdot e^{iwt} \cdot e^{i\phi_a(t)} + E_r \cdot e^{i\phi(t+\tau_0)} \cdot e^{i(w+\Delta\omega)(t+\tau_0)}, \tag{5.45}$$

where $E_n$ is the amplitude noise of the amplifier, instead of Eq. (5.41). The autocorrelation of the intensity at the output of the interferometer is

$$\begin{aligned}\Gamma(\tau) = \; & G^2E_0^4 + E_n^4 + E_r^4 + 2GE_0^2E_n^2 + 2GE_0^2E_r^2 + 2E_n^2E_r^2 \\ & + GE_0^2E_n^2 \cdot \left\langle e^{i\left[\phi(t)-\phi(t+\tau)\right]} \right\rangle \cdot \left\langle e^{-i\left[\phi_a(t)-\phi_a(t+\tau)\right]} \right\rangle + c.c. \\ & + GE_0^2E_n^2 \cdot \left\langle e^{i\left[\phi(t)+\phi(t+\tau)\right]} \right\rangle \cdot \left\langle e^{-i\left[\phi_a(t)+\phi_a(t+\tau)\right]} \right\rangle + c.c. \\ & + GE_0^2E_r^2 \cdot \left\langle e^{i\left[\Delta\phi_{\tau_0}(t)-\Delta\phi_{\tau_0}(t+\tau)\right]} \right\rangle \cdot e^{i\Delta\omega\tau} + c.c. \\ & + E_n^2E_r^2 \cdot \left\langle e^{i\left[\phi(t)-\phi(t+\tau+\tau_0)\right]} \right\rangle \cdot \left\langle e^{i\left[\phi_a(t)-\phi_a(t+\tau)\right]} \right\rangle \cdot e^{i\Delta\omega\tau} + c.c.\,,\end{aligned} \tag{5.46}$$

which, in the case of a matched interferometer, reduces to

$$\begin{aligned}\Gamma(\tau) = \; & G^2E_0^4 + E_n^4 + E_r^4 + 2GE_0^2E_n^2 + 2GE_0^2E_r^2 + 2E_n^2E_r^2 \\ & + GE_0^2E_n^2 \cdot \left\langle e^{i[\phi(t)-\phi(t+\tau)]} \right\rangle \cdot \left\langle e^{-i[\phi_a(t)-\phi_a(t+\tau)]} \right\rangle + c.c. \\ & + GE_0^2E_n^2 \cdot \left\langle e^{i[\phi(t)+\phi(t+\tau)]} \right\rangle \cdot \left\langle e^{-i[\phi_a(t)+\phi_a(t+\tau)]} \right\rangle + c.c. \\ & + GE_0^2E_r^2 \cdot e^{i\Delta\omega\tau} + c.c. \\ & + E_n^2E_r^2 \cdot \left\langle e^{i[\phi(t)-\phi(t+\tau)]} \right\rangle \cdot \left\langle e^{i[\phi_a(t)-\phi_a(t+\tau)]} \right\rangle \cdot e^{i\Delta\omega\tau} + c.c.\,,\end{aligned} \tag{5.47}$$

where *c.c.* stands for complex conjugate. This is completely different from (5.43), as shown in Fig. 5.20.

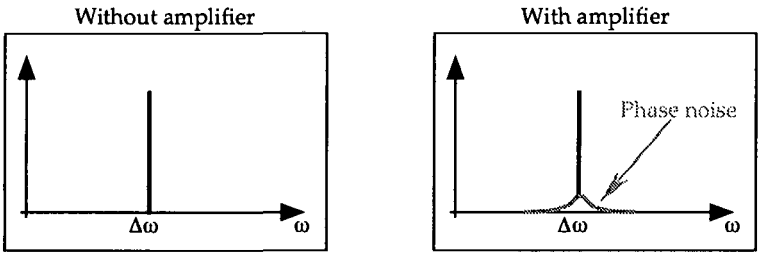


*Fig. 5.20: Autoccorelation spectra in the case of additive phase noise.*

There are now two terms at the beat frequency $\Delta\omega$. The first, whose intensity is $GP_0P_r$ corresponds to a delta function representative of a matched path Mach-Zehnder interferometer. It does not depend on the amplifier. The second, whose intensity $P_nP_r$ is much lower, represents the linewidth of the signal affected by the amplifier phase noise (Fig. 5.20).

We calculated the electrical power of the different terms in Eq. (5.47), in order to confirm the description of the phase noise as an additive noise. The ac electrical power of the measured beat signal is given by ([76])

$$P_{ac}^{el} = 2m^2 \frac{G_{amplifier}^2}{R_{load}} P_{ref} P_{sig}, \tag{5.48}$$

where $G_{amplifier}$ is the conversion gain of the photodetector, taking into account the spectral sensitivity, $R_{load}$ is the output impedance of the electrical amplifier, $P_{ref}$ and $P_{sig}$ are the optical power of the reference beam and the signal beam, respectively, and $m$ is the relative fringe visibility defined as

$$m = \frac{\Gamma_{meas}}{\Gamma_{theo}} \tag{5.49}$$

with

$$\Gamma_{meas} = \frac{I_{max} - I_{min}}{I_{max} + I_{min}}, \; \Gamma_{theo} = \frac{2\sqrt{P_{ref}P_{sig}}}{P_{ref} + P_{sig}}, \tag{5.50}$$

the measured and theoretical fringe visibility.

The characteristics of the detectors are given in Table 5-2.

| Type of detector | 125 MHz bandwidth (New-Focus 1811) | 1.5 GHz bandwidth (Newport AD-300DC) |
|---|---|---|
| $G_{amplifier}$ [V/W] | $26 \cdot 10^3$ | 180 |
| $R_{load}$ | 50 Ω | 50 Ω |

*Table 5-2: Characteristics of the detectors.*

*Measurement with a DFB fiber laser*

We measured the signal power and the noise power in the case of a DFB fiber laser with a linewidth of 500 kHz. The noise power in the bandwidth of the laser was estimated by the measurement of the ASE spectra on both sides of the laser line. The results are given in Table 5-3.

| | Optical power $P$ | $m$ (with reference) |
|---|---|---|
| Reference beam | 7.5 µW | |
| Signal beam (without amplifier) | 100 nW | 1 |
| Signal beam (with amplifier) | 8 µW | 0.8 |
| Noise | 54 fW | 1 (estimated) |

*Table 5-3: Measured power and fringe visibility on the detector for a DFB fiber laser with signal linewidth of 500 kHz. The noise power is measured for a bandwidth of 500 kHz.*

The measured beat spectra are shown in Fig. 5.21.

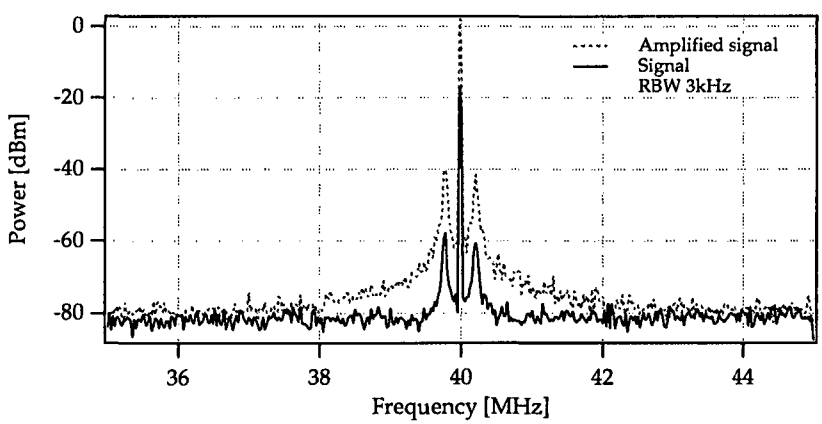


*Fig. 5.21: Beat spectra for a signal linewidth of 500 kHz (the bandwidth of the detection is 125 MHz). Noise levels correspond to the results described in Table 5-4.*

The calculated values, according to Eq. (5.48), are given in Table 5-4 and compared with the measurement of Fig. 5.21. Results are in good agreement. Note that the phase noise level is overestimated; the calculated electrical power is normally distributed over a 500 kHz linewidth whereas the value is given for a delta function. However, the order of magnitude is correct.

| Electrical power | P [dBm] (Calculated) | P [dBm] (Measured) |
|---|---|---|
| Signal level (without amplifier) | -16.9 | -17 |
| Signal level (with amplifier) | 0.2 | 2 |
| Noise level | -79.6 | -80 (det. Noise level) |

*Table 5-4: Calculated and measured electrical level for a DFB fiber laser.*

It is obvious from this first measurement, that the phase noise level is below the laser intensity noise, thus not visible. In fact, phase noise is actually so small that it will always be hidden by some other noise contribution (from the detector or from the signal).

*Measurement with a SFL source*

We did the same measurements in the case of a SFL source. The power and the relative fringe visibility are given in Table 5-5.

| | Optical power $P$ | $m$ (with reference) (det. 125 MHz) | $m$ (with reference) (det. 1.5 GHz) |
|---|---|---|---|
| Reference beam | 4.4 μW | | |
| Signal beam (without amplifier) | 20 nW | 0.48 | 0.48 |
| Signal beam (with amplifier) | 1.86 μW | 0.2 | 0.2 |
| Noise (125 MHz) | 70 pW | 0.5 (estimated) | 0.5 (estimated) |
| Noise (1.5 GHz) | 850 pW | 0.5 (estimated) | 0.5 (estimated) |

*Table 5-5: Measured power and fringe visibility on the detector for a DFB fiber laser with signal linewidth of 500 kHz. The noise power is given for a bandwidth of 500 kHz*

The measured beat spectra obtained with a detection bandwidth of 1.5 GHz are shown in Fig. 5.22.

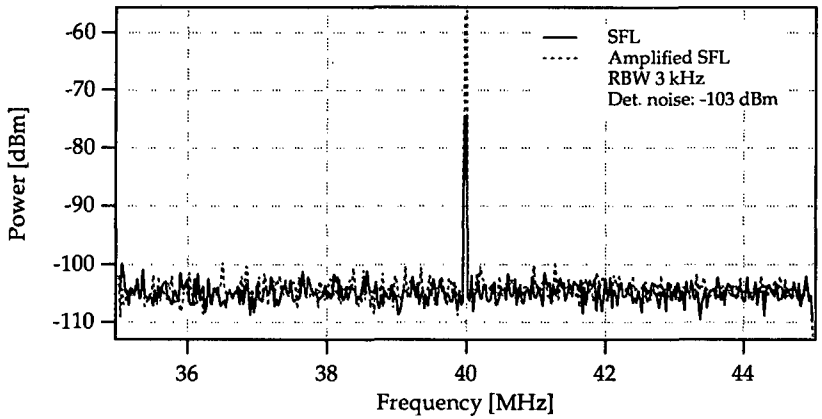


*Fig. 5.22: Beat spectra for a signal linewidth of 18 GHz. The bandwidth of the detector is 1.5 GHz. Noise levels correspond to the results given in Table 5-6.*

The calculated values, according to Eq. (5.48), are given in Table 5-6 and compared with the measurement of Fig. 5.22. The experimental results are again in good agreement with the theoretical prediction, except for the amplified signal level in the case of a 1.5 GHz detection system. The relative fringe visibility may have been overestimated. Note that the electrical level of phase noise must be distributed over the bandwidth, thus reducing its magnitude even much lower. As the level is already below the detector noise floor, we did not calculate the exact value.

| | 125 MHz det. bandwidth | | 1.5 GHz det. bandwidth | |
|---|---|---|---|---|
| | P [dBm] (Calculated) | P [dBm] (Measured) | P [dBm] (Calculated) | P [dBm] (Measured) |
| Signal level (without amplifier) | -32.6 | -35 | -75.8 | -75 |
| Signal level (with amplifier) | -20.5 | -18.3 | -63.7 | -56 |
| Noise level | -103 | -82 (det. noise level) | -146 | -103 (det. noise level) |

*Table 5-6: Calculated and measured electrical level in the case of SFL source, measured either with 1.5 GHz or 125 MHz detector bandwidth.*

From all these experiments, we conclude that the measurement of the effect of the phase noise is not possible because it is smaller than other noise contributions.

### 5.3.11 Phase noise in the case of coherent communication

In the case of coherent communication, 2 lasers are used and the effect of the phase locked loop must be taken into account in the measurement of phase noise. The set-up was modified to include 2 single-frequency Nd:YAG lasers, locked at a difference frequency of 10 MHz. The output of one of the two lasers is amplified while the other serves as local oscillator for the heterodyne detection of the am plified signal (Fig. 5.23).

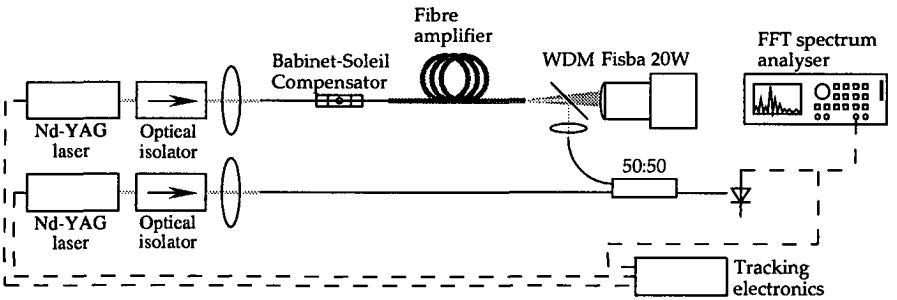


*Fig. 5.23: Set-up for the measurement of the phase noise using two locked lasers as in the communication scheme.*

In this case, Eq. (5.45) becomes

$$E_{out}(t) = \sqrt{G}E_1 \cdot e^{i\phi_1(t)} \cdot e^{iw_1 t} + E_n \cdot e^{iw_1 t} \cdot e^{i\phi_a(t)} + E_2 \cdot e^{i\phi_2(t)} \cdot e^{i\omega_2 t}, \tag{5.51}$$

where $E_1$ and $E_2$ are the amplitude of the two lasers, and $E_n$ is the amplitude noise of the amplifier. The autocorrelation of the intensity at the output of the interferometer is now

$$\begin{aligned}\Gamma(\tau) = \; & G^2E_1^4 + E_n^4 + E_2^4 + 2GE_1^2E_n^2 + 2GE_1^2E_2^2 + 2E_n^2E_2^2 \\ & + GE_1^2E_n^2 \cdot \left\langle e^{i[\phi_1(t)-\phi_1(t+\tau)]} \right\rangle \cdot \left\langle e^{-i[\phi_a(t)-\phi_a(t+\tau)]} \right\rangle + c.c. \\ & + GE_1^2E_n^2 \cdot \left\langle e^{i[\phi_1(t)+\phi_1(t+\tau)]} \right\rangle \cdot \left\langle e^{-i[\phi_a(t)+\phi_a(t+\tau)]} \right\rangle + c.c. \\ & + GE_1^2E_2^2 \cdot \left\langle e^{i[\phi_1(t)-\phi_1(t+\tau)]} \right\rangle \cdot \left\langle e^{-i[\phi_2(t)-\phi_2(t+\tau)]} \right\rangle \cdot e^{-i\Delta\omega\tau} + c.c. \\ & + E_n^2E_2^2 \cdot \left\langle e^{-i[\phi_2(t)-\phi_2(t+\tau)]} \right\rangle \cdot \left\langle e^{i[\phi_a(t)-\phi_a(t+\tau)]} \right\rangle \cdot e^{i\Delta\omega\tau} + c.c. \; .\end{aligned} \tag{5.52}$$

When the two lasers are freely running, the term $GE_1^2E_2^2$ produces a Lorentzian shape in the beat spectrum, whose linewidth is the width of the 2 laser linewidths. When the lasers are frequency locked, we can assume that the phase difference $\phi_1 - \phi_2$ remains constant over the time $\tau$. In this case, the term $GE_1^2E_2^2$ produces a delta function. The effect of phase noise is again in the form of a Lorentzian pedestal lineshape, of power $E_n^2E_2^2$. As for the measurement with one laser, no spectral broadening will appear in the beat spectrum, as can be seen in Fig. 5.24.

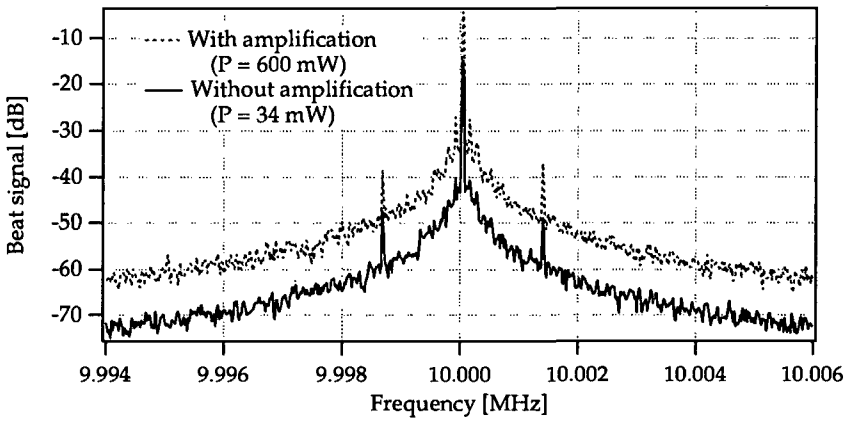


*Fig. 5.24: Phase noise measured for CSEM 100192B fiber amplifier with two frequency locked lasers.*

In coherent communication, the only relevant information is the effect of phase noise at high frequency, as the drifts of the laser frequency can be easily corrected using a low-frequency feedback loop. Thus, for the measurement of the beat spectra, the two lasers are frequency locked with a regulation bandwidth of 10 kHz. The side bands of the beat spectra give information on the electronic bandwidth required to lock the lasers in the communication systems (Fig. 5.24).

The replacement of Nd:YAG single-frequency laser by DFB fiber lasers may be possible but will depend on the results of such an experiment. A project is in preparation to clarify this point.

# 6 All-fiber master oscillator power amplifier

THE systems investigated so far were all based on a single-frequency solid-state laser, as this was the only device commercially available at the beginning of the project. However, during the course of the studies, it became also interesting to investigate other solutions, either to reduce weight or to increase the total output power.

A very interesting approach is to build an all-fiber MOPA. This has been demonstrated at 1.55 μm, with an output power of 160 mW [77], using a single-frequency fiber laser followed by a power amplifier. The wavelength is well controlled and the power can be set to the correct level required by the communication.

The same concept may be important at 1.06 μm for intersatellite coherent communication systems, because it may help to replace some bulky components in the emitter, thus reducing weight of the transmitter head. However, the requirements on linewidth are tough, so that good single-frequency fiber lasers have to be build first.

The highest integration is achieved when an all-fiber phase modulator is combined with the all-fiber MOPA. This is possible using piezo-electric coated devices.

We replace the Nd:YAG laser by a single-frequency fiber laser. In combination with an inline phase modulator, we get an all-fiber MOPA. Section 6.1 describes possible approaches for the fiber laser and presents results we obtained using a DFB fiber laser from Ionas (Denmark) and a new phase modulator design made at the EPFL. It has been submitted for publication in Photonics Technology Letters [78].

After a short review of both single-frequency and phase modulator, we present, to our knowledge, the first all fiber phase-modulated master oscillator power amplifier. It opens the way towards new design of coherent communication systems.

## 6.1 Single-frequency fiber lasers

The simplest structure for fiber lasers is the Fabry-Perot resonator, but it normally does not generate single-frequency operation because of the large gain spectrum and spatial hole burning [13]. This effect can be suppressed using very short cavities, but resulting in poor pump absorption and low efficiency. Moreover, the resulting linewidths are too large compared with the requirements of coherent communication systems.

It has been noted that for two and three-level laser transitions, a piece of unpumped doped fiber in the cavity acts as a saturable absorber, reducing the transmission loss for the lasing mode comparing with the less powerful competing modes. This principle has been applied to $Er^{3+}$ doped fiber laser [79] but without true single-frequency operation. Paschotta [80], using about 1 m long $Yb^{3+}$ doped fiber, demonstrated single-frequency operation with a linewidth in the range of kHz. However, the emission wavelength in $Yb^{3+}$ system depends on the length of the cavity [5] and on the pump wavelength [81] so that it may be difficult to select it in the desired range. For this reason, we investigated other solutions, such as traveling wave loop and Fox-Smith resonators.

### 6.1.1 Traveling wave loop resonator

Traveling wave operation eliminates spatial hole burning and prevents multi-mode operation [82]. Combining this principle with a saturable absorber and narrow band feedback using a Bragg grating, Cheng et al. [83] realized a stable single-frequency tunable fiber laser at 1.55 μm. Based on the same design, we have built a system for 1.06 μm, where the gain media is a $Nd^{3+}$ -doped fiber and the saturable absorber is an $Yb^{3+}$ doped fiber (Fig. 6.1).

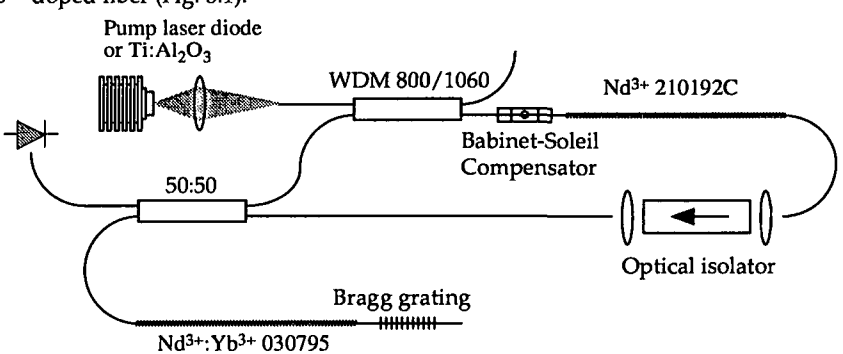


*Fig. 6.1: Traveling wave loop resonator using $Nd^{3+}$ doped fiber as gain medium and $Nd^{3+}$:$Yb^{3+}$ doped fiber as saturable absorber.*

The polarization controller allows adjusting the polarization state to the birefringence in the cavity. We obtained stable single-frequency operation over time in the range of 20 ms, but we were not able to stabilize it. The spectrum was measured using a Fabry-Perot analyzer (Burleigh SA$^{plus}$ Spectrum Analyzer System) with a FSR of 9 GHz and a resolution of 30 MHz. The result is shown in Fig. 6.2

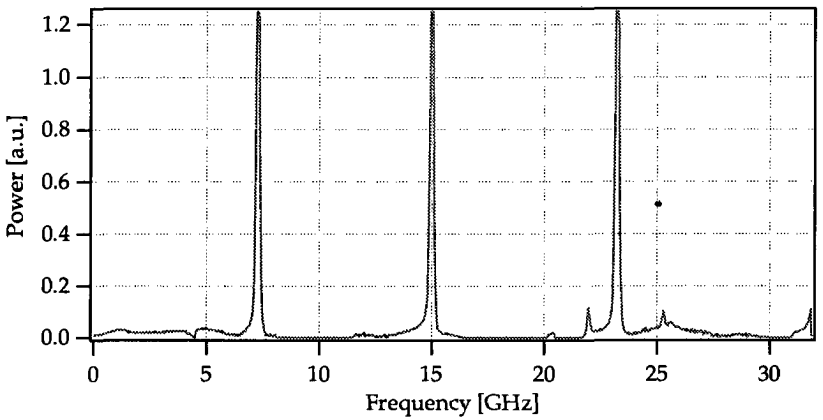


*Fig. 6.2: Emission spectrum of the single-frequency traveling wave resonator. The spacing of the peaks is the FSR of the Fabry-Perot analyzer.*

### 6.1.2 Fox-Smith resonator

A Fox-Smith resonator is made of two coupled cavities with different lengths. Strong mode selection is obtained through the Vernier effect; the only modes which oscillate are those which have the same resonance frequency in both cavities. Thus, Fox-Smith resonators are sensitive to the length ratio of the cavities, allowing long resonator and narrow linewidth. They have been investigated theoretically by Urquhart ([84] [85]) and demonstrated experimentally using erbium doped fiber by Barnsley et al. [86]. Again, we build a system at 1.06 μm to check its feasibility for coherent communication. The set-up is shown in Fig. 6.3.

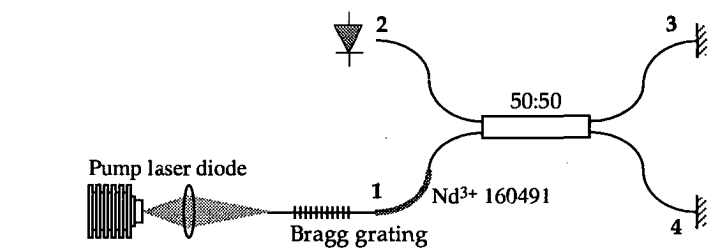


*Fig. 6.3: Fox-Smith resonator using one Bragg grating for narrow emission.*

A resonator build around a coupler can be described using complex electric fields propagating towards and away from the coupler, as reported by Urquhart [84]. Urquhart solved the equations for transversely coupled Fabry-Perot and Fox-Smith resonators, through a lot of cumbersome algebra. These equations, written in the form of matrix, can be solved in a much easier way using numerical computing. Moreover, the method can be applied also to other cavity designs based on couplers.

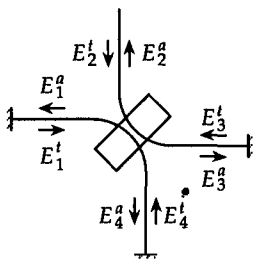


*Fig. 6.4: Nomenclature of the electric fields in a four-port device, as used in Fox-Smith resonator.*

The electric fields are defined in Fig. 6.4. Indices *a* stand for fields travelling away from the coupler while indices *t* stand for fields travelling towards the coupler. We assume that the coupling coefficient is *k* for amplitude. Thus, at the output of the coupler, the transmitted field is simply multiplied by $\sqrt{1-k}$ if it is in the same fiber as the original field and by $j\sqrt{k}$ in the other. The complex number *j* stands for the phase difference between transmission and reflection in the coupler, as required by the conservation of energy.

The transmission losses in the coupler are neglected, as well as its length.

The complex electric fields in the case of a Fox-Smith resonator can be described according to the following sets of equations:

$$\begin{aligned}
E_1^a &= E_4^t\sqrt{1-k} + E_3^t j\sqrt{k} \\
E_2^a &= E_3^t\sqrt{1-k} + E_4^t j\sqrt{k} \\
E_3^a &= E_2^t\sqrt{1-k} + E_1^t j\sqrt{k} \\
E_4^a &= E_1^t\sqrt{1-k} + E_2^t j\sqrt{k} \\
E_1^t &= E_{in}\cdot t_1\cdot\exp\left[(-\alpha+j\beta)L_1\right] + r_1\cdot E_1^a\cdot\exp\left[2(-\alpha+j\beta)L_1\right] \\
E_2^t &= 0 \\
E_3^t &= r_3\cdot E_3^a\cdot\exp\left[2(-\alpha+j\beta)L_3\right] \\
E_4^t &= r_4\cdot E_4^a\cdot\exp\left[2(-\alpha+j\beta)L_4\right]
\end{aligned} \qquad (6.1)$$

where $\alpha$ is the transmission loss in the fiber, $\beta$ is the propagation constant ($=2\pi n_e/\lambda$), $r_i$ and $t_i$ are the field coefficients of reflection and transmission (amplitude) for the mirror *i* and $L_i$ is the length of fiber between the coupler and the mirror.

Written in matrix, Eq. (6.1) becomes

$$\begin{bmatrix} 1 & 0 & 0 & 0 & 0 & 0 & -j\sqrt{k} & -\sqrt{1-k} \\ 0 & 1 & 0 & 0 & 0 & 0 & -\sqrt{1-k} & -j\sqrt{k} \\ 0 & 0 & 1 & 0 & -\sqrt{1-k} & -j\sqrt{k} & 0 & 0 \\ 0 & 0 & 0 & 1 & -j\sqrt{k} & -\sqrt{1-k} & 0 & 0 \\ -r_1\phi(2L_1) & 0 & 0 & 0 & 1 & 0 & 0 & 0 \\ 0 & 0 & 0 & 0 & 0 & 1 & 0 & 0 \\ 0 & 0 & r_3\phi(2L_3) & 0 & 0 & 0 & 1 & 0 \\ 0 & 0 & 0 & -r_4\phi(2L_4) & 0 & 0 & 0 & 1 \end{bmatrix} \begin{bmatrix} E_1^a \\ E_2^a \\ E_3^a \\ E_4^a \\ E_1^t \\ E_2^t \\ E_3^t \\ E_4^t \end{bmatrix} = \begin{bmatrix} 0 \\ 0 \\ 0 \\ 0 \\ t_1\phi(L_1) \\ 0 \\ 0 \\ 0 \end{bmatrix} E_{in} \qquad (6.2)$$

with $\phi(2L_i)=\exp[2(-\alpha+j\beta)L_i]$ and $\phi(L_i)=\exp[(-\alpha+j\beta)L_i]$. It is then straightforward to solve for $E_i^{at}$.

We have solved numerically this equation using the following parameters:

| | |
|---|---|
| Wavelength | 1.06 μm |
| Index of refraction | 1.5 |
| Fiber losses | 0.003 $m^{-1}$ |
| Coupling ratio | 0.5 |

| $i$ | $T_i$ [%] | $R_i$ [%] | $L_i$ [m] |
|---|---|---|---|
| 1 | 5 | 95 | 0.385 |
| 2 | 100 | 0 | - |
| 3 | 6 | 94 | 0.253 |
| 4 | 6 | 94 | 0.1795 |

*Table 6-1: Definition of the parameters used in the simulation of the Fox-Smith resonator.*

The output power in arm 2 is shown in Fig. 6.5.

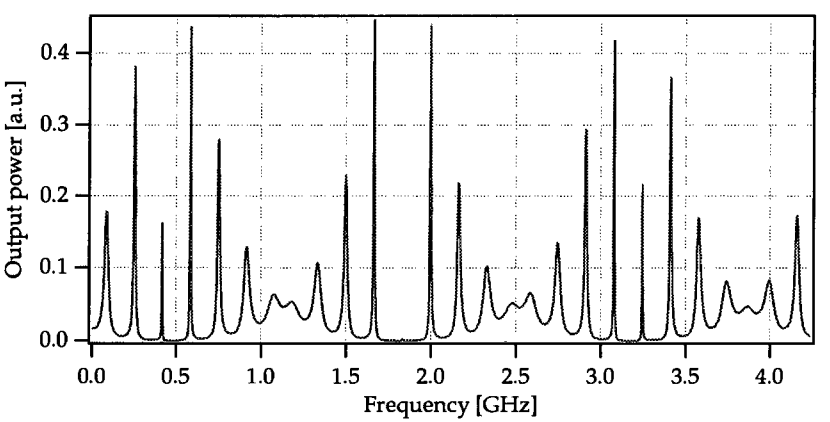


*Fig. 6.5: Simulation of the output power of arm 2 of the passive Fox-Smith resonator.*

The output power in arm 3 is shown in Fig. 6.6.

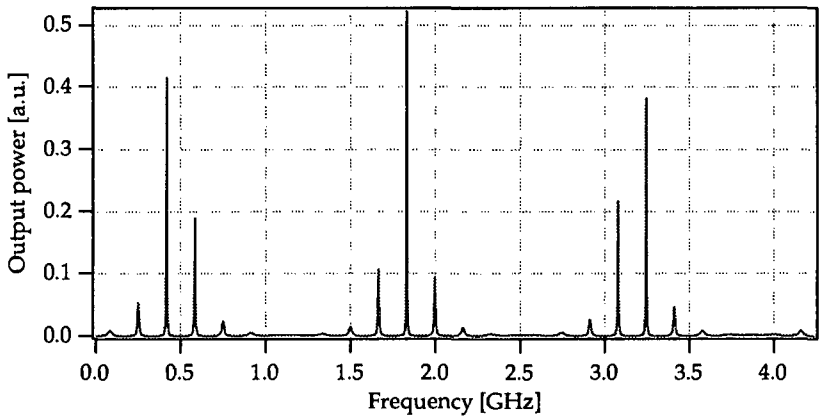


*Fig. 6.6: Simulation of the output power of arm 3 of the passive Fox-Smith resonator.*

The mode spacing is the same in the two arms, as expected for the same cavity. The difference for output on arm 2 or 3 is discussed in [86]. As can be seen in Fig. 6.5 and Fig. 6.6, the passive Fox-Smith resonator has a mode spacing in the range of 1.5 GHz. This is normally sufficient to achieve single-frequency operation when we take into account mode competition phenomena.

With this configuration, we actually obtained single-frequency operation, though not very stable. The output spectrum is shown in Fig. 6.7.

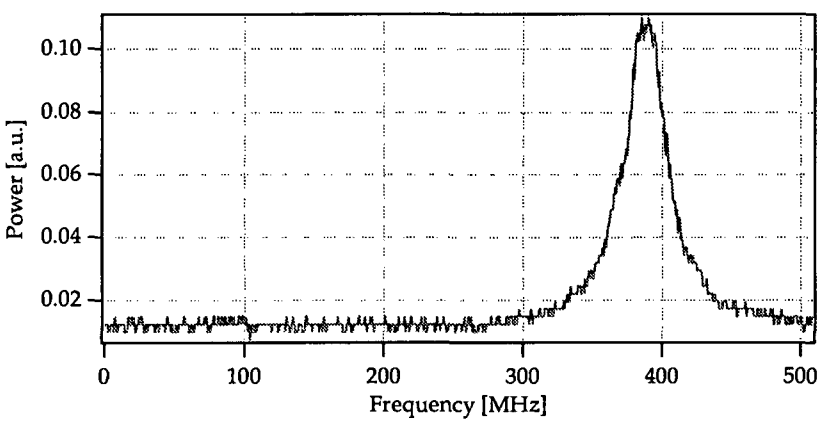


*Fig. 6.7: Emission spectrum of Fox-Smith resonator. The actual linewidth is 35 MHz. The resolution of the Fabry-Perot analyzer is 27 MHz.*

The linewidth of this configuration is in the order of 35 MHz, thus not as narrow has expected. Moreover, the laser jumped from one mode to another. This demonstrates that the mode spacing is not sufficient to get rid of mode hopping, because each dominant mode has the same possible output power. Thus, the smallest perturbation of the system gives the possibility for the emission to jump. We should probably add a piece of unpumped doped fiber in arm 3 or 4 to build a saturable absorber as described in [80].

The method of the complex electric field has also been applied to travelling wave loop and to ring resonators.

### 6.1.3 DFB fiber laser

Distributed feed-back fiber laser became commercially available recently. They are based on long Bragg gratings written in a piece of doped fiber. We bought such a laser from Ionas A/S, Denmark. This laser has the following specification:

| **Specification of Ionas DFB fiber laser** |
|---|
| Linewidth < 500 kHz, Single polarization mode, no mode hopping |
| SNR > 60 dB |
| Temperature stability < 7 pm/K |
| Output power: 10 mW for 100 mW pump power at 980 nm. |

*Table 6-2: Specification of Ionas DFB ytterbium doped fiber laser [87].*

The stability of this fiber laser strongly depends on the pump wavelength. Moreover, as the laser is not packaged, it is sensitive to birefringence, thus sometimes producing cross-polarization operation.

The DFB fiber laser was backward pumped through a WDM 980/1064 nm coupler by a 975 nm pigtailed laser diode made by Uniphase Laser Enterprise. The available pump power was about 300 mW. When pumping the fiber laser, we obtained up to 25 mW of output power. Such a power is compatible with the fiber amplifier to get more than 1 W total output power. Thus, such lasers are serious candidates to replace the heavier and bulkier Nd:YAG laser in space applications. However, further investigation are necessary, mainly to determine whether two such lasers can be frequency locked or not.

Due to the strong industrial interest encountered by the DFB fiber laser approach, a new project is in preparation for investigation of laser fine and fast tuning.

## 6.2 All-fiber phase modulator

The phase modulator is made of piezo-electric material sputtered around an optical fiber. The radial stress induces a variation of the index of refraction, thus a phase modulation.

The all-fiber phase modulator consists of concentric electrodes and piezoelectric coating that form a cylindrical actuator around the fiber [88]. The bottom electrode is made of a 10 nm thick Cr layer and a 100 nm thick Au layer, deposited by thermal evaporation. The 80 mm long ZnO piezoelectric jacket with a thickness of 6 μm is deposited by reactive magnetron sputtering. The top electrode is made of 2 and 6 mm long Cr/Au segments with a thickness of 20/200 nm, deposited by thermal evaporation (Fig. 6.8).

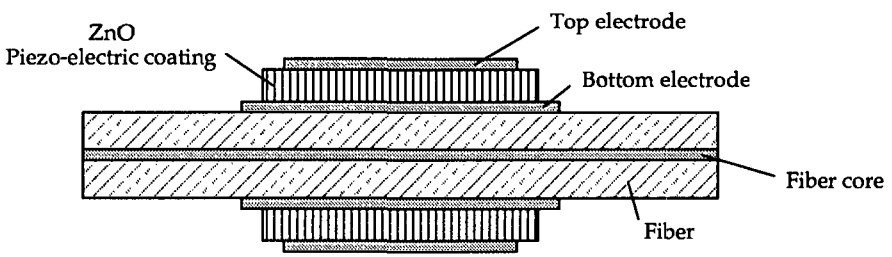


*Fig. 6.8: All fiber phase modulator based on ZnO coating of standard fibers.*

When an electric field is applied to the ZnO coating, a strain results due to the converse piezoelectric effect. Since the piezoelectric and the bottom electrode coatings are bonded to the fiber, the strain induced in the piezoelectric coating is elastically coupled into the fiber. Light waves propagating along the fiber experience then a phase shift.

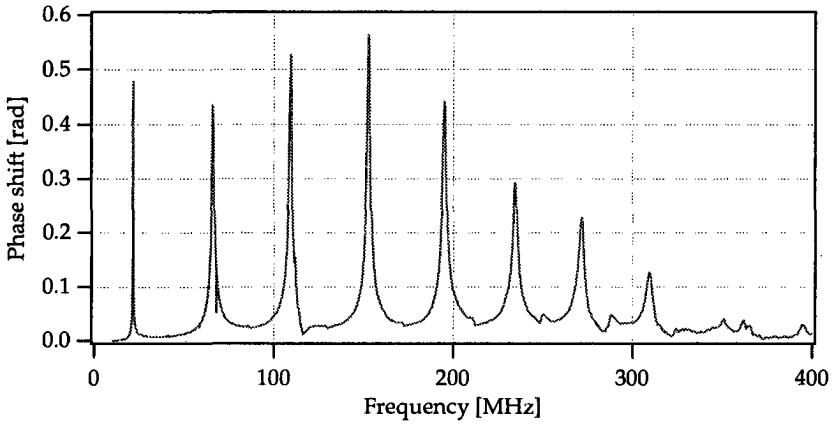


*Fig. 6.9: Phase modulation amplitude between 10 and 400 MHz for an applied source voltage of 4 V.*

Fig. 6.9 shows amplitude of the phase modulation as a function of frequency between 10 and 400 MHz for 4 V amplitude of the electrical signal. The modulator was 6 mm long. The peaks are due to the radial mode resonances of the coated fiber structure. The fundamental peak at 22 MHz is followed by regularly spaced resonance every 44 MHz. For relatively low voltage (< 5V), the amplitude of the phase modulation is a linear function of the excitation. At higher voltages, the response becomes non-linear and the resonance frequencies are shifted to higher values. A maximum modulation depth of about 1.4 rad was measured at 1550 nm [88]. Using the device at 1.06 μm results mainly in a higher modulation depth (up to 2 rad). More recent devices have been tested at higher modulation frequencies and are thus compatible with the requirements of coherent communication [89].

These modulators are made at the Laboratory of Ceramics, EPFL (Swiss Federal Institute of Technology) and characterized at the Institute of Applied Optics, EPFL. These phase modulators are of great interests for coherent communication. As they are based on standard fibers, they do not introduce power limitation as bulk modulators do. As a result, they can be placed before or after the fiber power amplifier.

## 6.3 Realization of an all-fiber MOPA

Using the devices described in the previous sub-section, we built an all-fiber phase modulated MOPA system, combining the DFB fiber laser, the phase modulator and the high-power fiber amplifier (Fig. 6.10).

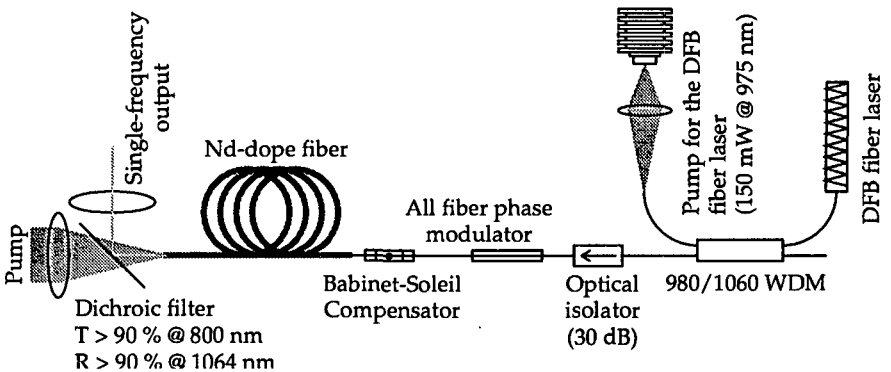


*Fig. 6.10: All-fiber MOPA combining DFB fiber laser, phase modulator and fiber amplifier.*

We measured the gain and the output power of this system. As expected, results are closed to the other investigated amplifiers. However, the DFB laser was not as stable as predicted by the manufacturer so that it was not possible to investigate the gain of the all fiber MOPA at very low signal input power.

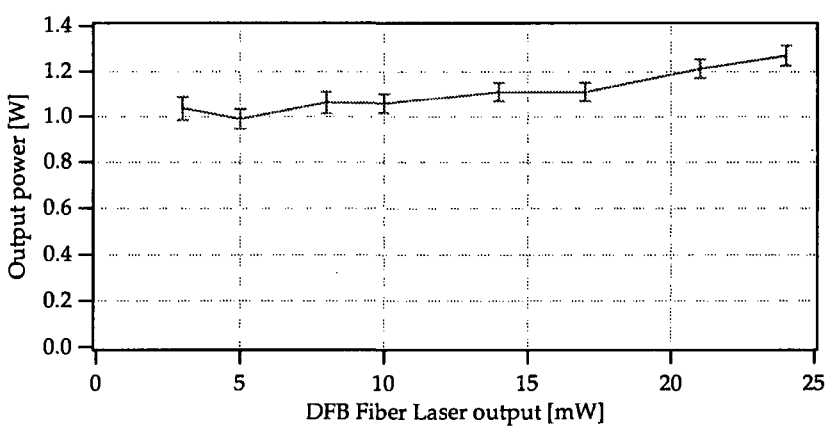


*Fig. 6.11: Fiber amplifier output power versus DFB fiber laser input power. The amplifier is made of a 9 m long 45SK3 fiber coiled in kidney shape and pumped with the Fisba laser module.*

The phase was modulated at 196 MHz, a resonance frequency of the piezoelectric coating. The phase modulation depth was simply measured with a scanning Fabry-Perot spectrum analyzer. The modulation depth $\Delta\varphi$ can be obtained from the ratio

$$\frac{P_1}{P_0} = \left(\frac{J_1(\Delta\varphi)}{J_0(\Delta\varphi)}\right)^2, \tag{6.3}$$

where $P_1$ and $P_0$ are the power in the first harmonic and in the carrier, and $J_1$ and $J_0$ are the first and zero order Bessel functions [90]. A typical spectrum of the phase modulation is shown in Fig. 6.12.

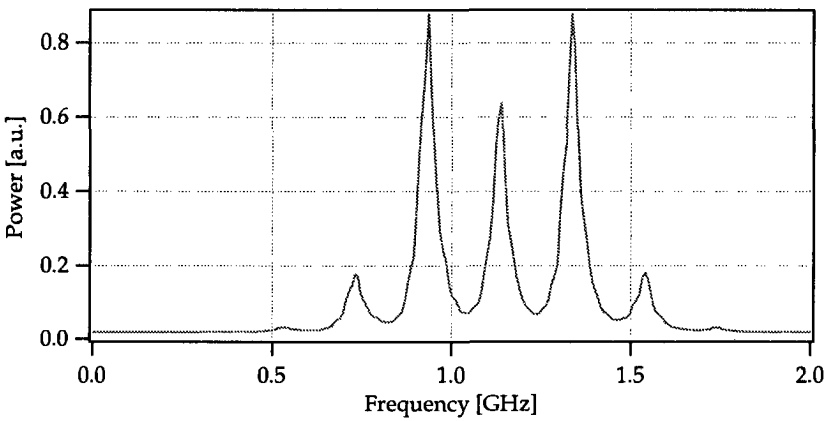


*Fig. 6.12: Fabry-Perot measurement for a depth of modulation of $\Delta\varphi = \pi/2$ at 196 MHz.*

Phase modulation depth up to 1.8 rad have been measured in this condition, at 1.06 µm. We did not observe any difference in the phase-modulated spectra before and after amplification. However, when the DFB fiber laser was operating in dual polarization mode, the output power was equally distributed over the 2 modes.

This work demonstrates that all-fiber structures are now viable solutions in terms of power and data rate. Their main advantages are low insertion loss and a reduction of weight, which are key issues in the context of coherent space communication systems. To the best of our knowledge, this is the first demonstration of an all-fiber phase modulated master oscillator power amplifier. It opens new possibilities for the application of powerful all-fiber structure in coherent communication.

# 7 Conclusion

OPTICAL communication in space is becoming more and more important, as the requirements for bandwidth and also the number of satellites requiring inter-satellite links (ILS) are increasing. For high data rate ISL, coherent optical communication seems to be the best solution, because it provides the highest receiver sensitivity, which helps to minimize the size and the weight of the communication terminal.

The short range optical intersatellite link (SROIL) proposed by the European Space Agency is one possible approach. The design relies on a low power stable single-frequency Nd:YAG laser, which is phase modulated and amplified up to the required output power. Double-clad doped fiber amplifiers have been identified as most promising optical amplifiers for this project.

During this work, we developed and investigated a double-clad $Nd^{3+}$-doped fiber amplifier, designed for the SROIL project.

The polarization stability, which is important to maintain the contrast in coherent communication, is stable within 1° in orientation and the extinction ratio is above 100:1. The variations are slow, in the order of a few tens of seconds. The variations of the polarization are due to thermal expansion of the mechanical support, mechanical vibrations and thermal perturbations of the fiber. The amplifier is completely saturated with an input power of 5 mW and delivers up to 1.3 W output power. It is shorter than other double-clad fiber systems, which is of interest to reduce radiation sensitivity and to increase overall efficiency. The amplified spontaneous emission (ASE) reduces the signal-to-noise ratio of the communication systems, though it is filtered by the coherent detection. When the amplifier is working in complete saturation, the ASE power represents less than 10 % of the total output power for signal input power of 10 to 60 mW. The dopant concentration is optimal around 2% weight. It was, however, not possible to demonstrate whether it is a general rule or not.

The fiber amplifiers developed as part of this project fulfilled the requirements of the SROIL terminal. However, the power may not be sufficient to extend the high-data rate links to medium or long distances GEO-GEO applications, where several Watts are necessary. It has been demonstrated that fiber amplifiers are capable of a few tens of Watts, but they will be limited somewhere by the destruction of the fiber or by non-linear effects. Assuming the fiber amplifier acts as a pre-amplifier for a more powerful device, it is straightforward to consider the combination of fiber and solid-state systems. We used a $Nd^{3+}$ -doped double-clad fiber and a Nd:YAG crystal to demonstrate the principles of dual-stage amplifiers system for coherent communication. The single-mode, single-frequency output power is as high as 3.5 W with a gain of 28 dB. The output power in our experiment was limited by the crystal amplifier, which cannot be driven into saturation. Thus, it was not possible to extract all the available power. However, using a more powerful fiber amplifier as the first stage, we can expect at least 10 W out of the booster crystal. Moreover, Nd:YAG lasers of a few tens of Watts are already available, showing that this second stage may be scaled to even higher power. To the best of our knowledge, this is the first demonstration of two-stage amplifiers combining the advantages of fiber and crystal amplifiers. It opens new possibilities in the field of high-performance coherent space communications.

Power is not the only issue in space communication systems; weight is another one. For this reason, we investigated the possibility to minimize the number of components requiring free-space coupling and to replace them with an integrated solution. We combined a single-frequency DFB fiber laser, a novel all-fiber phase modulator and a double-clad high power fiber amplifier to demonstrate a compact all-fiber phase modulated master oscillator power amplifier. The resulting single-frequency output power was in the range of 1 W. The phase modulator introduced a phase modulation depth of $\pi/2$ at a 200 MHz frequency, with sufficient growth potential to higher bandwidth in the GHz range. This demonstrated that simple all-fiber structures are now viable solutions in terms of power and data rate. Their main advantages are low insertion loss and a reduction of weight. This is again, to the best of our knowledge, the first demonstration of an all-fiber phase modulated master oscillator power amplifier. All-fiber structures seem now to be interesting for space communication. However, the stability of the fiber laser may not be sufficient yet to achieve high data rate in the Gbit/s range. A new project on fine-tuning of DFB fiber laser and linewidth measurement will start soon at IMT in order to investigate in more detail this question.

During all this work, the question of phase noise added by optical amplifiers just puzzled us. In intersatellite coherent communication systems, two lasers separated by a distance of 1000 km or more, must be frequency locked. When phase noise becomes too

important, this results in a reduction of the communication bandwidth. For MOPA structures, the effect of the phase noise introduced by the fiber amplifier must also be taken into account.

The effect of phase noise introduced by fiber amplifiers was first measured in 1990 and was found to broaden the linewidth of the amplified signal. A first model was proposed by Cowle, following the treatment of laser linewidth broadening. The signal at the output of the amplifier was measured with a matched path Mach-Zehnder interferometer. The shape of the beat signal changed from a delta function to a Lorentzian function in presence of the fiber amplifier. A more formal approach, the semiclassical model, was later derived, but seemed in contradiction with the experimental results. A paper published by Möller in 1998 incriminated the original work; the experiment of Cowle was reproduced, but the results were different. No spectral broadening had been seen and, consequently, more detailed experimental and theoretical investigations have been undertaken to solve this problem.

In the semiclassical description of phase noise, the spectral broadening depends on the linewidth and the power of the signal at the amplifier input. Therefore, we measured the linewidth of the signal with and without amplification, for different sources. Our results confirmed that phase noise do not apply in a way similar to line broadening in laser cavities; no spectral broadening was measured. This invalidates the semiclassical approach and confirmed the measurement reported by Möller in 1998.

Going back to the description of noise in amplification, we proposed that phase noise is an additive process, rather than a multiplicative one as described in the earlier original models. As a result, there is no spectral broadening of the signal linewidth due to the fiber amplifier. The beat signal at the output of the matched path Mach-Zehnder interferometer is always a delta function, but a Loretzian pedestal appears in the case of amplification. However, the upper level of this pedestal is normally hidden by the intensity noise of the signal or by the noise of the detection. As a result, the effect of phase noise is not critical in the sense of coherent communication, so that optical amplifiers are indeed a good solution for high-gain high-output power and high-data rate optical links.

The comprehension of phase noise is of scientific importance. The controversy about the effect of phase noise in fiber amplifier has been understood and a valid solution has been shown. Moreover, we proposed a description of phase noise consistent with our experimental results and also with previous results published in literature.

# 8 Acknowledgements

Writing a dissertation is an important personal effort, which can only be successful through a lot of collaboration and discussions with other people. Therefore, at the end of this work, I want to express my thanks to those who help me during the almost five years I spent in Neuchâtel.

First of all, I want to thank Prof. René Dändliker. After my diploma work, while I had already caught the virus for light, he proposed me a position within his group, to deal with doped fibers. Rapidly, he trusted me and delegated to me much of the project management tasks. I appreciated and I learned a lot that way. He also encouraged me writing this thesis and always kept his office open for questions and discussions. Thank you.

I would like also to thank very much Prof W. Lüthy (University of Bern), Dr. R. Czichy (Lockheed Martin) and Prof H.-P. Herzig (University of Neuchâtel) for their interest in my work, as members of the jury

During 4 years, I shared the entire lab and the office with Karim Haroud. Together, we proposed some interesting ideas in the field of doped fibers and could published some of them. Karim was also of a great help while measuring polarization properties of the amplifiers. Thank you Karim.

Doing research alone is not very funny. All over the 5 years, I received help from many colleagues within the group of Prof. Dändliker or the Institute of Microtechnology. Among them, I want to thank Marcel Griocca. He help me a lot with electronics and was ready to listen to my latest crazy idea. He also contributed to the nice atmosphere we had for lunch at the cafeteria (this time, it is your turn to serve the coffee...) I want to thank as well Alphonse Jeandupeux, also for his help with electronics.

Thank you to Dr. Yves Salvadé who taught me to deal with Mach-Zehnder interferometer and spent some time thinking about phase noise.

Thank you to Dr. Thomann from the Observatoire de Neuchâtel, who also took times for fruitful discussion about phase noise and how it should appear in fiber amplifier. This was of great help at the end of the work.

I wish to thank also Philippe Vuilleumier. During his semester work in spring 99, he built and measured the all-fiber MOPA system. His results were of considerable interest for me. He also participated to the early measurement of phase noise and therefore contributed in an important way to this dissertation.

I thank Dr. Peter Blattner as well; he had always available the newest *www* address. But more, he help me a lot when dealing with Matlab for numerical simulation and other computer problems.

Thank you also to Yves-Alain Peter. We build together a Q-switch fiber laser using MEMS and made some publications. But overall, we went sailing, which gave us enough courage to go in the lab in the afternoon.

I wish also to thank Frédéric Gonté for introducing me in the field of adaptive optics for coupling high power laser diode in double-clad fiber amplifiers.

Thank you to Sebastien Dubail, who just reduced the size of some fibers with HF. This was particularly efficient and helpful for my experiments.

I also thank very much those within IMT who contributed to the pleasant atmosphere at lunch time, as well as mechanics, secretary and staff of the institute who were always ready to help and to give advises.

During this dissertation, I had the opportunity to collaborate with many people from other universities. This was a great experience. I particularly want to thank Dr. Peter Tosin at the IAP, University of Bern. I drank a lot of coffee together with Peter when he was making a stop on his way to Cortaillod and he paid them with custom made doped fibers. It was, I believe, a good deal for both of us!

I also want to thank Ueli Roth for his enthusiasm when we were building the dual-stage amplifier and finally succeeded in publishing it. We have had a lot of fun aligning our respective set-up.

I thank Daniele Costantini (Laboratoire d'Optique Appliquée) and Claude Muralt (Laboratoire de Céramique) at the EPF Lausanne. They designed and build an all fiber phase modulator based on piezoelectric coating of single-mode fibers, which I finally used in the all-fiber MOPA experiment. Thank you also to Dr. Hans Limberger and to Daniele again for writing some Bragg gratings for me.

I wish to acknowledge the work of Ram Oron (University of Tel-Aviv). He developed an approach and wrote some codes for the simulation of high power amplifier. He kindly did some computation for me and sent me the code for further study.

I wish also to thank the Swiss Priority Program Optics II for supporting part of this work. I express also my thanks to the SROIL project of the European Space Agency, for some support of this work. Thank you also to my partners at Contraves Space (Zurich) for their help, their advises and also for lending me lasers within the SROIL project.

A long time ago, when I first came to Neuchâtel for my diploma, I worked with Dr. Jacques Morel and Alain Woodtli. They encouraged me and gave me the passion for doped fibers. Thank you Jacques and Alain for you help and your patience at that time.

Je tiens également à remercier mes parents pour leur aide précieuse tout au long de mes études. Ils m'ont donné le goût de la découverte, l'envie d'aller plus loin et surtout la confiance en moi, nécessaire pour mener à terme ce projet.

Merci Christine, merci Rafaël, de m'avoir écouté patiemment parler de mon travail, merci pour la famille que nous formons.

Oberrohrdorf, juillet 2000.

# 9 References

[1] E. Desurvire: "*Erbium-doped fiber amplifiers Principles and Applications,*" John Wiley & Sons, New York, 1994.

[2] A. Bjarklev: "*Optical fiber amplifiers: design and system applications,*" Artech House, Boston, 1993.

[3] P. W. France: "*Optical fibre lasers and amplifiers,*" Blackie, London, 1991.

[4] E. Rochat, A. Woodtli, R. Dändliker: "Excited-state absorption and gain measurement at 1.3 μm in $Nd^{3+}$ doped silica fibers with different codopants: effect of ceasium on ESA cross-section," *J. Ligthwave Technol.*, vol. 15, pp 1573-1577, 1997.

[5] H. M. Pask, R. J. Carman, D. C. Hanna, A. C. Tropper, C. J. Mackechnie, P. R. Barber, J. M. Dawes: "Ytterbium-doped silica fiber lasers: versatile sources for the 1-1.2μm region," *J. Sel. Topics Quantum Electron.*, vol. 1, pp. 2-13, 1995.

[6] W. L. Barnes, S. B. Poole, J. E. Townsend, L. Reekie, D. J. Taylor, D. N. Payne: "$Er^{3+}$-$Yb^{3+}$ and $Er^{3+}$ doped fiber lasers," *J. of Lightwave Tech.*, vol. 7, pp. 1461-1465, 1989.

[7] M. Pollnau, Ch. Ghisler, W. Lüthy, H. P. Weber, J. Schneider, U. B. Unrau: "Three-transition cascade erbium laser at 1.7, 2.7 and 1.6 μm," *Opt. Lett.*, vol. 22, pp. 612-614, 1997.

[8] J. F. Digonnet, C. J. Gaeta: "Theoretical analysis of optical fiber laser amplifiers and oscillators," *Appl. Opt.*, vol. 24, pp. 333-342, 1985.

[9] M. J. F. Digonnet, : "Theory of superfluorescent fiber lasers," *J. Ligthwave Technol.*, vol. LT4, pp. 1631-1639, 1986.

[10] M. Peroni, M. Tamburrini: "Gain in erbium-dopef fiber amplifiers: a simple analytical solution for the rate equations," *Opt. Lett.*, vol. 15, pp. 842-844, 1990.

[11] *EDFA Design* by Optiwave Corporation. More information can be found in "What is EDFA Design", *www.optiwave.com/edfa.htm*, ©1997

[12] B. E. A. Saleh, M. C. Teich: "*Fundamentals of Photonics*," John Wiley & Sons, New York, 1991.

[13] A. E. Siegman: "*Lasers*," University Science Books, Mill Valley, California, 1986.

[14] A.Yariv: *Optical electronics*, Holt, Reinhart and Winston, New York, 1985.

[15] E. Desurvire, J. L. Zyskind, C. R. Gilles: "Design optimization for efficient erbium-doped fiber amplifiers," *J. Ligthwave Technol.*, vol. 8, pp 1730-1741, 1990.

[16] J. Morel: "Study of the coherent coupling of fiber lasers by use of an intracavity phase grating," Ph.D. dissertation, University of Neuchâtel, 1994

[17] A. W. Snyder J. D. Love: *Optical waveguide theory*, Chapman and Hall, London, 1983.

[18] S. Bedö, W. Lüthy, H. P. Weber: "The effective absorption coefficient in double-clad fibres," *Optics Com.*, vol. 99, pp. 331-335, 1993.

[19] A. Hardy, R. Oron: "Signal amplification in strongly pumped fiber amplifiers," *J. Quantum Electron.*, vol. 33, pp. 307-313, 1997.

[20] A. Hardy, R. Oron: "Amplified spontaneous emission and Rayleigh backscattering in strongly pumped fiber amplifiers," *J. Ligthwave Technol.*, vol. 16, pp 1865-1873, 1998.

[21] D. W. Hewak, B. Samson, J. A. Medeiros Neto, R. I. Lamming, D. N. Payne: "Emission at 1.3 μm from dysprosium-doped Ga:La:S glass," *Electron. Lett.*, vol. 30, pp. 968-970, 1994.

[22] T. Schweizer, B. N. Samson, R. C. Moore, D. W. Hewak, D. N. Payne: "Rare-earth doped chalcogenide glass fibre laser," *Electron. Lett.*, vol. 33, pp. 414-416, 1997.

[23] H. Takebe, K. Yoshino, T. Murata, K. Morinaga, J. Hector, W. S. Brocklesby, D. W. Hewak, J. Wand, D. Payne: "Spectroscopic properties of $Nd^{3+}$ and $Pr^{3+}$ in gallate glasses with low phonon energies," *Appl. Opt.*, vol. 36, pp. 5839-5843, 1997.

[24] P. R. Morkel, M. C. Farries, S. B. Poole, "Spectral variation of excited state absorption in neodymium doped fiber lasers," *Optics comm.*, vol. 67, pp. 349-352, 1988.

[25] M. J. F. Digonnet, "Closed-form expressions for the gain in three- and four-level laser fibers," *J. Quantum Electron.* vol. 26, pp. 1788-1796, 1990.

[26] R. Wyatt, "Spectroscopy of rare earth doped fibers," Fiber laser sources and amplifiers (SPIE vol. 1171), pp. 54-64, 1989.

[27] M. Brierley, S. Carter, P. France and J. E. Petersen, "Amplification in the 1300 nm telecommunications window in a Nd-codoped fiber," *Electron. Lett.*, vol. 26, pp. 329-330, 1990.

[28] W. F. Krupke, "Induced-emission cross-section in neodymium laser glasses," *J. Quantum Electron.*, vol. 10 , pp. 450-457, 1974.

[29] W. L. Barnes, P. R. Morkel, J. E, Townsend, "Detailed characterization of $Nd^{3+}$ doped SiO2-GeO2 glass fiber lasers," *Optics comm.*, vol. 82, pp. 282-288, 1991.

[30] P. Tosin, W. Lüthy, H. P. Weber: "Determination of the spectral absorption in silica samples with known rare-earth dopant concentration," paper SX: P74, CIMTEC'98, 14-19 June 98, Firenze (CIMTEC: World Ceramics Congress & Forum on New Materials, 9th International Conference on Modern Materials & Technologies).

[31] P. Tosin, W. Lüthy, H. P. Weber: "Determination of concentration of rare-earth dopants in optical fibers," paper SX-2: L10, CIMTEC'98, 14-19 June 98, Firenze.

[32] J. Morel, A. Woodtli, R. Dändliker, "Characterization of the fluorescent lifetime of doped fibers by using the frequency transfer function," *J. Ligthwave Technol.*, vol. 14, pp. 739-742, 1996.

[33] K. Arai, H. Namikawa, K. Kumata, T. Honda, "Aluminum or phosphorus co-doping effects on the fluorescence and structural properties of neodymium -doped silica glass," *J. Appl. Phys.*, vol. 59, pp. 3430-3436, 1985.

[34] J. Evans : "Les réseaux de satellites" in Pour la Science, No 248, 1998, pp. 48-56.

[35] H.P. Lutz: "Optical Communications in Space - Twenty Years of ESA Effort," ESA Bulletin 91, pp. 25-31, 1997.

[36] R. H. Czichy: "Miniature optical terminals," *Space Com.* vol. 15, pp. 105-112, 1998.

[37] L. Kazovsky, S. Beneretto, A. Willner: *"Optical Fiber Communication Systems,"* Artech House, London, 1996.

[38] R. Dändliker: *"Optique appliquée I & II,"* Note de cours pour l'EPFL, Université de Neuchâtel, 1996.

[39] A. Küng: *"Les transmissions cohérentes,"*Séminaire d'optique avancée, IMT-IOA, 1999.

[40] B. Wandernoth: "5 photon/bit low complexity 2 Mbit/s PSK transmission breadboard experiment with homodyne receiver applying synchronization bits and convolutional coding," ECOC'94, 20th European Conference on Optical Communication, September 26-30, Firenze, Italy, 1994.

[41] T. Tolker-Nielsen, J-C. Guillen: "SILEX: The First European Optical Communication Terminal in Orbit," ESA Bulletin 96, 1998

[42] *Terminal for short range optical intersatellite links: Executive summary,* Oerlikon-Contraves Space, Zürich, 1997.

[43] E. Snitzer, H. Po, F. Jakimi, R. Tumminelli, B. C. McCollum: "Double-clad, offset core Nd fiber laser," *OFC*, PD5, 1988.

[44] H. Po, J. D. Cao, B. M. Laliberte, R. A. Minns, R. F. Robinson, B. H Rockney, R. R. Tricca and Y. H. Zhang: "High power neodymium-doped single transverse mode fibre laser," *Electron. Lett.* vol. 29, pp. 1500-1501, 1993.

[45] H. Zellmer, U. Willamowski, A. Tünnermann, H. Welling, S. Unger, V. Reichel, H.-R. Müller, J. Kirchhof, P. Albers: "High-power cw neodymium-doped fiber laser operating at 9.2 W.with high beam quality." *Opt. Lett.* vol. 20, pp. 578-580, 1995.

[46] E. Rochat, K. Haroud, R. Dändliker: "High power Nd-doped fiber amplifier for coherent intersatellite links," *J. Quantum Electron.*, vol. 35, pp. 1419-1423, 1999.

[47] E. Rochat, K. Haroud, U. Roth, J. E. Balmer, R. Dändliker, H. P. Weber: "High-gain solid-state and fiber amplifier-chain for high-power coherent communication,"*Photon. Technol. Lett.*, vol. 11, pp. 1120-1122, 1999.

[48] H. Zellmer, A. Tünnermann, H. Welling: "Faserlaser - kompakte Strahlquellen im nahinfraroten Spektralbereich," *Laser und Optoelektronik*, vol. 29, pp. 53-59, 1997.

[49] P. Glas, M. Naumann, A. Schirrmacher, Th. Pertsch: "The multicore fiber – a novel design for a diode pumped fiber laser," *Optics Com.*, vol. 151, pp. 187-195, 1998.

[50] H. Henschel, O. Köhn, H. U. Schmidt, J. Kirchhof, S. Unger: "Radiation-induced loss of rare earth doped silica fibers," RADECS'97, European Conference Radiation and their Effects on Devices and Systems, Cannes, September 15-19, 1997

[51] G. M. Williams, M. A. Puman, E. J. Friebele: "Space radiation effects on erbium doped fibers," Photonics for Space Environments IV (SPIE vol. 2811), pp. 30-37, 1996.

[52] W. C. Goltsos:" Radiation-induced loss studies in Er-doped fiber amplifier systems," Free-Space laser Communication Technologies VIII (SPIE vol. 2699), pp. 304-309, 1996.

[53] Th. Weber, W. Lüthy, H. P. Weber: "Side-pumped fibre laser," *Appl. Phys. B*, vol. 63, pp. 131-134, 1996.

[54] J. P. Koplow, L. Goldberg, D. A. V. Kliner: "Compact 1-W Yb-doped double-cladding fibre amplifier using V-groove side-pumping," *Photon. Technol. Lett.* vol. 10, pp. 793-795, 1998

[55] T. Miyazaki, K. Inagaki, Y. Karasawa, M. Yoshida: "Nd-doped double-clad fiber amplifier at 1.06 μm," *J. Ligthwave Technol*, vol. 16, pp. 562-566, 1998.

[56] P. R. Morkel, R. I. Lamming: "Theoretical modeling of erbium-doped fiber amplifiers with excited-state absorption," *Opt. Lett.*, vol. 14, pp. 1062-1064, 1989.

[57] T. Araki, S. Yamakawa, M. Furuya, Y. Hisada: "Latest results and trade-off of high power optical fiber amplifiers for optical inter-orbit communications," Free Space Laser Communication Technologies X (SPIE vol. 3266), pp. 42-48, 1998.

[58] R. Ulrich: "Polarization stabilisation on single-mode fiber," *Appl. Phy. Lett.*, vol. 35, pp. 840-842, 1979.

[59] R. M. A. Azzam: "Division-of-amplitude photopolarimeter (DOAP) for the simultaneous measurement of all four Stokes parameters of light," *Optica Acta*, vol. 29, pp. 685-689, 1982.

[60] I. P. Kaminov: "Polarization in optical fibers," *J. Quantum Electron.*, vol. 17, pp. 15-21, 1981.

[61] A. Lui, K. Ueda: "Propagation losses of pump light in rectangular double-clad fibres," *Opt. Engineering*, vol. 35, pp. 3130-3134, 1996.

[62] M. Kehrli: "Properties and laser performance of an $Yb^{3+}$-silica fibre," Diplomarbeit, IAP, University of Bern, Switzerland, 1999.

[63] I. Zawischa, K. Plamann, C. Fallnich, H. Welling, H. Zellmer, A. Tünnermann: "All-solid-state neodymium-based single-frequency master-oscillator fiber power-amplifier system emitting 5.5 W of radiation at 1064 nm," *Opt. Lett.*, vol. 24, pp. 469–471, 1999.

[64] S. MacCormack, E. Vail, M. Ziari, S. O'Brian, R. Zanoni, S. Sanders, R. Waarts: "High speed, high power double-clad fiber amplifiers," CLEO'98, paper CWE 5, San Francisco, 1998.

[65] V. Dominic, S. MacCornack, R. Waarts, S. Sanders, S. Bicknese, R. Dohle, E. Wolak, P. S. Yeh, E. Zucker: "110W fibre laser," *Electron. Lett.*, vol. 35, pp. 1158-1159, 1999.

[66] H.P. Weber, W. Hodel: "High power light transmission losses in optical waveguides," High Power Laser and Their Industrial Applications (SPIE vol. 650), pp. 102-108, 1986.

[67] Th. Graf, U. Roth, M. Schmid, J. E. Balmer, H. P. Weber : "Diode-pumped Nd:YAG amplifier for intersatellite optical communication," *Optics Comm.*, vol. 152, pp. 302–306, 1998.

[68] U. Roth, Thomas Graf, E. Rochat, K. Haroud, Jürg E. Balmer, and Heinz P. Weber: "Saturation, Gain, and Noise Properties of a Multipass Diode-Laser-Pumped Nd:YAG CW Amplifier," *J. Quantum Electron.*, vol. 34, pp. 1987-1991, 1998.

[69] H. Heffner: "The fundamental noise limit of linear amplifiers," *Proc. IRE*, vol. 50, pp. 1604 – 1608, 1962; also in *Quantum Theory and Measurement*, J. A. Wheeler and W. H. Zurek, Eds. Princeton, Princeton Univ., 1983, pp. 725 – 735.

[70] G. J. Cowle, P. R. Morkel, R. I. Laming, D. N. Payne: "Spectral broadening due to fibre amplifier phase noise," *Electron Lett.*, vol. 26, pp. 424-425, 1990.

[71] G. J. Cowle, "Narrow-linewidth erbium-doped fiber lasers," Ph.D. dissertation, University of Southampton, 1991.

[72] L. Möller: "Novel aspects of spectral broadening due to fiber amplifier phase noise," *J. Quantum Electron.*, vol. 34, pp. 1554-1558, 1998.

[73] Y. Salvadé: "Distance measurement by multiple-wavelength interferometry," Ph.D. dissertation, University of Neuchâtel, 1999.

[74] H. Ludvigsen, E. Bødtker: " New method for self-homodyne laser linewidth measurements with a short delay fiber," *Optics Comm.*, vol. 110, pp. 595 – 598, 1994.

[75] H. A. Haus, J. A. Mullen: "Quantum noise in linear amplifiers," *Phys. Rev.* vol. 128, pp. 2407-2413, 1962.

[76] E. Zimerman: "Signal processing for optical phase detection" Ph.D. dissertation, University of Neuchâtel, 1997.

[77] J. J. Pan, Y. Shi: "166-mW single-frequency output power interactive fiber lasers with low noise," *Photon. Technol. Lett.*, vol. 11, no1, pp. 36–38, 1999.

[78] E. Rochat, D. M Costantini, C. A. P. Muller, K. Haroud, H. G Limberger, R. Dändliker, R. P. Salathé: " All-fiber Phase Modulated Master Oscillator Power Amplifier," accepted for publication, *Photon. Technol. Lett.*, September issue, 2000.

[79] M. Horowitz, R. Daisy, B. Fischer, J. Zyskind: "Narrow-linewidth, singlemode erbium-doped fibre laser with intracavity wave mixing in saturable absorber," *Electron. Lett.*, vol. 30, pp. 648-649, 1994.

[80] R. Paschotta, J. Nilson, L. Reekie, A. C. Trooper, D. C. Hanna: "Single-frequency ytterbium-doped fiber laser stabilized by spatial hole burning," *Opt. Lett.*, vol. 22, pp. 40-42, 1997.

[81] R. Paschotta, J. Nilsson, A. C. Tropper, D. C. Hanna: "Ytterbium-doped fiber amplifiers," *J. Quantum Electron.*, vol. 33 pp. 1049-1056, 1997.

[82] G. J. Cowle, D. N. Payne: "Single-Frequency travelling-wave erbium-doped fibre loop laser," *Electron. Lett.*, vol. 27, pp. 229-230, 1991.

[83] Y. Cheng, J. T. Kringlebotn, W. H. Loh, R. I. Laming, D. N. Payne: "Stable single-frequency traveling-wave fiber loop laser with integral saturable-absorber-based tracking narrow-band filter," *Opt. Lett.*, vol. 20, pp. 875-877, Avril 1995.

[84] Paul Urquhart: "Transversely coupled fiber Fabry-Perot resonator: theory," *Appl. Opt.*, vol. 26, pp. 456-463, 1987.

[85] Paul Urquhart: "Compound optical-fiber-based resonators," *J. Opt. Soc. of Am. A.*, vol. 5, pp. 803-812, 1988.

[86] P. Barnsley, P. Urquhart, C. Millar, M. Brierley: "Fibre Fox-Smith resonators: application to single-longitudinal-mode operation of fibre lasers," *J. Opt. Soc. of Am. A.*, vol. 5, pp. 1339-1346, 1988.

[87] Ionas Integrated Optical Network Coponents A/S: "Single channel DFB fiber laser 1064 nm," Product information sheet, Denmark, august 1998.

[88] N.H. Ky, H.G. Limberger, G.R. Fox, R.P. Salathé, "400 MHz-bandwidth all-fiber phase modulators with ZnO coating on standard telecommunication fiber", *Photon. Technol. Lett.*, vol. 8, pp. 629-631, 1996.

[89] D.M. Costantini, H.G. Limberger, R.P. Salathé, C.A.P. Muller, P. Muralt, N. Setter, S.A. Vasiliev, O.I. Medvedkov, E.M. Dianov, "Acousto-Optic Amplitude Modulator based on a Long-Period Fiber Grating Mach-Zehnder Interferometer", OSA Topical Meeting on Bragg Gratings, Photosensitivity, and Poling in Glass Waveguides, Stuart, Florida USA, September 23-25, 1999.

[90] Reference data for radio engineers, 6th edition, Howard W. Sams & Co ITT, Indianapolis, 1975.

ISBN 3-930803-89-5